Numerical Study of Jet Noise Generated by Turbofan Engine Nozzles

Equipped with Internal Forced Lobed Mixers

using the Lattice Boltzmann Method

Hao Gong

Department of Mechanical Engineering

McGill University, Montreal

April, 2013

A thesis submitted to McGill University in partial fulfillment of the

requirements of the degree of Master of Engineering

ACKNOWLEDGEMENTS

---

[1] PowerFLOW is a registered trademark of Exa Corporation.

TABLE OF CONTENTS

LIST OF TABLES

LIST OF FIGURES

NOMENCLATURE

Roman Symbols

A	Area
c_i	Particle speed
C_p	Specific heat capacity at constant pressure
D	Diameter
D_{mp}	Diameter of the mixing plane
f_i	Distribution function
F_i	Equilibrium distribution function
H_{mp}	Height of mixing plane
H_m	Height of mixer lobe
L	Nozzle nominal mixing length
L_{char}	Characteristic length
L_s	Scalloping depth
m	Mass
M	Mach number
NPR	Total pressure ratio
NTR	Total temperature ratio
p	Pressure
p_{char}	Characteristic pressure
R	Ideal gas constant
S	Symmetric parts of the velocity gradient tensor
r	Radial distance
T	Lattice temperature
T_{char}	Characteristic temperature
t	Time
t_{ts}	Simulation time

t_s	Simulated physical time in one time step
U	Streamwise velocity
V_{char}	Characteristic velocity
v	Mean velocity of flow
w_i	Weight parameter for lattice model
x,y,z	Cartesian coordinates

Greek Symbols

Δt	Time resolution
Δr	Simulation resolution
k	Turbulent kinetic energy
ρ	Fluid density
ρ_{char}	Characteristic density
$\rho u(x,t)$	First order moment of fluid velocity
λ	Wavelength
τ	Relaxation time
ν	Kinematic viscosity
ν_{char}	Characteristic viscosity
ε	Energy dissipation rate
Ω	Anti-symmetric parts of the velocity gradient tensor
∇u	Velocity gradient tensor

Superscripts, Subscripts, and Accents

$(\cdot)_i$	Direction of particles in a lattice model
$(\cdot)_j$	Jet properties
$(\cdot)_f$	Fan stream properties
$(\cdot)_c$	Core stream properties
$(\cdot)_0$	Stagnation properties
$(\cdot)_s$	Static properties

$(\cdot)_{amb}$	Ambient condition
$\overline{(\cdot)}$	Time averaged mean value
$\dot{(\cdot)}$	Flow rates

Abbreviations

LDV	Laser Doppler Velocimetry
RANS	Reynolds Averaged Navier-Stokes
LES	Large Eddy Simulation
DNS	Direct Numerical Simulation
FWH	Ffowcs-Williams- Hawkings
CFD	Computational Fluid Dynamics
LBM	Lattice Boltzmann Method
LBE	Lattice-Boltzmann Equation
BGK	Bhatnagar-Gross-Krook
SRT	Single Relaxation Time
RNG	Renormalization Group
VLES	Very Large Eddy Simulation
OASPL	Overall Sound Pressure Level
SPL	Sound Pressure Level
CONF	Confluent mixer
12CL	12-lobe, unscalloped, low-penetration mixer
20UH	20-lobe, unscalloped, high-penetration mixer
20MH	20-lobe, mediumly-scalloped, high-penetration mixer
20DH	20-lobe, highly-scalloped, high-penetration mixer
CAD	Computer Aided Design
STL	Stereolithography
VR	Variable Resolution
dB	Decibel
BPR	Bypass Ratio

ABSTRACT

The growing stringency of community noise regulations for commercial turbo-fan engines requires the development of effective jet noise suppression configurations. The lobed mixer has been previously found to be an effective noise reduction device for medium or low bypass engines typical of regional jet aircraft applications. The large number of geometrical design parameters for lobed mixers precludes trial and error experimental studies. In this study, a robust computational tool was used to investigate the effects of lobe number, penetration depth and scalloping depth on the sound radiated from a lobed mixer. The near field sound and flow were simulated using a flow solver based on the Lattice Boltzmann Method (LBM). The far-field radiated sound was predicted using the Ffwocs William-Hawkings (FWH) surface integral method. The Reynolds number based on jet diameter was 1.36×10^6 and the peak Mach number reached 0.5. The low-Mach setting was to abide by the constraints of the 19-stage LBM algorithm used in this study, with operating conditions selected to best approach the operating conditions of actual engines. The effects of an outer mean flow to simulate forward flight were not included.

Two groups of one quarter scale mixers were selected for investigation. Flow results and statistics were obtained. Plume survey data was obtained across transverse cross-sections of the jet at different downstream locations. Far-field overall sound pressure level (OASPL) and sound pressure level (SPL) directivity results were obtained. All lobed mixers configurations were found to be quieter than the baseline confluent mixer.

The results showed that a greater lobe number and a greater penetration depth leads to lower low-to-mid frequency noise, and relatively higher sound pressure levels at high frequency at locations far downstream. Lobed mixers were found to decrease the sound pressure level at mid frequencies, and to significantly decrease noise emissions at low frequencies.

The introduction of scalloping did not provide the same low-frequency noise reduction advantage as unscalloped mixers, but yielded noise reduction benefits at low frequencies compared to the baseline case. Deep scalloping tended to trade off low-frequency noise suppression for a noise decrease at high frequencies. The SPL directivity indicated the angle of maximum emissions changed with scalloping depth. The results were found to be in qualitative agreement with published experimental data.

Résumé

Les récentes mesures prises afin de règlementer le bruit provenant des turboréacteurs à double flux nécessitent le développement de nouvelles configurations de tuyères pour réduire le bruit de ces moteurs. Il a déjà été démontré que les mélangeurs lobés peuvent aider à réduire les émissions sonores. La construction des mélangeurs à lobes comprend un grand nombre de paramètres géométriques, ce qui rend difficiles les approches d'optimisation expérimentales pour trouver la configuration idéale. Dans la présente étude, un logiciel a été utilisé pour analyser l'effet du nombre de lobes sur les niveaux de bruit. Les effets de la largeur et profondeur des lobes, et la profondeur des festons furent aussi étudiés. L'écoulement et le bruit à proximité du jet ont été simulés en utilisant un logiciel basé sur la méthode de Boltzmann sur réseau (MBR). Le bruit en champ lointain a été prédit en utilisant la méthode analogique de Ffwocs-Williams et Hawkings. Le nombre de Reynolds, basé sur le diamètre du jet, était de 1.36×10^6, et le nombre de Mach maximum était 0.5. Le nombre de Mach est limité en raison de restrictions inhérentes au schéma de calcul MBR utilisé. Les paramètres de l'écoulement ont été choisis pour approcher les conditions de vol de vrais moteurs. Les effets d'un écoulement extérieur pour simuler le mouvement de l'avion ne furent pas pris en considération.

Deux groupes de mélangeurs à l'échelle d'un quart ont été sélectionnés pour cette étude. Les résultats et statistiques de l'écoulement instantané et moyenné ont été obtenus. Les données du panache ont été obtenues sur des coupes transversales à plusieurs positions en aval du jet. Les niveaux de pression acoustiques pondérés et la directivité du bruit ont été obtenus. Tous les résultats indiquent que les mélangeurs à lobes étudiés sont plus silencieux que le mélangeur confluent standard, tel qu'attendu.

Les résultats suggèrent qu'un plus grand nombre de lobes et une profondeur de pénétration plus prononcée sont préférables vis à vis les fréquences moyennes et basses, au prix d'émissions accrues en aval pour les fréquences élevées. Les mélangeurs à lobes semblent produire moins de bruit aux fréquences moyennes, mais

la réduction est plus prononcée pour le bruit à basse fréquence.

Les mélangeurs avec festons n'ont pas réduit le bruit à basse fréquence autant que les mélangeurs sans festons. Ceci semble indiquer que les festons à haute-profondeur sont préférables aux fréquences élevées et non aux basses fréquences. La directivité du bruit suggère un décalage de crête associé à la variation de la profondeur des festons. Les résultats obtenus sont en bon accord qualitatif avec les données expérimentales publiées dans la littérature.

Chapter 1 Introduction

1.1 Motivation

Government and airport regulations have implemented stricter regulations for aircraft noise emissions over the past decades. Aircraft noise has been found to cause physical and mental damage to the communities surrounding airports[1]. In the United States, a goal was stated in 1997 that the perceived noise levels of future subsonic aircraft would be reduced by a factor of two by 2007 and by a factor of four by 2022[2]. Jet noise is the dominant contributor to aircraft noise at takeoff. Noise reduction at the source requires a deep understanding of the turbulent flow processes responsible for the generation of sound radiated in the surrounding environment. Jet noise still remains one of the most elusive problems in aeroacoustics due to the complexity of the flow-generated sound processes.

For the case of subsonic single stream jets, noise is created by the turbulent mixing of the jet stream with the ambient air. For coaxial jets, additional noise may be generated by the mixing of the primary and secondary flows. Complex jet configurations can have additional mixing enhancement devices, such as lobed mixers or chevrons. Currently, there is no well developed industrial design tool for the prediction of the noise characteristics resulting from complex jet flows. As a result, the jet noise levels of modern turbofan jet engine configurations can only be determined through expensive experimental testing after they have been designed and built. The current study focused on noise predictions from jets with internal forced lobed mixers which are currently used in regional jet aircraft.

1.2 Lobed Mixers and Key Parameters

Reduction of jet noise has been sought earlier by mixing the hot core flow and the cooler fan flow before they exit through the nozzle. A more uniform flow at the nozzle exit plane leads to reduced noise levels. Uniform flow at the nozzle exit plane yields better cruise thrust efficiency thermodynamically than partially mixed flow or separate unmixed flow nozzle systems. That is the primary reason for mixing the flows internally. However, the overall noise benefit and penalty resulting from internal mixing to achieve the uniform exit flow is not well understood. The actual level of noise abatement realized in a specific application must be critically related to the manner and extent to which internal mixing is achieved. So far various kinds of devices proposed include confluent mixers, vortex generators, chevrons, exhaust tabs, diverters and lobed mixers. Among these devices tested, the lobed mixer configuration has been found to yield significantly enhanced mixing with acceptable pressure losses.

A lobed mixer is basically a splitter plate with a convoluted trailing edge which alternately diverts the upper and lower streams into the lobe troughs. The key parameters of a lobed mixer nozzle include lobe number, lobe penetration, scalloping shape, perimeter of the trailing edge and mixing length.

The lobe number is directly related to the wetted perimeter. By increasing the lobe number in the mixer, the interface area between the two flow streams is increased, which leads to an overall increase in turbulent mixing. However, this process is not entirely straightforward. Because all mixers must fit within the same duct cross-sectional area, increasing the number of lobes produces a corresponding decrease in lobe width and in diameter of the axial vortex shed from each lobe sidewall. The resulting changes in vortex growth, diffusion, and interaction substantially alter and complicate the mixing process. The possible acoustic benefit is offset by increases in skin friction and total pressure loss, which adversely affect thrust production. Other factors such as weight, blockage due to the lobe metal thickness, and the manufacturing of the mixers also need to be considered.

The introduction of scalloping to the lobed mixer allows the two streams to interact with each other gradually and further upstream. Because the two streams are not parallel near the lobe sidewall, their radial velocity components give rise to axial or streamwise vorticity shed from the leading edge of the scallop. Streamwise vorticity enhances mixing between two streams compared with mixing only due to Kelvin-Helmholtz type vortex-sheet instability.[3,4] Scalloping should be designed such that the vorticity is introduced gradually. The axial gradient at which net vorticity is introduced into the flow should be smooth and gradually increasing, presumably reducing the relatively high-frequency noise sources. In comparison, high-frequency noise generation is expected for unscalloped mixers because the two streams merge with each other suddenly after the exit of the mixer across the full height of the lobe, the generation of high-frequency noise is expected. To minimize the dipole noise, the scalloped edge should be shaped such that it acts as a trailing edge over its entire length with respect to both streams around it.

1.3 Previous Experimental Studies of Lobed Mixers

1.3.1   Mixing Mechanisms

A combination of several lobed mixer design parameters significantly affects the mixing process, thereby the associated noise generation.

It has been suggested that the mixing process in a lobed mixer is controlled by three major factors[4]. These are the streamwise vorticity generated by lobe shape, the increase in the interfacial area between the two fluid streams, and the Brown-Roshko type structures that occur in any free shear layer due to the Kelvin-Helmholtz instabilities. Manning[5] attempted to isolate the effects of these three mechanisms. He studied a flat plate as a baseline case and two different lobed mixers. Mixing performance of the lobed mixer exceeded the performance of the convoluted plate by an amount that increased with velocity ratio. At velocity ratios close to unity, the increased mixing was mainly due to the increased contact area, whereas the

streamwise vorticity had a larger role at a velocity ratio of two.

Paterson[6,7] studied subsonic flow issuing from a lobed nozzle for both cold and heated flows. Detailed pressure and temperature data were obtained as well as three dimensional laser Doppler velocimetry (LDV) measurements. Paterson found that large-scale secondary flows, set up by the nozzle, produced streamwise vortices of low intensity with a length scale on the order of the nozzle radius. Also, a horseshoe vortex on the order of the lobe half-width was found in the lobe troughs. The respective contribution of these flow features to the overall mixing process was not clear, but the secondary flow vortices were argued to be dominant because of their much greater size. Werle *et al.*[8] found that the vortex formation process was an inviscid one. Also, the mixing process was proposed to take place in three basic steps: the vortices formed, intensified, and then rapidly broke down into small scale turbulence. In effect, the lobed mixer was thought to act as a "stirrer" initially to mix the flow, until the rapid breakdown of the vortices produced small scale, and possibly, molecular mixing. Eckerle *et al.*[9] used a two component LDV to study mixing downstream of a lobed mixer at two velocity ratios. They determined that the breakdown of the large scale vortices, and the accompanying increase in turbulent mixing, was an important part of the mixing process. This vortex breakdown occurred further upstream for a velocity ratio of 2:1 than for 1:1. Barber *et al.*[10] studied both analytically and experimentally three different two-dimensional lobed mixers. Performing a one-dimensional inviscid analysis to predict lobe circulation and geometrical scaling relations produced results in reasonable agreement with their data, further emphasizing the inviscid nature of the overall large scale mixing process. One of the conclusions of that study was that lobed mixers with parallel side walls produced higher streamwise circulation than lobes with sinusoidal or triangular shapes. The close proximity of the walls in the lobe peak region for the triangular shapes created thicker boundary layers which reduced the effective lobe height and therefore reduced circulation. A detailed study by McCormick[11] revealed several more details of the flow patterns downstreams of a lobed mixer. Extensive flow visualizations and

three-dimensional velocity measurements showed that the interaction between Kelvin-Helmholtz vortices and the streamwise vortices produced high levels of mixing. The streamwise vortices pinched off the normal vortices, thus enhancing the stirring effect in the flow. This pinching caused the normal vortices to merge within 1.5 lobe heights downstream, where they were observed to break down shortly thereafter, leading to intense turbulent mixing. Another interesting observation by McCormick was that the scale of the normal vortices shed from the lobed mixer was about 25% of that shed from a planar baseline case. From this, McCormick and Bennet[12] inferred that the lobed mixer introduced smaller scales into the flow stream further upstream, which might enhance molecular mixing.

1.3.2   Evaluation of Lobed Mixers

Experimental research on lobed mixers has been extensive in the past few decades. Pioneering work by Frost[13] and Hartmann[14] showed the theoretical thrust gain for ideal mixing and presented results from turbofan engine scale model tests with nominal low bypass ratios. Since then, both far-field noise data for lobed mixers[15] and detailed measurements of aerodynamic properties[16,17,18] have been reported in the literature. Couch *et al.*[19] and Packman *et al.*[15] reported that jet noise could be reduced by mixing the turbofan engine fan and primary streams. Shumpert[20] investigated four types of internal mixers (confluent, injection, vortex generator, and lobed mixer) for turbofan engines with a nominal engine airflow bypass ratio of six. The experimental results were presented in terms of mixer nozzle pressure losses, mixing effectiveness, thrust gain, and primary thrust recovery. It was concluded that the lobed mixer favored rapid mixing of the two streams, and 70% of the ideal thrust gain was achievable. Kuchar's experimental study[17] on scale model performance first revealed the qualitative correlation between lobed mixer geometric properties and the engine performance. Their conclusion was that scalloping enhanced mixing with essentially no increase in mixer pressure loss. Kozlowski and Kraft [21] later conducted a similar study. They found that increasing the lobe number and radial penetration of a

lobed mixer within a certain range offered overall performance improvement. The introduction of scalloping was also found to be beneficial. Barber *et al.*[10, 22, 23] showed that a forced mixer reduced the exit jet velocity without significant thrust penalties for turbofan engines. Barber *et al.* also established the inviscid nature of the streamwise vortices formation at the mixer trailing edge. They compared streamwise circulation measurements near the trailing edge with analytical results based on the principle of two-dimensional continuity within the penetration region, and good agreement was obtained. Booher *et al.*[24] showed that lobed mixers with high penetration yielded substantial performance improvements at typical subsonic cruising relative to an unmixed nozzle configuration. According to their experimental results, the generation of streamwise vorticity and the rapid mixing of the fan and core streams downstream of the mixer yielded very high mixing effectiveness values with low total pressure losses. In an acoustic study of lobed mixers on a high bypass ratio engine, Meade[25] showed that internal forced mixing significantly reduced jet noise compared to internal confluent mixing. Publications by Presz *et al.*[26, 27, 28] again indicated that the enhanced mixing between the core and the bypass flows caused by the lobed mixer not only reduced jet noise, but also provided some gains on net thrust. Nevertheless, a systematic study on the effects of lobed mixer parameters is not practical without predictions from numerical simulations.

1.4 Jet Noise Prediction Methods

Computational simulations have been established as a primary tool for recent jet noise sound generation studies. Three basic approaches to computational aeroacoustics are the direct, the semi-empirical, and the indirect approach.

In the direct approach, the complete and fully coupled compressible Navier-Stokes equations are solved. The computational domain includes both the source region and the far-field observer. Sound generation and propagation phenomena are part of the solution. Because the acoustic perturbations are very small compared to the mean flow properties, high-order, low-dissipative, and low-dispersion schemes are required

to provide reliable results. Therefore, the direct approach is usually very expensive and suitable only for fundamental studies and academic configurations.

In the semi-empirical approach, a steady or unsteady Reynolds Averaged Navier Stokes (RANS) computation is performed to obtain information about turbulence length and time scales. This information is then transformed into sound-source spectra using empirical relations. This approach is inexpensive, but the reliability of the results is heavily dependent on the validity and accuracy of the empirical relations in the case being considered.

The indirect approach consists of two steps. The first step is to perform a detailed and accurate flow simulation in the near-field where all possible sources are contained in the computational domain using large eddy simulation (LES) or direct numerical simulation (DNS). The second step is to use an acoustic analogy method such as Lighthill's acoustic analogy, the Ffowcs-Williams-Hawkings (FWH) method, or the Kirchhoff surface integral method to obtain the far-field noise. This approach is less expensive than the direct approach and provides valuable information about the overall sound level and directivity in the far-field. Limitations include the neglect of flow-sound interactions and scattering through shear layers. In the present study, the indirect approach was adopted. The investigation was categorized into near-field flow simulation and far-field noise prediction.

1.4.1 Near-field Simulations

Previous researchers have performed calculations to capture the near-field flow features generated by lobed mixers. Povinelli and Anderson[29] developed a computer code that could predict the complex three-dimensional temperature contours within the mixing duct, however, their prediction largely depended on the accurate knowledge of the 3D velocity field at lobe exit for use as inlet boundary conditions. To tackle this problem, Barber *et al.*[30,31] and Koutmos and McGuirk[32] modeled the lobe flow itself. Malecki and Lord[33] and Abolfad and Sehra[34] later performed an analytical modeling of the mixer utilizing the full Navier-Stokes analysis and

provided some insight into the design of lobed mixers. In the last two decades, some researchers investigated lobed mixer flows using RANS computational fluid dynamics (CFD) analysis. Barber *et al.*[35] performed RANS simulations of jet flows with lobed mixers. Salman *et al.*[36,37] used both structured and unstructured grids to study lobed mixer jet flows. Garrison[38] carried out RANS calculations based on the WIND flow solver with a two-equation turbulence model, and the results were able to capture some features of lobed mixer flows.

Most numerical methods now involve the solution of some form of the basic equations of motion using finite difference schemes. With the continuous improvements in computing power, the application of DNS is now feasible in some cases[39,40]. The approach involves the simulation of the flow dynamics for all the relevant turbulence scales. Hence it requires no turbulence model. The wide range of time and length scales present in turbulent flows and the current computational resources limit the use of DNS for high Reynolds number flows. LES involves direct computation of the large scales, in conjunction with sub-grid scale models. It is assumed that the large scales in turbulence are generally more energetic than the small scales and are affected by the boundary conditions directly. In contrast, the small scales are more dissipative, weaker, and tend to be more universal in nature. Most turbulent jet flows that occur in experimental or industrial settings are at high Reynolds numbers. LES methods for high Reynolds number flows cost a fraction of DNS. One of the first uses of LES as an investigative tool for jet noise prediction was carried out by Mankbadi *et al.*[41] They performed a simulation of a low Reynolds number supersonic jet and applied Lighthill's analogy[42] to calculate the far-field noise. Lyrintzis and Mankbadi[43] used Kirchhoff's method with LES to compute the far-field noise. Other numerical studies[44,45,46] were then carried out by investigators at higher Reynolds numbers. A comprehensive overview of applications of LES to jet noise prediction was given by Uzun[47]. In general, the results have been found to be accurate, and in good agreement with experimental results.

However, the aforementioned simulations did not include a nozzle in the

computational domain, which precluded possible dipole contributions from the nozzle surfaces. Instead, *ad hoc* inflow conditions that typically include random Gaussian or pipe flow simulation output data as forcing were specified to mimic the nozzle exit plume. Although the exclusion of the nozzle reduces computational costs, inflow forcing tends to result in higher noise levels in the far-field compared to experiments. The inclusion of the nozzles in LES simulations is rather recent, and the works of Anderson *et al.*[48], Paliath and Morris[49], Schur *et al.*[50], and Uzun and Hussaini[51] are the most notable. The simulation results obtained following the inclusion of the nozzle geometry did improve the far-field noise prediction but at the expense of computational cost. Even if the computational expense with the addition of the nozzle is acceptable, the setup for these simulations includes tedious body-fitted meshing for complex geometries. Thus, despite recent progress in computational aeroacoustics, detailed LES studies remain largely confined to academic jet configurations.

Hence, computational tools with high accuracy, high efficiency, stability, and relatively low cost have to be developed to uncover the flow and noise characteristics resulting from complex jet flows, such as lobed mixer flows. The tool based on the Lattice Boltzmann Method (LBM) is a potential candidate in addition to Navier-Stokes based methods, and it was employed in the present study.

Recent advances have been made in kinetic based methodologies such as the lattice-Boltzmann method (LBM). These methods have been shown to be accurate for the simulation of complex fluid phenomena[52]. While Navier-Stokes equations solve the macroscopic properties of the fluid explicitly, LBM solves the Lattice-Boltzmann equation (LBE) by explicitly tracking the development of particle distribution functions either at the mesoscopic or the microscopic scale. Through the use of the Chapman-Enskog expansion[53], the LBE has been shown to recover the compressible Navier-Stokes equation at the hydrodynamic limit[52, 54, 55]. The conserved variables such as density, momentum and internal energy are obtained by performing a local integration of the particle distribution. The LBM has been recently applied to aeroacoustic problems. Lew *et al.*[75] applied LBM to study the far-field noise

generated from an unheated round jet of Mach 0.4. The predicted far-field sound pressure levels were within 2 dB from experimental data. Lew *et al.*[56] conducted a study to predict the noise radiation from a round jet with impinging microjets using LBM. The results were found to be in qualitative agreement with experimental observations. Habibi *et al.*[57] used LBM to investigate the aeroacoustic problem of low-Mach heated round jets. Qualitative comparison between simulated results and experimental data supported the viability of the LBM schemes application. More detailed background of LBM is discussed in section 1.5.

1.4.2 Far-field Sound Predictions

In the indirect approach, the flow field data is usually post-processed using the acoustic analogy to determine the far-field sound. The acoustic analogy was first formed by Lighthill[42] through the derivation of an equation to describe aerodynamically generated noise by rearranging the Navier-Stokes equations. In particular, Lighthill derived the acoustic analogy by combining the continuity and momentum equations. He then formed a wave equation on the left-hand side and moved all other terms to the right-hand side. In this form, the wave operator on the left-hand side represents the propagation of the sound and the terms on the right-hand side are regarded as known source terms that are responsible for the generation of the sound. Further developments have been made to the standard acoustic analogy developed by Lighthill to account for noise sources that are embedded in a mean flow. Lilley derived another acoustic analogy[58], and the governing equation is linearized for a parallel sheared mean flow, which is representative of the mean flow in a jet. The advantage of this approach is that in addition to the propagation of the sound it also accounts for the refraction of sound waves in the jet mean flow.

In the current study, a modified porous FWH surface integral acoustic method[59] was used to predict the far-field noise. An FWH formulation is the generalization of Lighthill's equation to account for the effect of a moving solid surface. The formulation source terms include monopoles, dipoles, and quadrupoles. The surface

integral method follows the description of Lyrintzis & Uzun[60] and Lyrintzis[61]. For simplicity, a continuous stationary control surface around the turbulent jet was used. Details regarding the numerical implementation of the FWH method can be found in Uzun[47].

1.5 Lattice-Boltzmann Method

The Lattice-Boltzmann equation has the following form[52, 53]:

$$f_i(x + c_i \Delta t, t + \Delta t) - f_i(x, t) = -\frac{\Delta t}{\tau}(f_i(x, t) - F_i(x, t)), \qquad (1.1)$$

where the distribution function $f_i(x,t)$ yields the number density of kinetic particles at position, x, with a particle velocity c_i in the i direction at time t. The left-hand side of (1) computes the particle advection from one center cell to another whereas the right-hand side of (1), known as the collision operator, represents the relaxation of the particles. The Bhatnagar-Gross-Krook (BGK) approximation[62] is used to relax the equilibrium distribution function $F_i(x,t)$. The relaxation time τ, however, is related to the kinematic viscosity, ν, such that $\tau = (\nu + \Delta t)/T$. This relation is also commonly referred to as single relaxation time (SRT). The conservative macroscopic variables, such as density and momentum density, are obtained through the zeroth and first-order moments of the distribution function:

$$\rho(x,t) = \sum_i f_i(x,t), \qquad \rho u(x,t) = \sum_i c_i f_i(x,t). \qquad (1.2)$$

The pressure is obtained using the equation of state for an ideal gas with the assumption that the gas constant is taken to be unity. This can be expressed as $p=\rho T$. In addition, the LBM approach recovers the compressible, viscous Navier-Stokes equation in the hydrodynamic limit for wavelengths $\lambda \gg \Delta x$ and frequencies $f \ll \Delta t/\tau$. To recover the macroscopic hydrodynamics, $F_i(x,t)$ must be chosen in such a way that the essential conservation laws are satisfied and the resulting macroscopic equations are Galilean invariant. In the three-dimensional situation, one of the common choices is the D3Q19 model[63] shown in Figure 1.1:

$$F_i = \rho w_i \left[1 + \frac{c_i \cdot u}{T} + \frac{(c_i \cdot u)^2}{2T^2} - \frac{u^2}{2T^2} + \frac{(c_i \cdot u)^3}{6T^3} - \frac{c_i \cdot u}{2T^2} u^2 \right], \qquad (1.3)$$

where w_i has the weighting parameters of 1/18 in the 6 coordinate directions, 1/36 in the 12 bi-diagonal directions and 1/3 for the 'rest' particle. T is the lattice temperature, which is set to 1/3 for isothermal simulations. The LBM used in this study has been shown to be second-order accurate in time and space[64].

To account for the presence of solid boundaries in the simulation, the no-slip boundary condition used a simple particle bounce back and reflection process on a solid surface[64]. In addition, an improved volumetric boundary scheme for arbitrary geometries has been devised and implemented to accurately control and govern the momentum flux across the boundary. Further details regarding the handling of solid geometries can be found in references[64, 65].

To include the unresolved turbulent scales, an eddy viscosity turbulence model was used. Specifically, the commercial code used in this study employed the two-equation k-ε renormalization group (RNG) turbulence model to compute the turbulence viscosity with the addition of a swirl corrector to model part of the large scale structures. This methodology is also commonly referred to as very large eddy simulation (VLES). This procedure has been argued to be analogous to an LES[66].

The potential advantages of LBM over the conventional Navier-Stokes solvers include: 1) linearity of the convection operator (Equation (1.1)) due to the kinetic nature of the LBE method; 2) easy calculation of the strain rate from the non-equilibrium distribution function; 3) suitability for complex geometries, due to the absence of Jacobians to compute grid metrics; 4) ease of parallelization for large to massive supercomputing architectures due to its simplicity in terms of form.

The most notable disadvantage is that the LBM does not recover flow physics correctly for cases with high Mach numbers (M > 0.5). Efforts are being made to extend the current LBM for higher Mach number jet flows. Recently, Sun and Hsu[67] used an LBM technique to study a shock tube problem and obtained good results compared to the Reimann solution. Shan *et al.*[68] and Chen *et al.*[69] have laid a firm

theoretical groundwork to efficiently extend the LBM to higher Mach numbers and arbitrary Knudsen numbers. Recently, Li *et al.*[70] devised a modified Boltzmann equation and applied it to a 2D aeroacoustic benchmark problem. They obtained good results and showed that their methodology is valid up to a Mach number of 0.9.

1.6 Research Objectives

Investigating the impact of various parameters of a lobed mixer on the generated noise requires a systematic study; however, the underlying mixing mechanism is affected by only three main factors[4]. Through a comprehensive study of several key parameters, some understanding of these underlying physical mechanisms can be obtained and used for a better mixer design. The objective of this study is, therefore, to investigate the three most important lobed mixer parameters on noise suppression: lobe number, penetration depth, and scalloping effects. One group of three mixers was selected with the aim to uncover the compound effect of increased lobe number and penetration depth, which is equivalent to the effect of increased interface area. The second group of four mixers was chosen to investigate the far-field sound pressure level differences caused by different scalloping depth. Another goal of the study is to showcase the capacity and applicability of the LBM scheme in simulating complex jet flow.

1.7 Organization of the Thesis

This thesis is organized as follows. In chapter 2, five different mixer-nozzle configurations are introduced, and the setting of grid distribution and measurement windows in the simulation is discussed. The characteristic parameters, initial condition, boundary conditions, and the use of forcing function are also presented. In chapter 3, three mixers are selected to study the compound effect of lobe number and penetration depth. Both instantaneous and time-averaged flow results and statistics are presented. Plume survey data is given. Overall sound pressure level (OASPL) and sound pressure level (SPL) directivity results are shown for the three mixers to

analyze the far-field radiated noise. In chapter 4, three scalloped mixers along with a confluent mixer are investigated for the aerodynamic and acoustic effect of scalloping. The same set of simulation results as those in chapter 3 is given and compared among the four mixers. Chapter 5 summarizes the results and gives an outlook on future work.
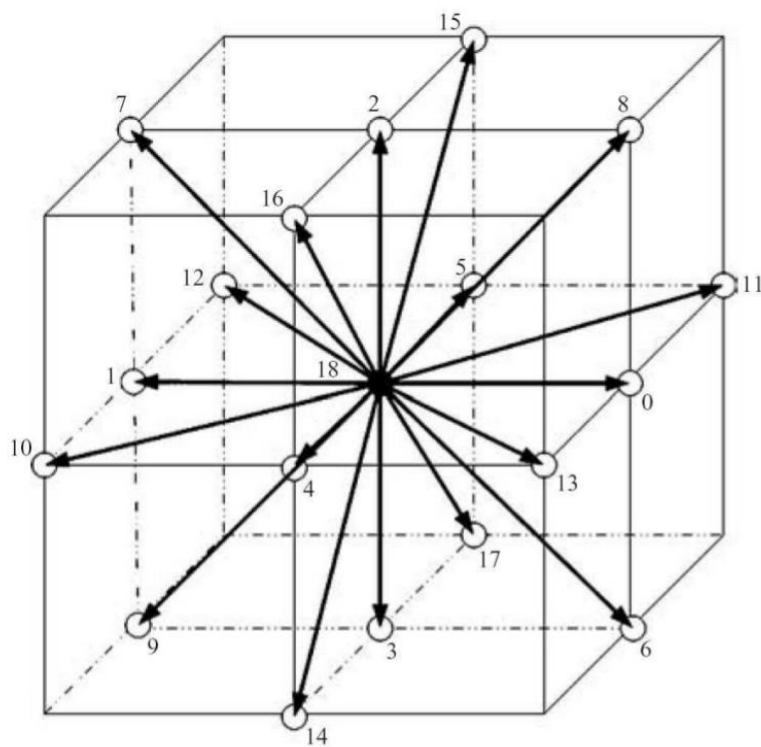
Figure 1.1: Schematic of the D3Q19 LBM Model[71].

Chapter 2 Numerical Procedures

In this chapter, the five selected mixer configurations are briefly described. The configuration of the computational grid distribution and measurement window is discussed. The characteristic parameters, initial condition, and adjusted inflow boundary conditions are given. Although the simulations were conducted without heat transfer, a verified approach was applied to approximate heated flow conditions with isothermal conditions. The use of artificial forcing techniques is presented at the end. The simulations were performed using a commercial LBM code (i.e., PowerFLOW 4.3d) for a maximum Mach number below the upper limit of 0.5.

2.1 Lobed Mixer and Nozzle Models

Five lobed mixer-nozzle geometries were extracted from a NASA report[72]: confluent mixer (CONF); 12-lobe, unscalloped, low-penetration mixer (12CL); 20-lobe, unscalloped, high-penetration mixer (20UH); 20-lobe, mediumly scalloped, high-penetration mixer (20MH); and 20-lobe, highly scalloped, high-penetration mixer (20DH). Figure 2.1 shows the mixer-nozzle configurations. All mixer-nozzle configurations have common inner flow lines and consist of three parts: nozzle, mixer, and center-cone. Mixer key parameters are listed in Table 2.1. Figures 2.2 and 2.3 illustrate the mixer-nozzle configuration and five test models. The selected nozzle geometry is the same for all five configurations. The converging nozzle diameter decreases from about 261.37mm at the inlet to 184mm at the nozzle exit plane. The nozzle has a nominal mixing length, L, of 279.4mm which yields a mixing length to mixing plane diameter ratio (L/D_{mp}) of about 1.10.

The confluent mixer was used as the baseline reference configuration. Acoustic data obtained from the previous tests[72,73] confirmed that aggressive, high-penetration,

unscalloped mixer configurations suppressed low-frequency noise emissions, which are characteristic of unmixed, coaxial turbofan exhausts, but also produced greater emissions at higher frequencies. Previously presented data[74] for scalloped sidewall mixers shows that they reduced low frequency emissions without incurring a penalty at the higher frequency regimes. Hence, it can be inferred that the scalloping on the mixer sidewall can be beneficial to the overall sound pressure level reduction. This is the reason why 20UH, 20MH, and 20DH mixers were included in this study. These three mixers were designed for NASA tests[72] and varied parametrically in the scalloping depth and shape while holding all other parameters fixed. The purpose of studying this group of mixers is to discover the impact of different sidewall scalloping on far-field sound radiation. Meanwhile, the 12CL mixer was selected to gauge the combining effects of different lobe number and penetration depth.

The mixer-nozzle solid boundaries were incorporated into the computational domains as follows. A solid model was created using CAD software and then imported into the code as a stereolithography (STL) file format. The STL file contained the information representing the surface features of a 3D body of the mixers. The interaction between a surface mesh and a discrete voxel generated a surface element. This element acted as a boundary lattice element that imposed a no-slip boundary condition on the flow field via the bounce-back scheme which is utilized in LBM[56]. Despite the very complex shape of the lobed mixers, the LBM approach allows relatively easy geometries import.

2.2 Geometries Configurations

2.2.1   Simulation Domain and Variable Resolution Regions

The dimensions of the computational domain were $(x,y,z)=(37D_j, \pm15D_j, \pm15D_j)$. The domain length was sufficiently long to include twice the length of the jet core, as well as a sponge layer to dissipate and absorb the reflected acoustic waves. The outermost contour in Figures 2.4 and 2.5 illustrates the outer boundary of the

computational domain.

The computational domain was partitioned into several variable resolution (VR) regions to tailor the grid as needed to resolve the flow details and reduce computational costs. This methodology is similar to grid-stretching techniques typically employed in CFD. Figure 2.4 shows a side view of the computational domain. Successive VR regions were concentric and cylindrical as shown in Figure 2.5, but the voxels are cubic. The second outermost rectangular bounding region shows the inner boundary of the sponge layer. Sufficient spacing must be provided between successive VR regions radially and in the streamwise direction. Simulation with no spacing in the streamwise direction between VR regions usually causes "VR tones" to be generated in the far-field pressure spectra. These tones can have very significant levels of 15 dB above the underlying broadband spectral density levels[75], and therefore bias the overall spectrum. Sufficient streamwise spacing between VR regions eliminated these tones to a large extent. Each grid cell is called a "voxel". Hence, each VR region represented one grid resolution level and the VRs cascaded outwards from the fine resolution region towards the coarse resolution region. The voxel cell size between each successive VR region differed by a factor of two to keep the lattice velocity directions consistent between VR interfaces. The domain included a total of around 76 million voxels. The entire simulation domain was divided into seven VR regions. To the same end, coarse VR regions further away from the jet dissipated the outgoing traveling waves and thus acted as 'sponge' zones. In addition, an anechoic sponge layer with depth equivalent to five jet diameters was inserted between the two outermost rectangular VR regions to minimize acoustic wave reflection. Close-up views of the VR regions near the nozzle geometry are shown in Figures 2.6 and 2.7. Figure 2.8 shows the voxel distribution over the entire domain. Figures 2.9 and 2.10 show a close-up view of the voxel distribution inside the nozzle. Figure 2.11 shows the voxel distribution at the nozzle exit.

Inside the nozzle, voxels of size 4.25×10^{-4} m were distributed very close to the solid boundaries of the nozzle, the mixer, and the center-body (Figures 2.9 and 2.10)

to accurately capture the boundary layer characteristics. A high resolution in regions of high shear is required for accurate sound production modeling. The smallest voxel size corresponds to approximately $\Delta r/D_j \approx 0.09$ which may be considered coarse for wall-bounded flow studies. The ratio needed to resolve the duct boundary layers is at least one order of magnitude lower without the implementation of a wall model, which is prohibitively expensive. Although the adopted cell size did not fully resolve the boundary layer details, a carefully selected artificial forcing technique was utilized to perturb the flow within the boundary layer to achieve physical jet inflow conditions. The forcing function used in this study is discussed in section 2.3.2. A VR region with second resolution level was placed right off the finest level to act as a smooth transition from the smallest to coarser grids in the outer region.

The shear layer is a major contributor to the far-field sound radiation due to the large velocity gradients and turbulence levels. Possible flow separation downstream of the center-body may also generate flow patterns with high turbulence intensity, which also contribute to the far-field sound. A second finest VR level was therefore put at the downstream of both the mixer and the center-body to resolve the shear layer, vortex shedding and flow separation. A comparison between initial and later studies showed a satisfactory improvement on the resolved flow pattern when the second finest VR level (Figure 2.9) was added.

Outside the nozzle, two finest cylindrical VR regions were placed downstream of the nozzle tip to capture the initial development of turbulence in the shear layer. In addition, a larger VR region with third finest resolution level was located further downstream of the nozzle exit to yield a smooth transition to the outer coarser VR regions. Experience from previous simulations showed that the shear layer and vortex shedding features generated from the mixer tip have their footprint downstream close to the nozzle exit. Therefore a third VR level was added to properly cover that region (Figures 2.6 and 2.9).

2.2.2   Measurement Windows

Two volume measurement windows and one surface measurement window were used in the simulation. A rectangular streamwise measurement window with a thickness of two lattice lengths was placed at the symmetric plane of the simulation domain, as indicated in Figure 2.12. This measurement window was used to check the flow evolution and convergence and to generate snapshots of transient and time-averaged flow fields. The flow data was recorded every 100 time steps, from the establishment of flow convergence to the end of the simulation.   Meanwhile, a cylindrical measurement window was inserted in the near field. The window had an initial diameter of $2D_j$ and a diameter of $6D_j$ at the end. It started upstream of the nozzle inlet and extended to the downstream of the FWH surface measurement window, with a length of $22D_j$. This measurement window was mainly used for the analysis of the near flow field, such as the turbulence kinetic energy, the center-line mean velocity decay rate, the plume survey, and the 3D Lamda-2 criteria isosurface. Due to the large amount of data included in the measurement window at each frame, the data was sampled every 500 time steps and recorded after the establishment of flow convergence to the end of the simulation.

A surface measurement window was utilized for the near-field sound data recording, as indicated in Figure 2.13. This surface acted as a porous control surface in the FWH surface integral method. For simplicity, a continuous stationary surface around the turbulent jet was used. The funnel-shaped control surface started slightly upstream of the nozzle exit and had an initial diameter of $3D_j$. It extended streamwise over a distance of 21 D_j and had diameter of $18D_j$ at the end. The shape of FWH surface was reasonable compared to previous simulations[75], and the size was large enough to include the jet potential core. The entire surface remained in the same VR level to avoid different data sampling rates and different resolved Strouhal numbers. The end of the surface also managed to keep a reasonable distance from the VR transition to avoid spurious noise source caused by the VR tones. No data recording surface was present at the two ends of the FWH surface to avoid spurious sound

caused by interaction between the surface and vortices. Flow data was collected on the control surface at every 87 time steps over a period of 500,000 time steps. The sampling data was recorded after the first jet plume and the first reflected acoustic wave exited the computational domain. Based on the variable resolution around the control surface, and assuming that LBM required 12 cells per wavelength to accurately resolve an acoustic wave, the maximum resolved frequency corresponded to a Strouhal number of three.

2.2.3   Inlet and Outlet Geometry

As shown in Figure 2.14, two annular surfaces were located at the inlet of the nozzle and were fitted into the fan and core inflow area to help impose the inlet boundary conditions.

Six planar rectangular surfaces were located at the boundaries of the simulation domain to help impose the outlet boundary conditions. The surface at the outlet of the computational domain is shown in Figure 2.15 as an example.

Four ring-shape surfaces were extracted from the solid mixer-nozzle geometries to help define the forcing for the inflow perturbation. The application of the forcing was referred to the trip procedure used by Bogey & Baily[76], and the forcing surfaces were placed close to the inlet with a length of approximately $0.1D_j$. Figure 2.16 shows the four surfaces used for the forcing of the nozzle, mixer (both upper and lower surface), and center-body.

2.3 Parameters and Operating Conditions

2.3.1   Characteristic Parameters

The characteristic parameters used in all the simulations are listed in Table 2.2. The values were used to establish a dynamic range for the simulation case. Table 2.3 shows the grids points used in each case.

The atmospheric pressure was selected as the characteristic pressure (p_{char}) when

specifying the initial and boundary conditions and calculating the characteristic density (ρ_{char}). It was assumed to be approximately in the average of the pressure range encountered in the cases. The characteristic velocity (V_{char}) was selected to be the inflow velocity of the core stream. It was used to calculate the simulated Reynolds number (Re). The detailed calculation of V_{char} is discussed in section 2.3.2. The characteristic temperature (T_{char}) was selected by the usual isothermal test conditions. It was also used to calculate ρ_{char}. The characteristic viscosity (ν_{char}) was chosen by the air viscosity at T_{char}. The characteristic length (L_{char}) was selected to be the nozzle exit plane diameter. The value was used to calculate the smallest grid size and the Re. The resolution (Δr) was defined as the number of the smallest grid points along the characteristic length. It specified the size of grids and surfels in the case. The smallest grid size was calculated as the ratio of L_{char} and Δr. The value in this case was selected after careful consideration of the trade-off between accuracy and computation time. The flow Mach number is limited to values below 0.5 in the LBM scheme. In this range, flow results are approximately independent of Mach number. The flow field converges more rapidly when running a simulation at higher Mach number because the particles comprising the digital fluid move faster on the voxel lattice. This is part of the reason why the inflow boundary conditions were chosen such that the jet velocity at the nozzle exit reached a Mach number of 0.5. The simulation was performed at the same Mach number as experiments, which means acoustic waves were assumed to propagate at the same rate relative to the main flow as they do in experiments. The simulation time (t_s) of a million time steps was considered sufficient for the flow to reach a steady state, and for the FWH surface to obtain enough sampling data for the far-field sound analysis. In LBM, the time step size was determined from T_{char}, L_{char} and resolution, and it was calculated as follows:

$$t_{ts} = \frac{K}{\sqrt{T_{char}} \times \dfrac{\Delta r}{L_{char}}} \tag{2.1}$$

where t_{ts} is the simulated physical time in one time step, and the constant K=0.0288 s/m. Turbulence intensity of 5% is the common value for flow conditions within

turbomachinery devices. It should be noted that the overall actual turbulence intensity value was the sum of 5% and the values specified in the forcing function. The turbulence length scale defined the mean size of the turbulent eddies and the value used in the current study was common for external flows.

2.3.2   Initial Conditions, Inlet and Outlet Boundary Conditions

The initial condition specified the initial pressure and three velocity components for the simulation case. The initial pressure was set to be equal to the characteristic pressure. Because no free stream effect outside the nozzle was considered in this study, the initial velocity was set to zero.

Because the computational domain was far larger than the nozzle, the pressure value at the outlet boundary was considered constant and equal to the atmospheric pressure. For the same reason, velocity components were not specified at the outlet to avoid imposing a flow direction.

The inlet boundary conditions imposed on the fan and core stream were extracted from the NASA report[72]. Total pressure ratios of the fan (NPR_f) and core (NPR_c) streams, total temperature ratio (NTR), mass flow rates for fan ($\dot{m}_f$) and the core streams ($\dot{m}_f$) were obtained from the experimental data to calculate the static pressure and mean velocity values. The calculation was based on the assumption of an isentropic flow condition, therefore it is an approximation. The relations used in the fan stream calculation are as follows:

$$\dot{m}_f = \rho_f \cdot A_f \cdot v_f \tag{2.2}$$

$$NPR_f = p_{0,f} / p_{amb} \tag{2.3}$$

$$p_{0,f} = p_{s,f} + \frac{1}{2}\rho_f \cdot v_f^2 \tag{2.4}$$

$$T_{s,f} = T_{amb} = 300K \tag{2.5}$$

$$p_{s,f} = \rho_f \cdot R \cdot T_{s,f} \tag{2.6}$$

From the input values of NPR_f and $\dot{m}_f$, v_f, $p_{s,f}$ and ρ_f were calculated and then used in the calculation of core streams parameters. The relations used in the core stream calculation are:

$$\dot{m}_c = \rho_c \cdot A_c \cdot v_c \tag{2.7}$$

$$NPR_c = p_{0,c}/p_{amb} \tag{2.8}$$

$$NTR = T_{0,c}/T_{0,f} \tag{2.9}$$

$$p_{0,c} = p_{s,c} + \frac{1}{2}\rho_c \cdot v_c^2 \tag{2.10}$$

$$T_{0,c} = T_{s,c} + \frac{1}{2}\frac{v_c^2}{C_p} \tag{2.11}$$

$$T_{0,f} = T_{s,f} + \frac{1}{2}\frac{v_f^2}{C_p} \tag{2.12}$$

$$p_{s,c} = \rho_c \cdot R \cdot T_{s,c} \tag{2.13}$$

From the input values of NPR_c, $\dot{m}_c$, NTR, and v_f, the values of v_c, $p_{s,c}$, ρ_c, $T_{s,c}$ were obtained.

The inflow data was from experiments conducted at a high Mach number subsonic flow. Because of the limitations of the current adopted LBM scheme has an upper limit of simulated Mach number 0.5, the calculated inflow conditions were adjusted. The velocity ratio of the isothermal flow was modified using the formulation by Greitzer et al.[77] to approximate the heated flow field using isothermal flow simulations. The approximation can be regarded as an extension of the Munk and

Prim substitution for steady isentropic flows to non-isentropic flows. The adjusted operating conditions are listed in Table 2.3. A comparison between the simulated operating conditions in the current study and the experimental test conditions in previous studies[72] is shown in Table 2.5.

A hyperbolic tangent velocity profile was used to mimic the fully turbulent velocity profile at the nozzle inlet. The formulation was given by Freund[78]:

$$\bar{v}(r) = \frac{1}{2}\bar{v}\left[1 - \tanh\left[b\left(\frac{r}{r_0} - \frac{r_0}{r}\right)\right]\right],\tag{2.14}$$

where $r = \sqrt{x^2 + y^2}$, $r_0=1$, b is a constant, and v is the mean inlet velocity for fan or core stream.

In order to match with the actual turbulent intensity level and to perturb the boundary layer close to the nozzle tip, a forcing procedure[76] was followed. The boundary layer was perturbed close to the nozzle inlet. Random velocity fluctuations of low amplitude were added in the boundary layer to generate negligible spurious acoustic waves. These fluctuations were random both in time and space, whereas they were based on vortical disturbances decorrelated in the azimuthal direction as in LES schemes. The tripping magnitudes were empirically chosen to obtain, at the nozzle exit, a turbulence intensity of 5%. In this study, the three forcing velocity components were applied in the following way:

$$\begin{Bmatrix} v_r \\ v_\theta \\ v_z \end{Bmatrix} = \begin{Bmatrix} v_r \\ v_\theta \\ v_z \end{Bmatrix} + \alpha v_j \begin{Bmatrix} \varepsilon_r(r,\theta,z,t) \\ 2\varepsilon_\theta(r,\theta,z,t) \\ 3\varepsilon_z(r,\theta,z,t) \end{Bmatrix},\tag{2.15}$$

where $\varepsilon_r(r,\theta,z,t)$, $\varepsilon_\theta(r,\theta,z,t)$, and $\varepsilon_z(r,\theta,z,t)$ were random numbers between -1 and 1 updated at every time step and at every grid point. $\alpha = 0.00625$ was used here to achieve the desired turbulence intensity level.

Mixer ID	Lobe Penetration H_m/H_{mp}	Scalloping Depth L_s/H_m	Area Ratio A_f/A_c
[*]CONF	N/A	N/A	2.34
[†]20UH	0.48	0	2.34
[‡]20MH	0.48	0.399	2.34
[§]20DH	0.48	0.686	2.34
[**]12CL	0.41	N/A	2.34

Table 2.1: Mixer geometric parameters.

*Confluent mixer; †20 lobe unscalloped mixer with high penetration; ‡20 lobe medium scalloped mixer with high penetration; §20 lobe highly scalloped mixer with high penetration; **12-lobe unscalloped mixer with low-penetration.

p_{char}	101,000 Pa
V_{char}	67.32 m/s
T_{char}	300 K
ν_{char}	15.75×10^{-5} m^2/s
L_{char}	0.1847 m
Re	1.36×10^6
Δr	435
Simulated highest Mach number	0.5 (Same as experiment)
t_s	1,000,000 time steps
t_{ts}	6.918×10^{-7} s
Turbulent intensity	5%
Turbulent length scale	0.0129 m (0.07 ×characteristic length)

Table 2.2: Numerical simulation characteristic parameters.

Mixer ID	Grid Points
CONF	80,244,840
20UH	89,619,083
20MH	87,906,996
20DH	86,032,136
12CL	85,677,722

Table 2.3: Grid points of each cases.

NPR_f	1.23
NPR_c	1.18
$T_{0,c}/T_{0,f}$	1.01
m_f	3.45 kg/s
m_c	1.15 kg/s
BPR	3
V_f	83.67 m/s
M_f	0.24
V_c	67.32 m/s
M_c	0.19
$p_{s,f}$	119,259.2 pa
$p_{s,c}$	117,017.4 pa
T_f	300 K
T_c	303.7 K
ρ_f	1.39 kg/m^3
ρ_c	1.34 kg/m^3

Table 2.4: Inflow operating conditions.

Mixer ID	Simulation Operating Condition					Experimental Operating Condition				
	NPR_f	NPR_c	$T_{0,c}/T_{0,f}$	V_f (m/s)	V_c (m/s)	NPR_f	NPR_c	$T_{0,c}/T_{0,f}$	V_f (m/s)	V_c (m/s)
CONF	1.22	1.18	1.01	83.67	67.32	1.44	1.40	2.34	129.0	148.7
20UH	1.22	1.18	1.01	83.67	67.32	1.44	1.39	2.50	129.0	160.8
20MH	1.22	1.18	1.01	83.67	67.32	1.44	1.39	2.50	129.0	160.8
20DH	1.22	1.18	1.01	83.67	67.32	1.44	1.39	2.50	129.0	160.8
12CL	1.22	1.18	1.01	83.67	67.32	1.44	1.40	2.35	129.0	149.3

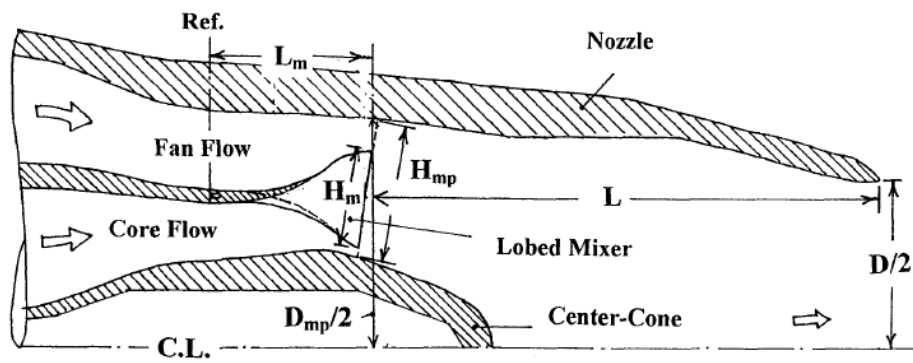Table 2.5: Operating conditions of the current study and previous experiments.

Figure 2.1: Schematic of the mixer-nozzle configuration.
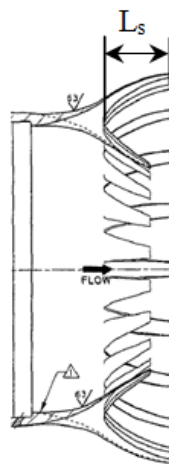
Figure 2.2: Sketch of a scalloped mixer.
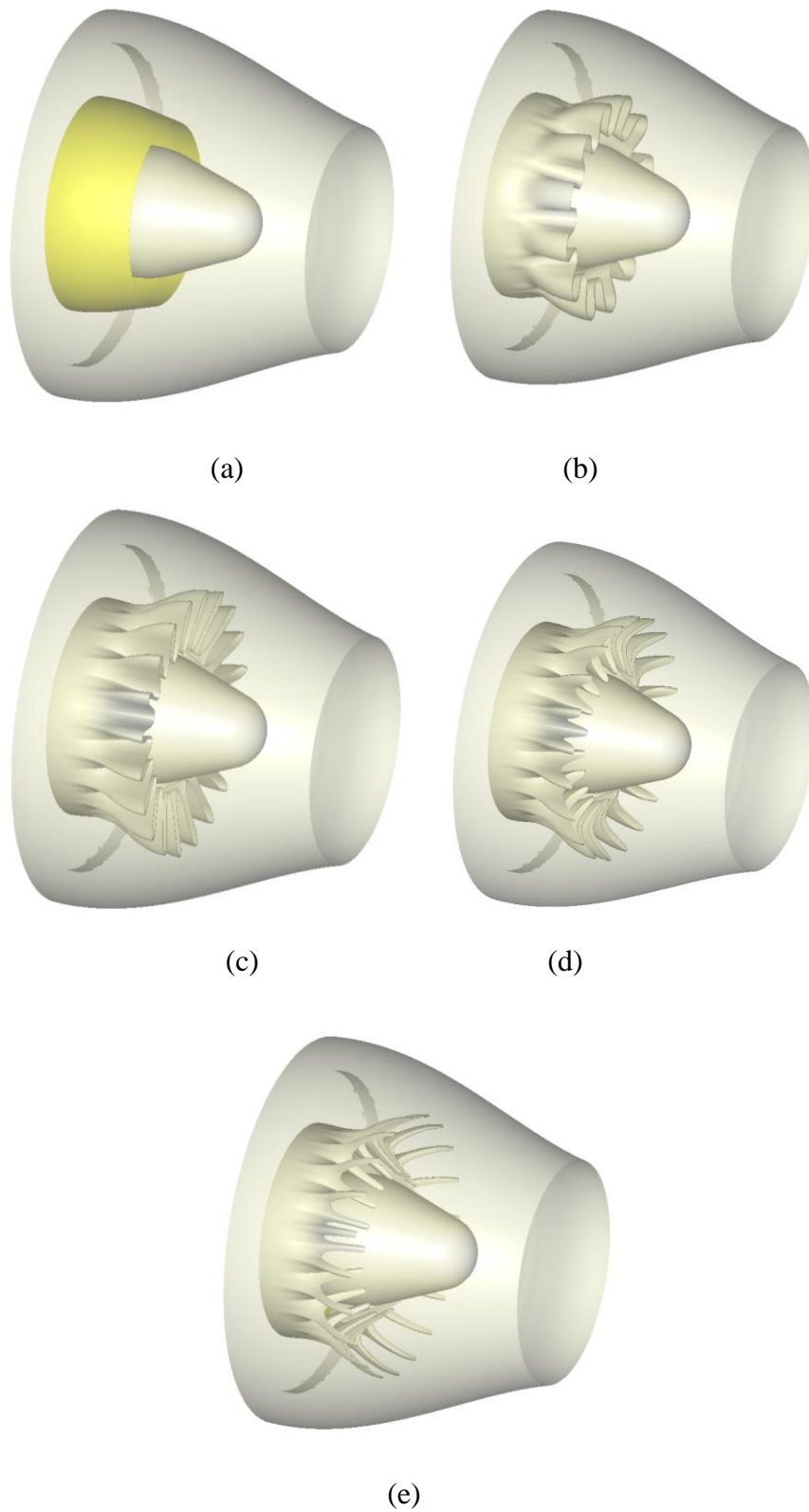
Figure 2.3: Drawings of the five mixer models. (a): CONF; (b): 12CL; (c) 20UH; (d) 20MH; (e) 20DH.
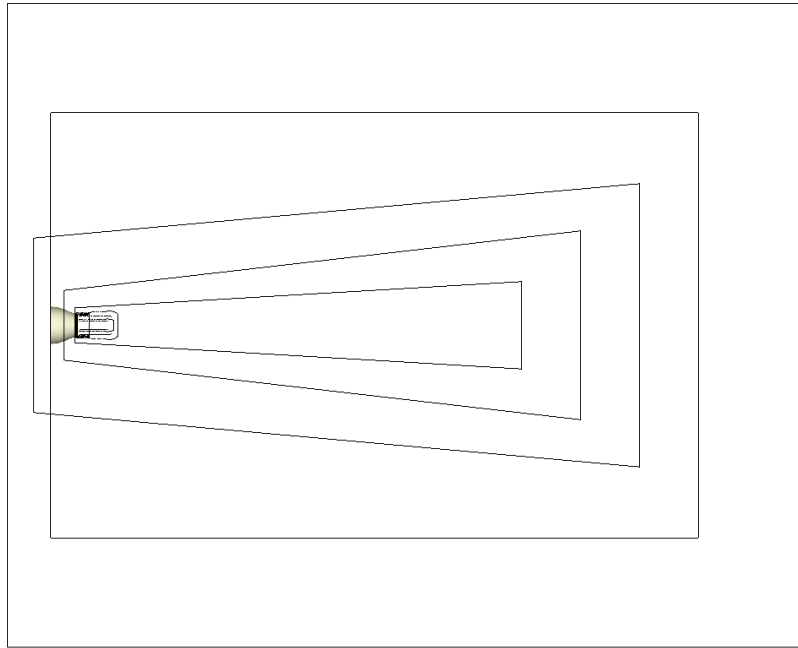
Figure 2.4: Streamwise view of the computational domain and VR regions.
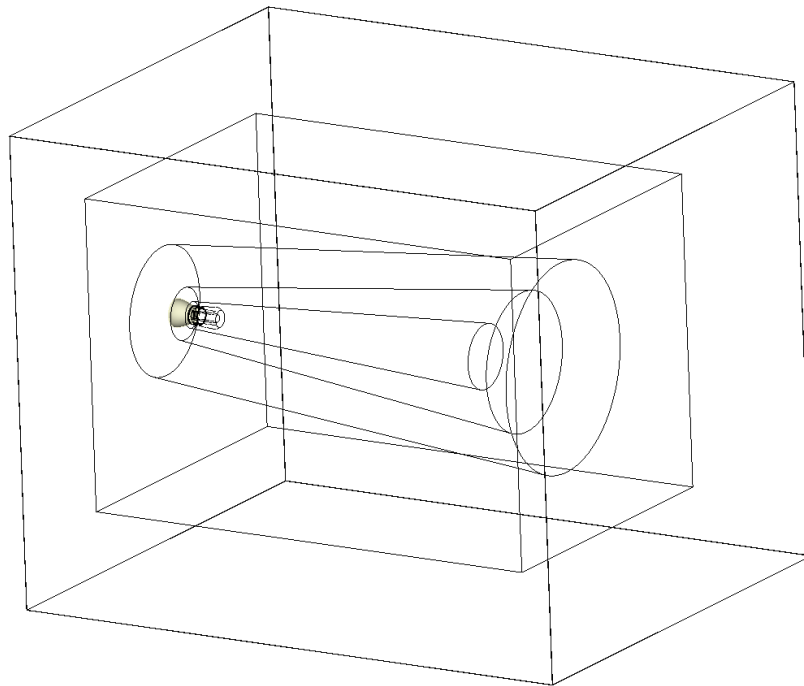
Figure 2.5: A different view of the computational domain and VR regions.
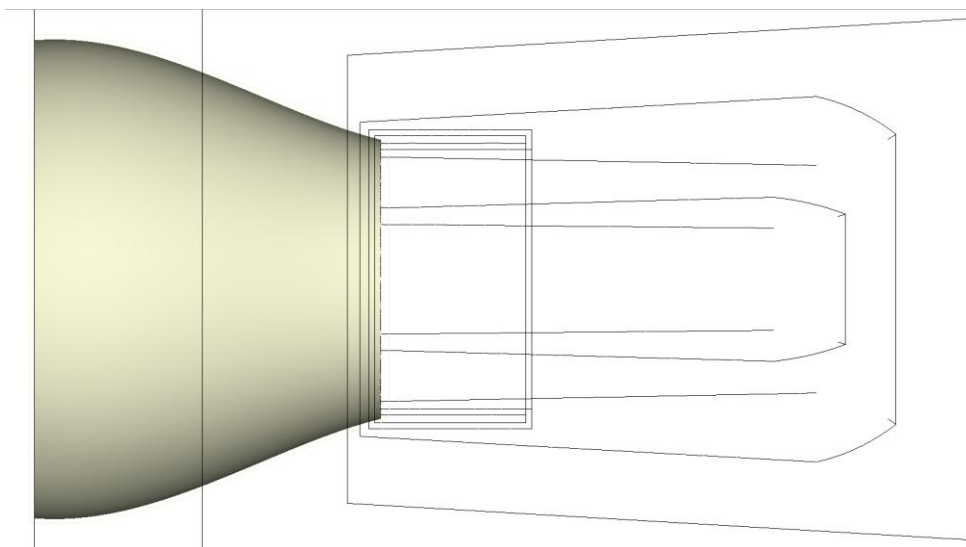
Figure 2.6: A schematic of the VR regions close to the nozzle.
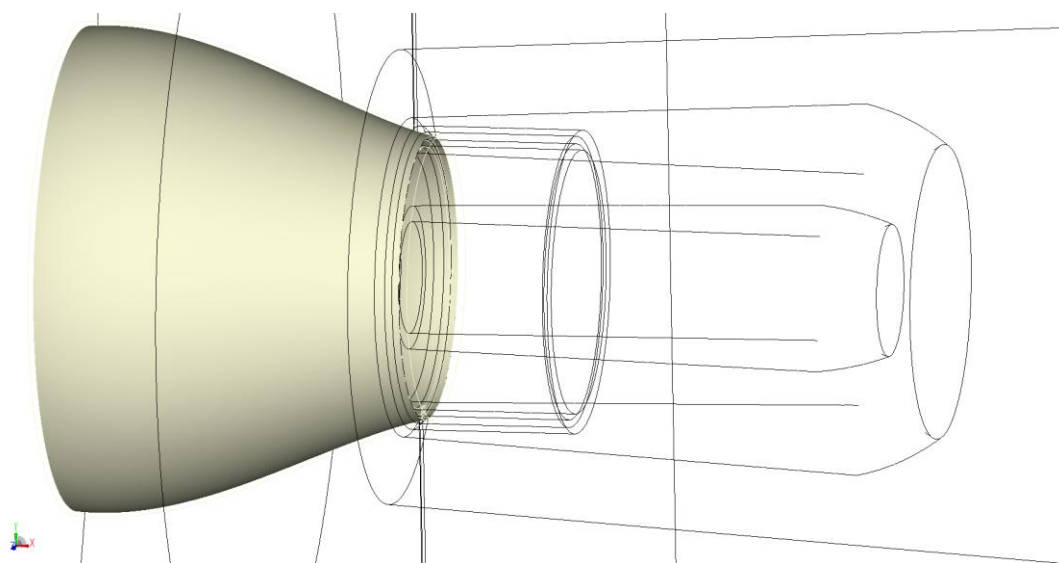
Figure 2.7: An isometric view of the zoom-in VR regions.
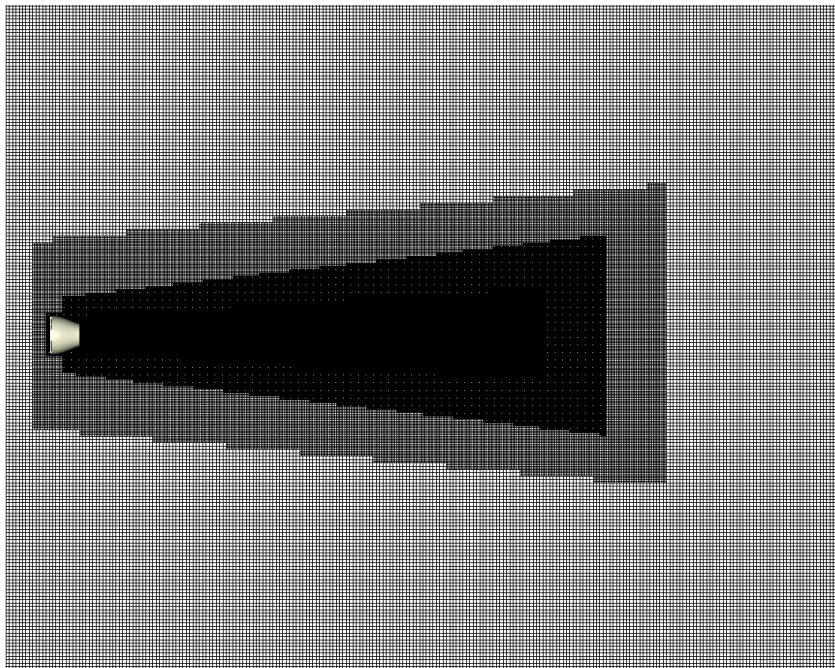
Figure 2.8: Streamwise view of voxel distribution in the entire domain.
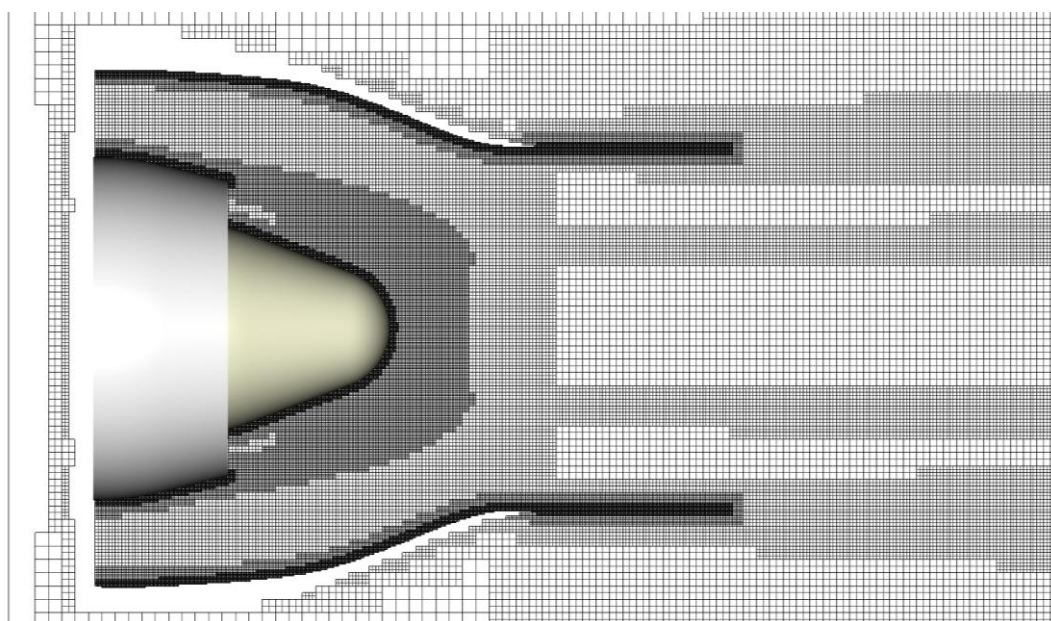
Figure 2.9: Streamwise view of voxel distribution inside the nozzle.
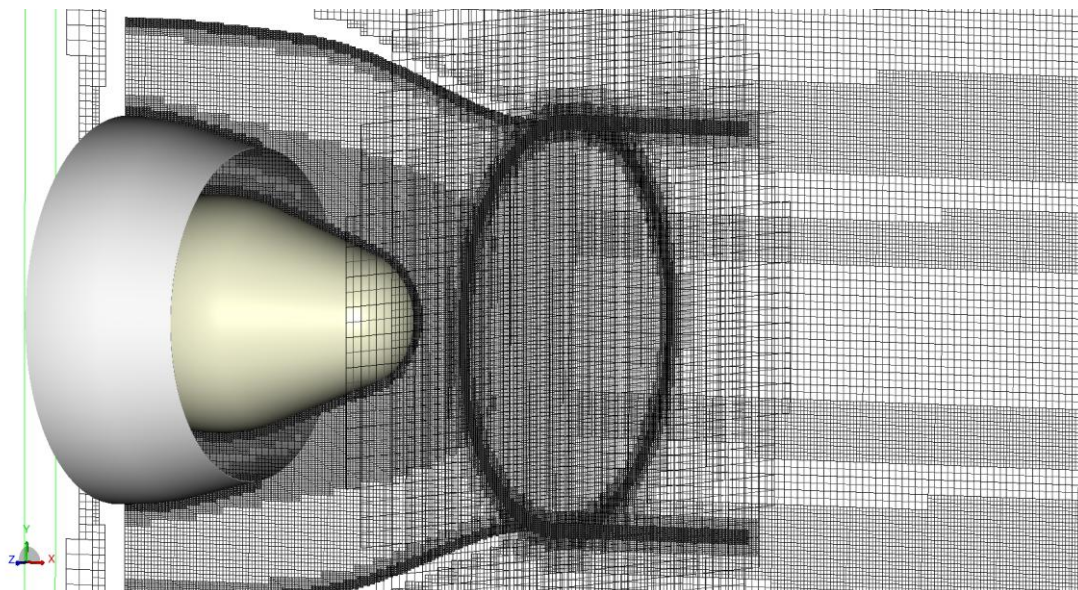
Figure 2.10: An isometric view of voxel distribution near the nozzle.
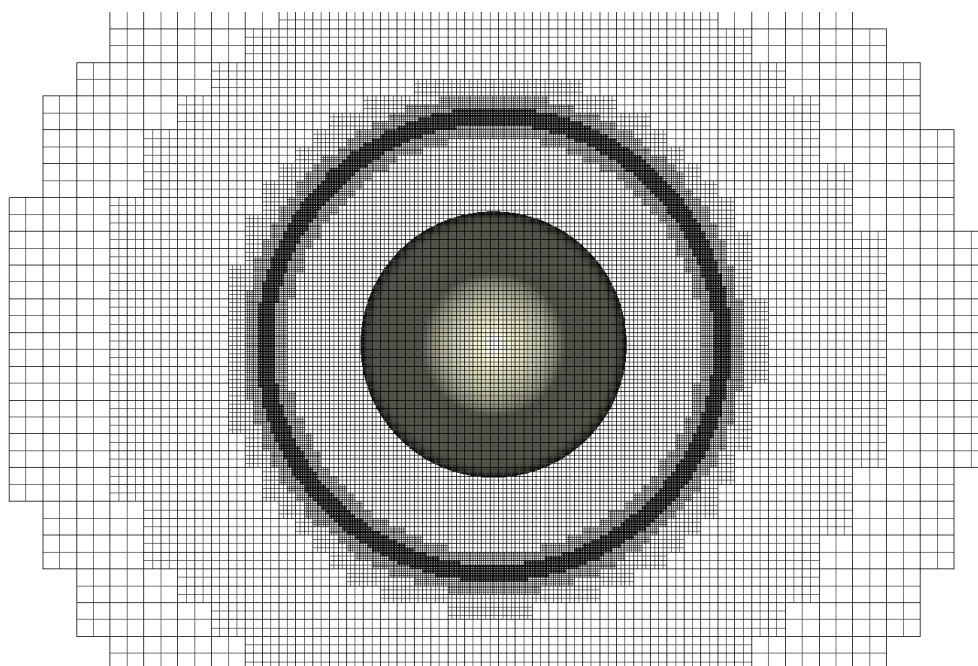
Figure 2.11: Voxel distribution at the nozzle exit.
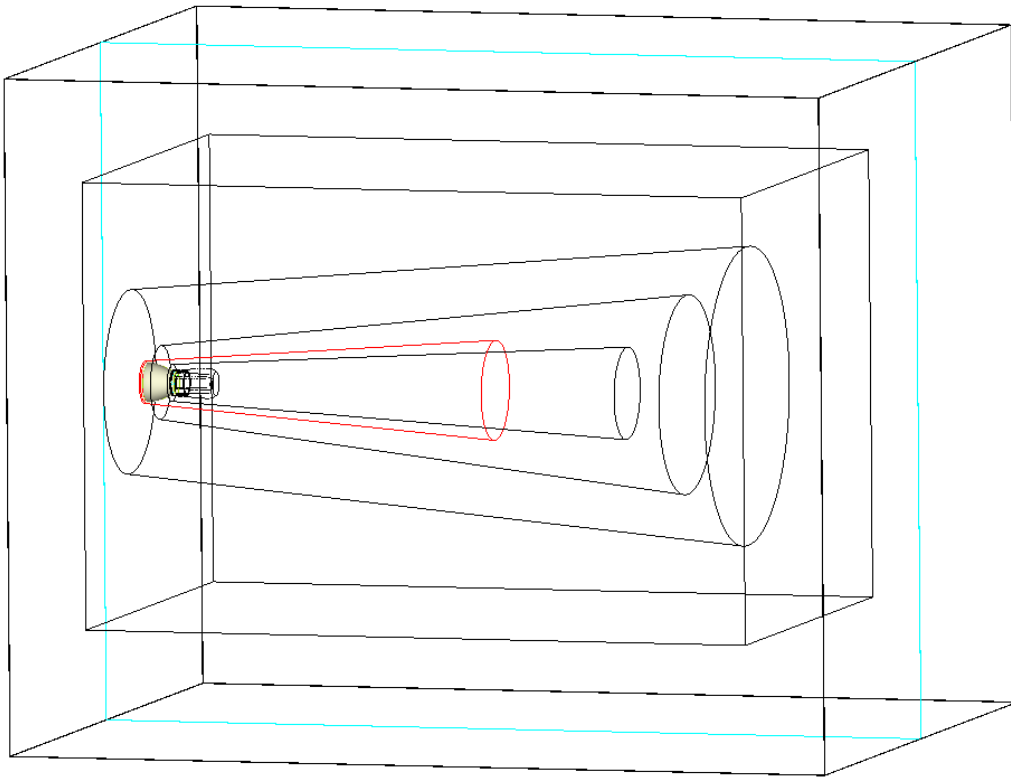
Figure 2.12: Streamwise measurement window and 3D measurement window. Blue square box: Streamwise measurement window; red cylinder: 3D measurement window.
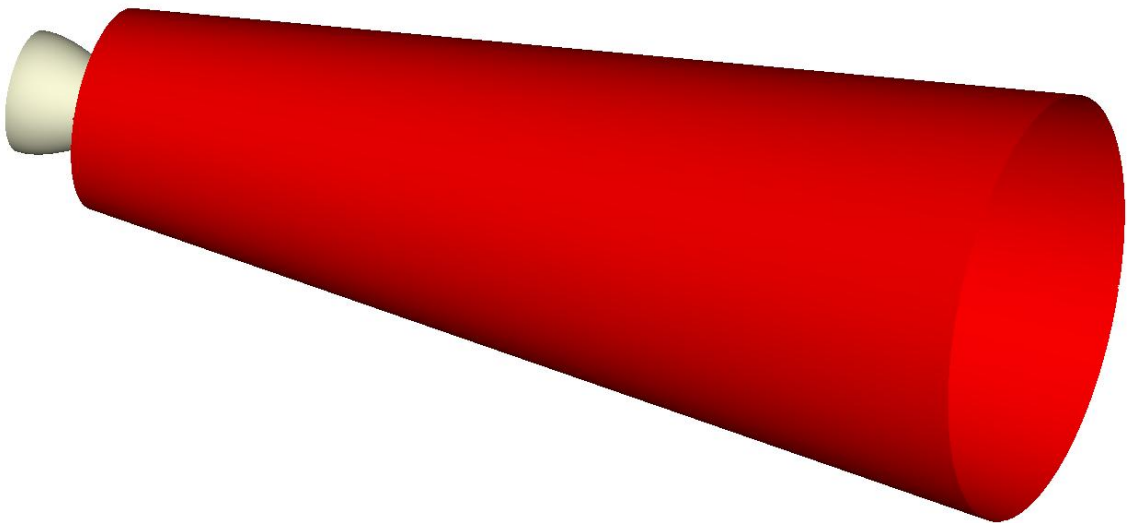
Figure 2.13: Porous FWH control surface.
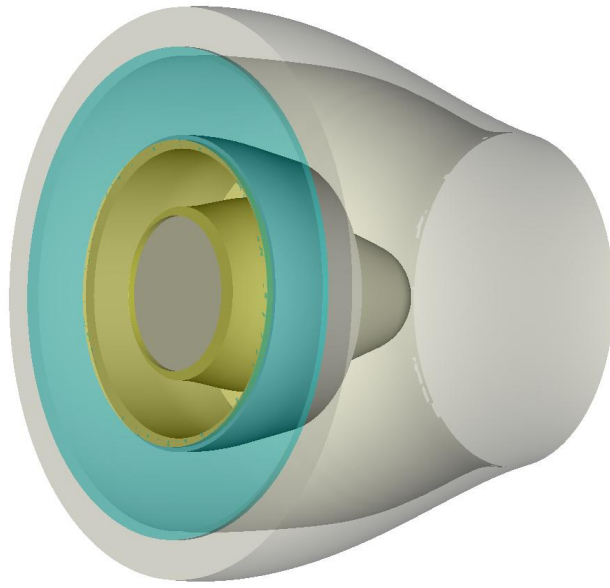
Figure 2.14: Inlet geometries. Blue plate: fan stream inlet; yellow plate: core stream inlet.
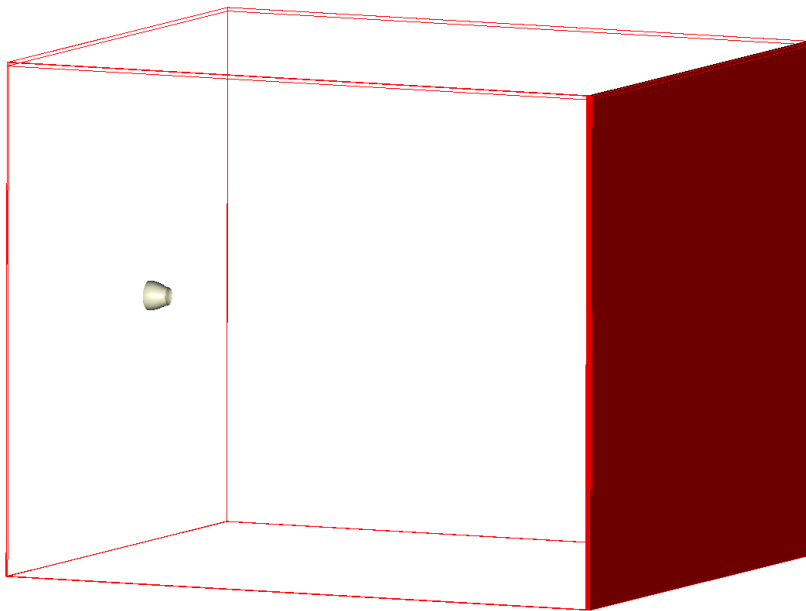
Figure 2.15: Outlet boundary geometry. Red solid plate: outlet.
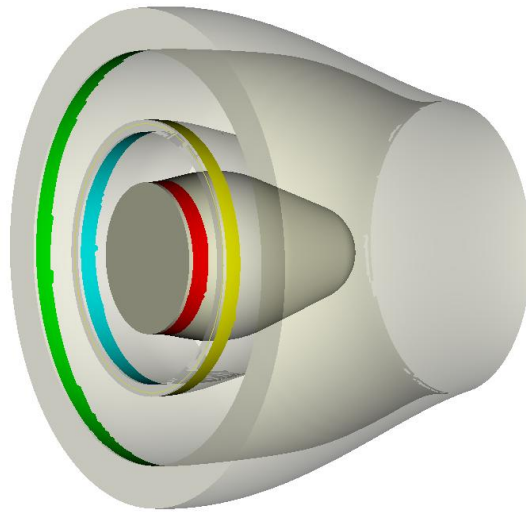
Figure 2.16: Inlet surfaces of the artificial forcing.

Chapter 3 Effects of Lobe Number and Penetration Depth

The aerodynamic performance and noise emissions of three unscalloped mixers (i.e., CONF, 12CL, 20UH) were investigated. With the confluent mixer as a baseline, the 12CL and 20UH configurations were selected to study the compounded effects of lobe number and penetration depth. Although the consequences of changes in these two geometrical parameters are not independent, the effects of increased interface area between core and fan streams were studied. Instantaneous and time-averaged flow results and statistics were obtained. Plume survey data revealed the local velocity distribution across transverse cross-sections of the jet at different downstream locations to help relate the plume flow physics and the radiated sound. Overall sound pressure levels (OASPL) and sound pressure level (SPL) directivity results were obtained for the three mixers. The results qualitatively matched previous experimental findings.

3.1 Aerodynamic Results and Analysis

The same operating conditions (i.e., velocity and static pressure) were imposed in the simulation for the three mixer-nozzle configurations. Because the three models also had the same fan inlet and core inlet area, the bypass ratios (BPR, defined as m_f /m_c) were identical. Figure 3.1 shows a snapshot of the transient streamwise velocity iso-surface (U_x=80 m/s) qualitatively representing the diffusion of momentum in the quiescent fluid medium interacting with the jet shear layer. Figure 3.2 (a) to (c) shows the instantaneous total velocity contours of the three mixers. These are within planes along the jet centerline, through the lobe crests of 12CL and 20UH. The 12CL mixer had the highest jet exit velocity (i.e., time- and space-averaged velocity magnitude at the nozzle exit) of 149.65 m/s (Mach 0.43), while the 20UH mixer had the lowest jet

velocity of 142.30 m/s (Mach 0.41). It can be observed from Figures 3.1 and 3.2 that the flow field reached a fully turbulent state within one jet diameter downstream of the nozzle exit. The turbulent jet cores broke approximately eight jet diameters downstream of the exit.

Figure 3.3 (a) to (c) shows close-up views of instantaneous vorticity inside the three nozzles. It can be seen from Figure 3.3 (a) that there was hardly any mixing between core and fan streams downstream of the confluent mixer. The only turbulent vortex shedding pattern observed was immediately downstream of the center body due to flow separation. For the two lobed mixers, Figures 3.3 (b) and (c) show clearly the mixing phenomenon inside the nozzle. For both the 12CL and the 20UH mixers, flow separation occurred near the upper wall of the lobe. The vortex shedding process occurred immediately downstream to the 20UH mixer exit. For the 12CL mixer, there was no vortex observed until around one lobe height downstream of the mixer exit. Due to a greater lobe number, the 20UH mixer had smaller lobe widths which were the characteristic length for the vortex produced by the mixer. Figures 3.3 (b) and (c) confirm that the 20UH mixer had a much smaller vortex length scale compared to the 12CL mixer. Figures 3.3 (b) and (c) show that the vortex shedding location of 20UH was much closer to the nozzle wall, and the vortex detached from the 20UH mixer entered the shear layer downstream of the nozzle exit plane. This can be explained by the high penetration depth of the 20UH mixer. It can be inferred that increased turbulent intensity added into the shear layer might increase the far-field noise level. However, as discussed in section 3.2, it was observed that this penalty is not significant in comparison with noise reduction benefits of the 20UH mixer.

Figure 3.4 (a) to (c) shows the lambda 2 criterion iso-surface for the three mixers (iso-surface value = -100). Lambda 2 was defined as the second eigenvalue of the symmetric tensor $S^2 + \Omega^2$, where S and Ω were respectively the symmetric and anti-symmetric parts of the velocity gradient tensor ∇u. This criterion has been shown to accurately capture vortex structure[79] and to properly visualize the 3D turbulent coherent structures. The 12CL and 20UH mixer featured intensive mixing processes,

while the confluent mixer did not produce any significant mixing pattern.

Figures 3.5 (a) to (c) show the mean streamwise velocity contour at the nozzle exit plane. In terms of magnitude, the 12CL mixer had the highest average and peak velocities, and the 20UH had the lowest. The confluent mixer had a contour similar to that of the simple dual stream coaxial jet. The circular ring region of low velocity magnitude indicated the mixing area where interaction between the two streams occurred due to Kelvin-Helmholtz instability. The energy loss caused by flow separation behind the center body led to the velocity deficit visible in the center region of the contour. As seen from Figures 3.5 (b) and (c), there are clear indications of the 12CL and 20UH lobe shapes at the exit of the nozzle. The lobed mixers considerably reduced the velocity within the core region associated with the confluent mixer. The greater lobe number and deeper penetration caused the 20UH mixer to exhibit a relatively more uniform flow profile than that of the 12CL.In comparison with the 12CL mixer, the wetted area of the high velocity region for the 20UH mixer was smaller and closer to the nozzle wall due to the high penetration length. Because a more uniform flow velocity profile at the nozzle exit should lead to reduced noise levels, the OASPL level for the 20UH was expected to be lower than that for 12CL.

Figure 3.6 (a) to (c) shows the time-averaged mean streamwise velocity contour for the three cases along the jet center plane. Identical to the previous results, for all three cases, a velocity deficit region extended from the end of the center body to approximately two diameters downstream of the nozzle exit plane. The confluent mixer did not show any evidence of significant mixing, and there were velocity peaks close to the nozzle lip. The 12CL mixer produced a high velocity region close to the nozzle lip line, which extended from slightly upstream of the nozzle exit to about 1.5 jet diameters downstream of the exit. In contrast to the confluent mixer, the 20UH had a fairly well mixed flow profile, with high velocity regions confined within the nozzle. The three mixers produced about the same potential jet core length.

The corrugated azimuthal flow profiles in the lobed mixer cases became smooth and axisymmetric downstream of the nozzle exit due to the good azimuthal mixing

produced by the axial vortices. Hence, a center line velocity decay comparison should give a fairly good indication of the overall relative noise levels produced by the lobed mixer. The centerline mean streamwise velocity comparison is shown in Figure 3.7. The velocities were normalized by the jet velocity, and the measurement started from the nozzle exit plane. Within the first jet diameter, there were initial increases for all three cases due to the velocity deficit. From approximately two to six diameters downstream of the exit, the velocities remained nearly constant, except that inside the confluent mixer-nozzle the velocity continued to rise gently. Note that the peak velocity of the confluent mixer was about 10% U_j higher than the 12CL. The next section looks at whether this would affect the far-field noise level. Further downstream, the three cases yielded a similar decay rate for the centerline velocity.

Figure 3.8 (a) to (c) shows the mean turbulent kinetic energy contour for the three cases. The low energy near the nozzle lip indicates a nearly laminar exit shear layer. Interestingly the flow reached a fully turbulent state, or its peak turbulent kinetic energy level, at different downstream locations for the three mixers. The peak turbulent kinetic energy level was reached at around $0.6D_j$, $0.5D_j$, and $0.4D_j$ downstream of nozzle exit plane for the confluent, 12CL, and 20UH mixers respectively. Lobed mixers are expected to produce higher turbulent energy levels than the confluent mixer in the shear layer because of enhanced mixing. The 20UH mixer had turbulent kinetic energy concentrations closer to the nozzle than did the 12CL. The addition of streamwise vorticity into the nozzle exit shear layer clearly increased mixing, causing the turbulent kinetic energy to peak further upstream.

Figure 3.9 shows non-dimensional centerline mean turbulent kinetic energies as a functions of streamwise distance. It can be observed that the 12CL and 20UH mixers reached a peak level further upstream than the confluent mixer. Comparing the two lobed mixers, it appeared that the 12CL reached the highest turbulent kinetic energy level earlier than the 20UH. This might be because the high penetration of the 20UH mixer tended to guide the energy-containing vortices towards the nozzle wall and away from the nozzle centerline. In terms of magnitude, the value of the confluent

mixer was 0.3% higher than that of the 20UH, and 0.5% higher than that of the 12CL. Further downstream, the turbulent kinetic energy of the 12CL and 20UH mixers decayed at about the same rate, slightly faster than that of the confluent mixer.

Figure 3.10 (a) to (f) shows cross-stream views of mean streamwise velocity contours at different streamwise locations. From Figure 3.10 (a), it can be seen that small-scale vortices started to form at the crest and valley of the lobes of the 12CL and the 20UH mixers. This observation has been reported previously [5,72]. The velocity magnitude of the fan and core streams was similar for the 12CL and 20UH mixers, whereas the two streams surrounding the confluent mixer did not show any sign of mixing. Viscous mixing in the confluent mixer, the dominant mechanism available, was obviously not effective. The Kelvin-Helmholtz instability was apparently not a strong mixing mechanism for the confluent mixer with a fan-to-core velocity ratio of 1.24. From Figure 3.10 (b), at the nozzle exit, clear 'footprints' of the lobe shape can be detected for the 12CL and 20UH mixers. One can qualitatively say the 20UH mixer was better mixed than the 12CL. The greater penetration and lobe number of the 20UH mixer increased the interface area between the two streams. Previous experimental results have indicated that this effect is conducive to faster mixing[3]. The enhanced mixing mechanism was largely attributed to the streamwise vorticity generated by the difference in radial velocity components of the core and fan flows near each lobe sidewall. The axial vorticity generated downstream of the lobe sidewalls rotated the two flows around each other in tight spirals, increasing the interface area, producing better mixing. The effect of lobe penetration on the radial location of the vortices at the nozzle exit plane was also clearly captured. The 12CL mixer, with low penetration, had its axial vortices closer to the central axis than 20UH. Because the nozzle exit radius is smaller than the radial height of the lobe crests in 20UH, it appeared that these axial vortices could be interacting with the nozzle wall at the very aft end. This was confirmed by results from Figure 3.3 (c). Figure (c) to (f) shows that after one jet diameter, the lobed pattern started to become diffuse, and then became axisymmetric further downstream.

Figure 3.11 (a) to (c) shows a plume survey of mean streamwise velocity across transverse cross-sections of the jet at different downstream locations. For all cases, the initial complicated structure of the velocity profiles gave way to a simpler plume further downstream. The velocity magnitude continued to increase beyond the exit until one diameter downstream. High-velocity gradients were observed at the nozzle lip shear layer. For the confluent mixer, in the region within one diameter from the exit plane, high-velocity gradients were observed at the radial locations where the two streams interacted. The velocity deficit also caused high-velocity gradients in the vicinity of the centerline. As for the 12CL mixer, within one diameter downstream of the exit, there were high-velocity gradients concentrated close to the inner side of the nozzle lip line. The velocity deficit effect was decreased due to mixing. It is interesting to see that for the 20UH mixer the large velocity gradient near the inner surface of the nozzle lip line was diffused almost immediately downstream of the nozzle exit, and the velocity profile varied gently further downstream. This should be attributed to the high penetration depth and enhanced mixing process of the 20UH mixer. The radial gradients in axial velocity govern part of the turbulence intensity and are strong sources of noise. The plume generates noise not only from the radial gradient in velocity at the nozzle-lip shear layer, but also from axial vortex structures and velocity peaks. These are excess noise sources, in the sense that they do not occur in a jet with equivalent uniform velocity at the nozzle exit plane. In the next section, the impact of velocity gradients on the far-field noise was examined.

The mean thrust coefficients of the three cases were compared and listed in Table 3.1. The coefficient was calculated as follows:

$$C_T = \frac{F}{\frac{1}{2}\rho u^2 A},$$
(3.1)

where

$$F = \iint \rho V (V \cdot n) dA + A_j (P_j - P_a).$$
(3.2)

The results showed that the geometric difference of the different lobed mixers didn't have a significant impact on the produced mean thrust coefficient.

3.2 Acoustic Results and Analysis

Figures 3.12 to 3.15 show the OASPL directivity and the associated SPL directivity comparison for the confluent, 12CL, and 20UH mixers. Recall that the results were obtained for a stationary mean flow with no forward flight effects. The virtual microphones were located on a circle with a radius of 45m ($21D_j$), covering the angles from 45 to 160 degree relative to the nozzle inlet axis.

The OASPL level of the confluent mixer was the highest, as expected. Compared to the confluent mixer, 12CL had the largest OASPL reduction of 2.7 dB at a 45-degree angle and around 2 dB reduction at aft angles. The 20UH OASPL directivity followed a trend similar to that of the 12CL mixer, but it had the lowest OASPL level at all angles. The two lobed mixers both reached a peak level at around 140-degree angle, which is consistent with experimental results[72]. The OASPL directivity of the confluent mixer reached a peak value at 145 degrees, and remained constant in locations further downstream. The OASPL result further confirmed experiment results[72,73] that the two tested lobed mixers yielded a significant noise reduction benefit over the confluent mixer. It also indicated that the increased interface area offered by the 20UH mixer produced additional OASPL reductions compared to the 12CL mixer.

From Figure 3.13, band-passed SPL directivity at 120 hz, it can be observed that the confluent mixer was 4 dB higher than the 20UH mixer at most angular locations and about 5 dB higher than the 12CL mixer at a shallow angle of 160 degrees. All three mixers reached a peak level at a 160-degree angle. This can be explained by the fact that the jet plume usually decays far downstream of the nozzle exit, and large eddies there govern the low frequency domain. This trend was also consistent with previous experimental results[72]. Lobed mixers were expected to do fairly well in suppressing low frequency noise. The introduction of the lobed mixer was intended to

break the large vortices into smaller eddies to reduce the dominant low frequency noise of the confluent mixer. The 20UH mixer yielded a lower low frequency SPL level than 12CL at most of the angles. As explained earlier, the lobe width (i.e., the characteristic length of the vortex produced by the mixer) of 20UH was smaller than that of 12CL. It seems plausible to relate this fact to the noise suppression at low frequencies.

Figure 3.14 shows the 1200 hz SPL directivity for the three mixers. The confluent mixer was not the noisiest mixer in the mid-frequency domain, as found in previous experiments[72,73]. Instead, the 12CL mixer yielded the highest levels at most observer angles. At locations downstream of 140 degrees, both of the lobed mixers yielded higher SPL levels than the confluent, as expected. The peak of the lobed mixers' SPL level appeared to be shifted with the variation of lobe number and penetration depth. The 12CL and 20UH mixer had a 3 dB difference in terms of SPL peak value. The 20UH mixer remained quieter than 12CL; however, the advantage of 20UH over 12CL in suppressing mid-frequency noise was not as significant as in the low frequency domain. The results indicate that the dominant contribution to the overall mid-frequency noise of lobed mixers was from the downstream angles between 135 and 150 degrees.

The SPL directivity comparison at 4500 hz is shown in Figure 3.15. Except at locations of 85 to 125 degree angles, the high frequency SPL level for the confluent mixer was mostly lower than for the 12CL and 20UH mixers. At positions downstream of the 140-degree angles, the 12CL mixer was quieter than 20UH, and a reduction of 4 dB at a 160-degree angle was obtained. The overall high frequency SPL trends of 12CL and 20UH were similar, and the magnitude was comparable. The 20UH mixer did not seem to produce a significant increase in the high frequency range while suppressing low-to-mid frequency noise. Note that the peak SPL value for 12CL and 20UH was reached at 125- and 135-degree angles respectively. In comparison with the SPL trends over the mid-frequency range, the peak angles were reached further upstream because high frequency noise is usually attributable to

smaller eddies which predominate near the nozzle exit plane or even inside the nozzle, according to turbulent jet theory[80]. High frequency noise is more likely to concentrate at upstream locations[81].

Considering the overall trends for the three mixers, the large reduction in low-frequency noise was found to lead to a lower OASPL level for the two lobed mixers. In the mid-to-high frequency domain, the confluent mixer was mostly quieter than 12CL and 20UH. The 12CL mixer had higher low-to-mid frequency noise and lower high frequency SPL level in the far downstream than 20UH. The high penetration depth and greater lobe number of 20UH brought the extra benefit of decreasing mid-frequency noise while maintaining considerable reduction in low-frequency noise.

3.3 Summary

Inside the 20UH mixer-nozzle were small-scale vortices shed from the mixer tip which entered the downstream nozzle lip shear layer. This effect, however, did not increase the turbulent kinetic energy significantly. The data showed that the peak value of turbulent kinetic energy along the nozzle lip-line was lower downstream of the 20UH mixer-nozzle than for the 12CL. Figure 3.15 shows that the far-field high-frequency noise level of 20UH remained comparable to that of the 12CL. Although the high penetration tended to guide the vortices towards the nozzle wall and the downstream shear layer, this factor did not seem to increase far-field sound.

The uniformity of the velocity profile at the nozzle exit may be indicative of the differences in the three mixers' OASPL level. The 20UH mixer had the most uniform exit velocity profile, followed by the 12CL and confluent mixer. From Figure 3.12, it was found that 20UH had the lowest OASPL level. The decreased high velocity gradient of 20UH as seen in Figure 3.11 (c) provided a possible explanation for the low high-frequency SPL level of 20UH. The high velocity gradient near the jet center line downstream to the confluent mixer might explain why it had a relatively higher SPL level in the high-frequency domain (see Figure 3.15).

For a simple round jet, a correlation exists between the downstream mean centerline velocity decay rate and the far-field low frequency noise level[72]. A faster decay rate usually results in reduced low frequency noise level. However, from Figures 3.7 and 3.13, it is hard to determine whether there was a direct relation between the two factors for jet flow exited from lobed mixers.

Figure 3.8 (a) to (c) showed that the turbulent kinetic energy of the 20UH mixer peaked downstream those of the 12CL and confluent mixer. Calculations showed, however, that the peak turbulent kinetic energy value along the 20UH nozzle lip line was lower than that of 12CL. On the other hand, the OASPL level in Figure 3.12 shows that 20UH had the lowest OASPL level. Therefore, for lobed mixers, it is plausible that it should be the magnitude of the turbulent kinetic energy inside the nozzle lip shear layer that determined the far-field sound level, rather than the increasing rate of the turbulent kinetic energy.

Finally, the overall effect of increasing lobe number and penetration depth increases the interface area between the fan and the core flows and decreases the length scale of the axial vortices. This should enhance mixing between the two flows. A decrease in the length scale of the axial vortices seems to imply an increase in the dominant frequency, but it is true only if their strengths remained the same. As the lobe number and penetration depth increase, the number of vortices occupying the space within the nozzle must also increase. This promotes upstream azimuthal interaction between the vortices and reduces their strength. It has been shown from Figure 3.14 that the mid-to-high frequency sound of 12CL and 20UH was associated with these axial vortices. In Figure 3.12, the mid-frequency content of the 20UH mixer was less than that of the comparable 12CL mixer. This seemed to imply that an increase in the lobe count produced a reduction in the strength of the axial vortices due to better azimuthal mixing of the axial vortices. On the other hand, the 20-lobe mixer, 20UH, was also effective in reducing the low frequency portion of the spectrum which was typically related with the far downstream plume characteristics. Penetration played a role in the radial migration of the axial vortices generated by the

mixers. This change in radial migration determined whether the vortices would interact with the outer nozzle wall and modify the ambient-jet shear layer. The12CL low-penetration mixer kept the axial vortices closer to the jet centerline. This should, to some extent, prevent the core flow from immediately interacting with the ambient shear layer, and hence reduce the mid-to-high frequency noise from that region. However, these vortices could modify the flow further downstream and change the noise characteristics in a different manner which might be why (shown in Figure 3.15) substantial reduction was not obtained in the high-frequency domain.

Mixer ID	$T_{s,c}/T_{s,f}$	M_j	C_T
Confluent	1.0	0.41	1.95
12CL	1.0	0.42	1.94
20UH	1.0	0.43	1.94

Table 3.1: Mean thrust coefficient comparison between the three tested cases.
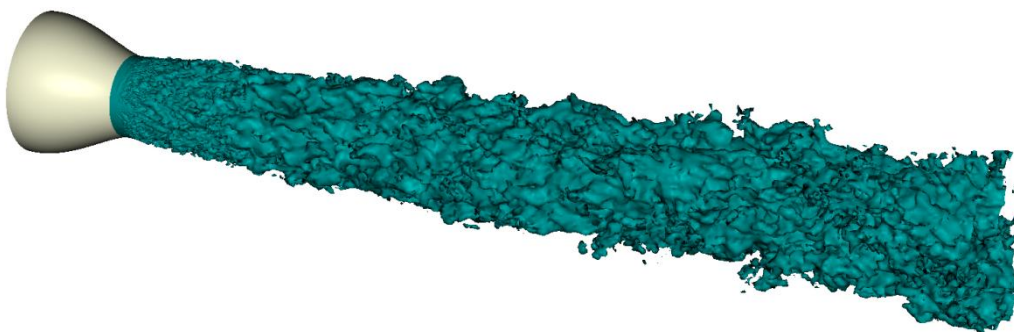
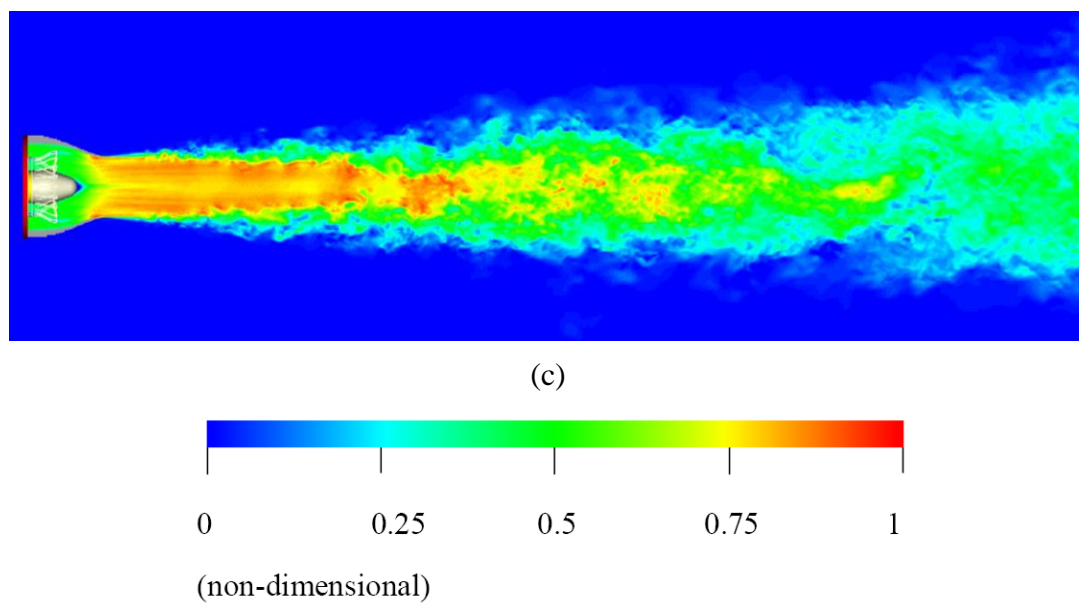Figure 3.1: Transient streamwise velocity iso-surface (U_x=80 m/s).

(a)

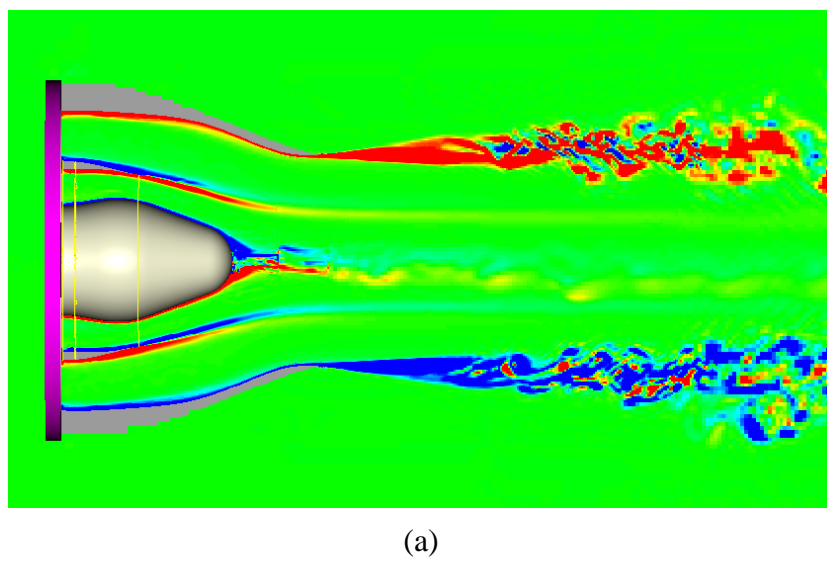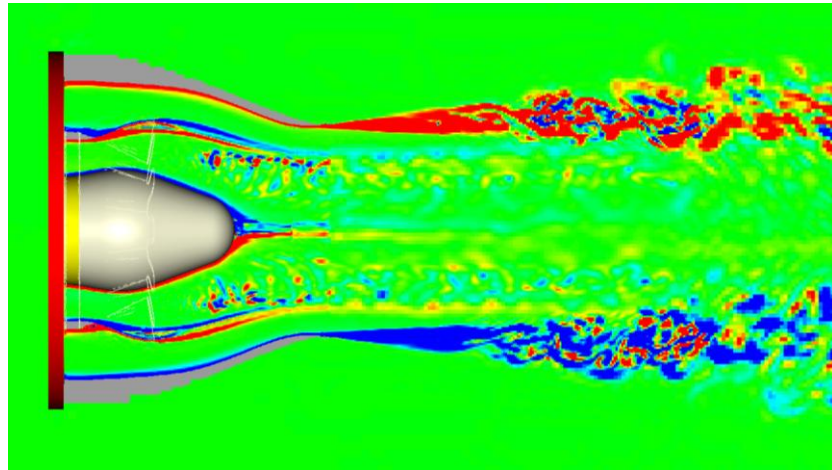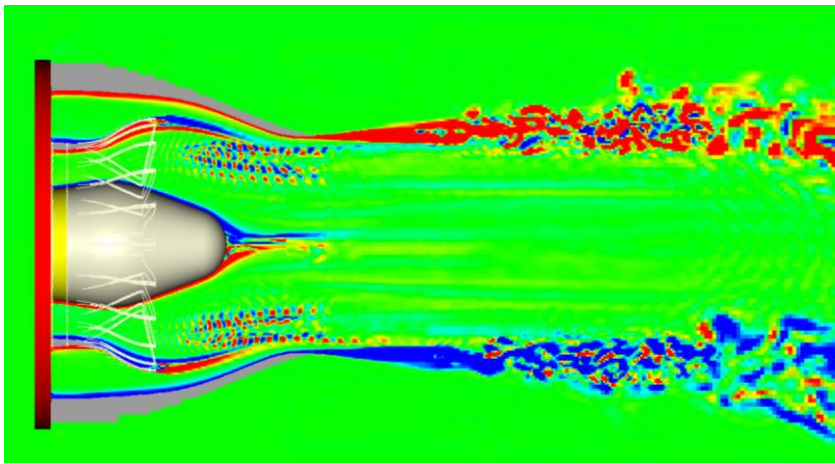
(b)

(c)
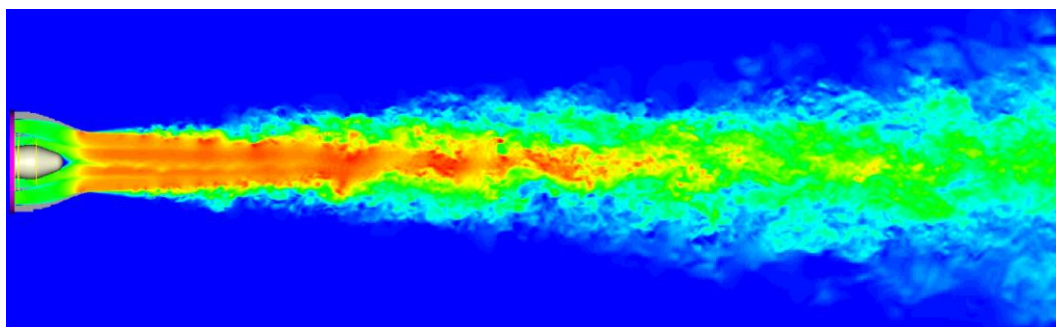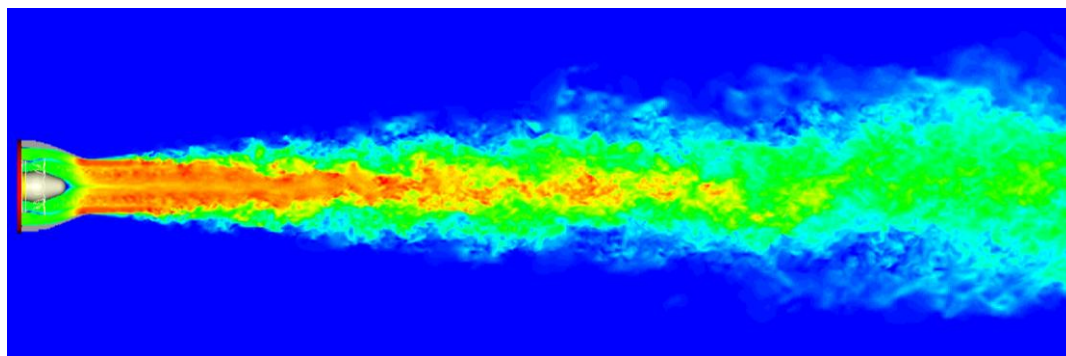
(non-dimensional)

Figure 3.2: Instantaneous total velocity contours of the three mixers. (a): confluent mixer; (b): 12CL; (c): 20UH.
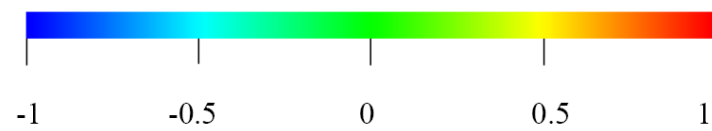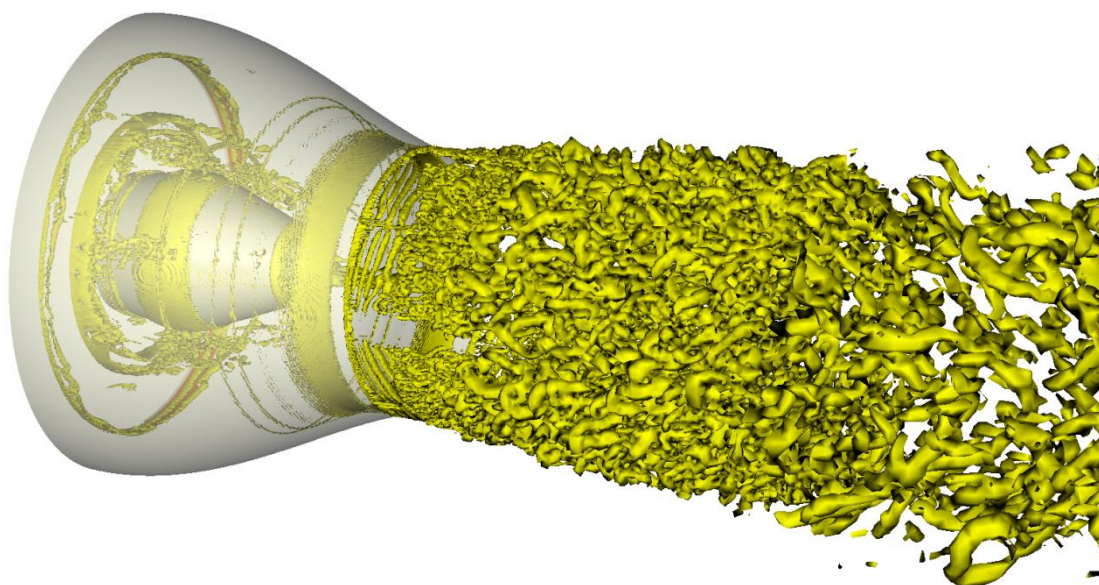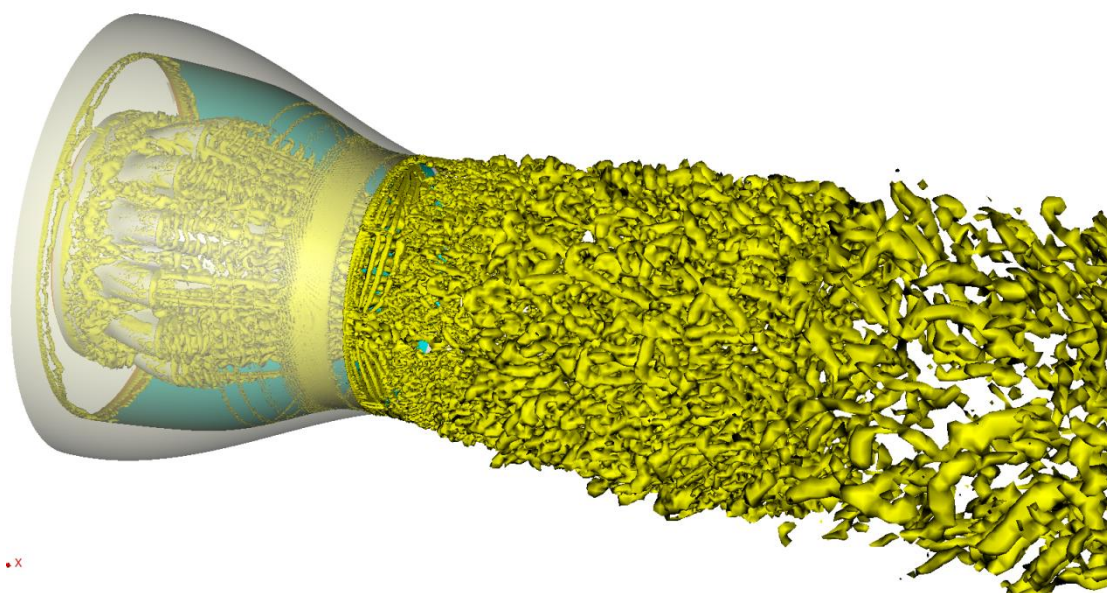

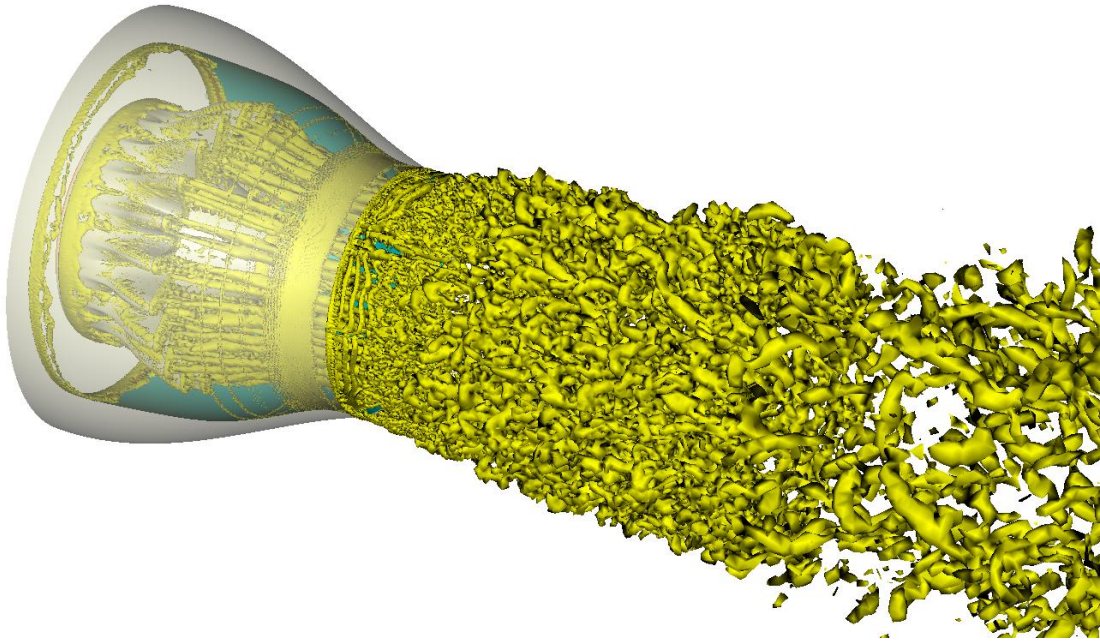
(a)

(b)

(c)

(non-dimensional)

Figure 3.3: Close-up view of instantaneous vorticity inside the three nozzles. (a): confluent mixer; (b): 12CL; (c): 20UH.
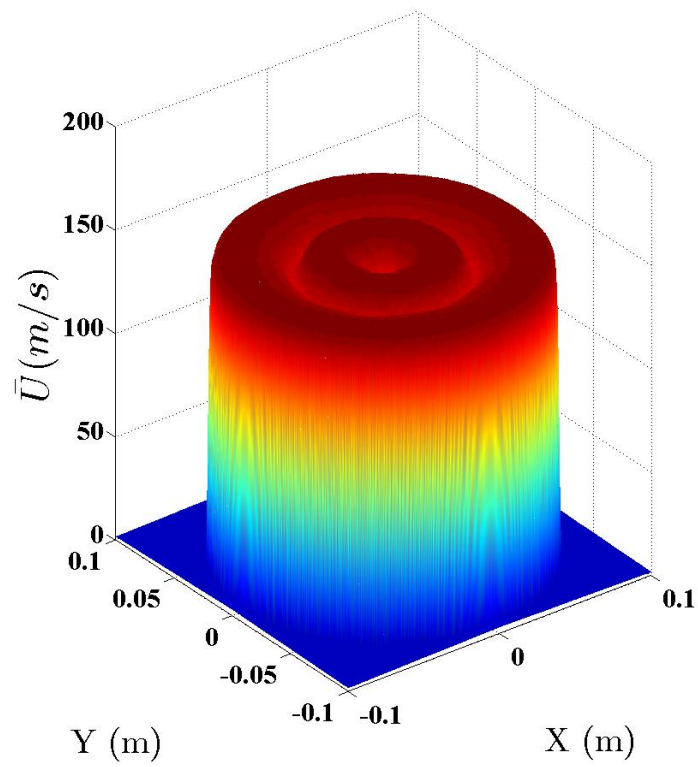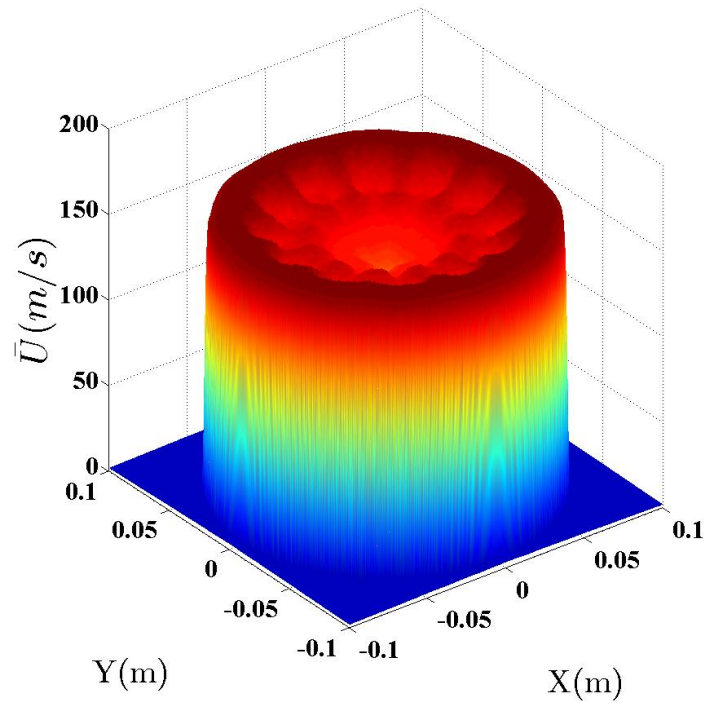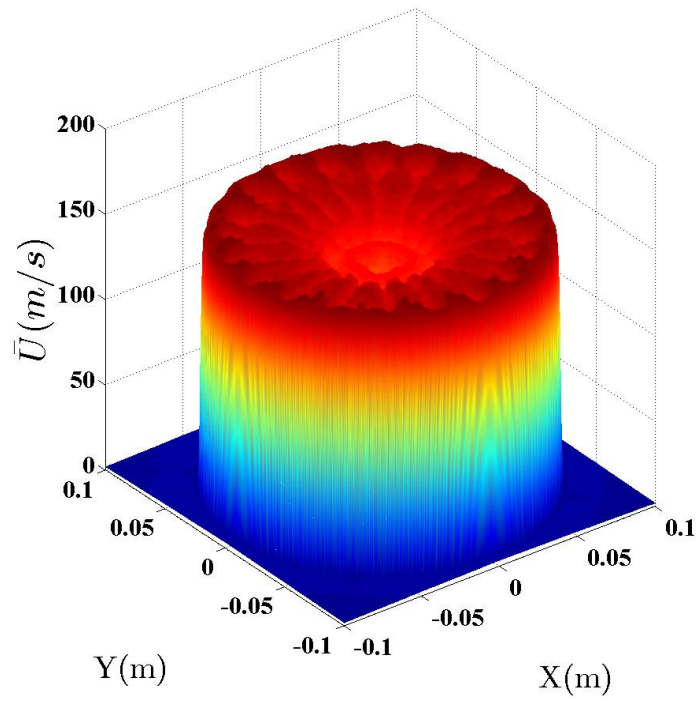
(a)

(b)

(c)

Figure 3.4: Lambda 2 criterion iso-surface for the three mixers. (a): confluent mixer; (b): 12CL; (c): 20UH. (iso-surface value = -100)

(a)

(b)

(c)

Figure 3.5: Mean streamwise velocity 3D contour at the nozzle exit plane. (a): confluent mixer; (b): 12CL; (c): 20UH.

(a)

(b)

(c)

0   0.25   0.5   0.75   1
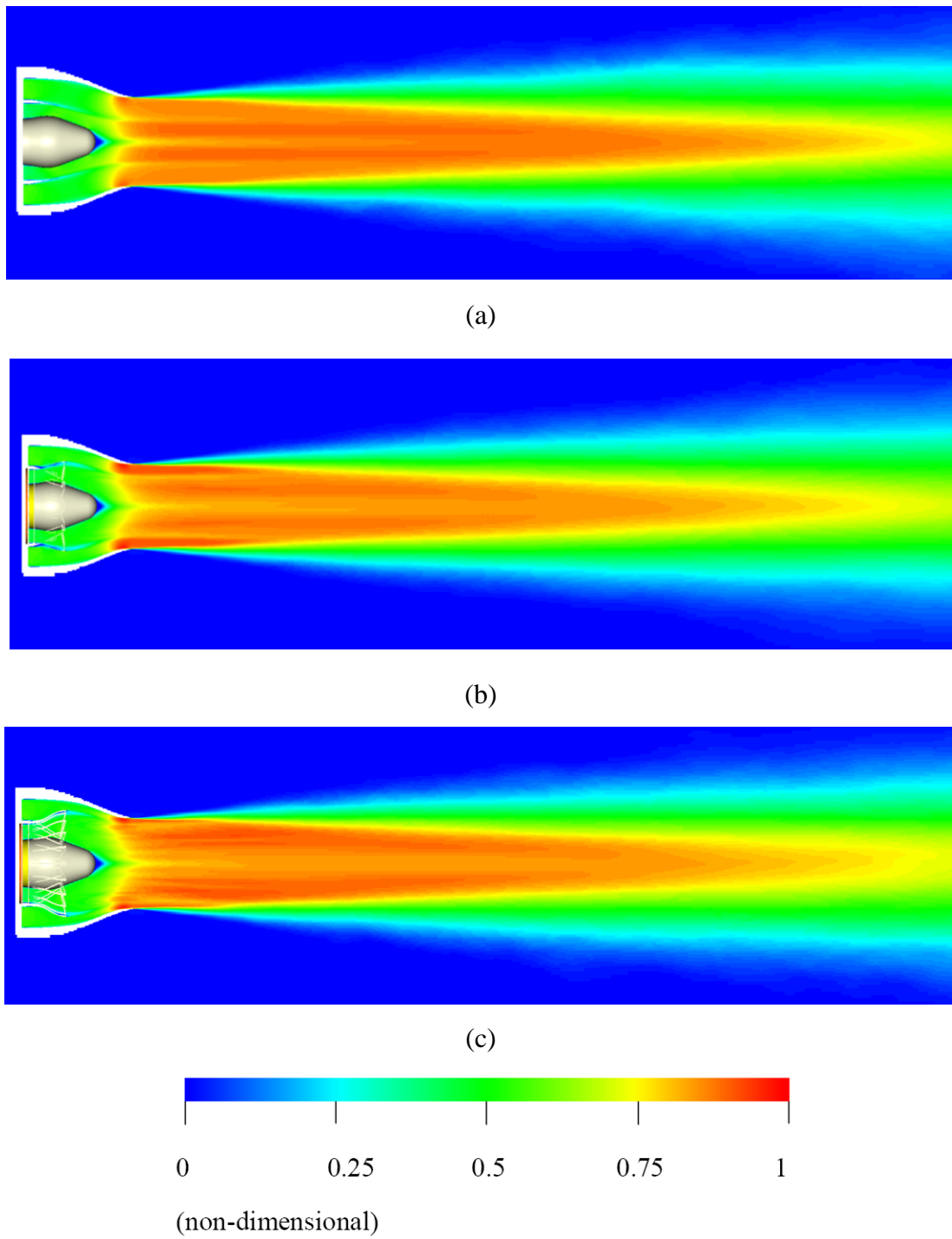
(non-dimensional)

Figure 3.6: Time-averaged mean streamwise velocity contour for the three cases along jet center plane. (a): confluent mixer; (b): 12CL; (c): 20UH.

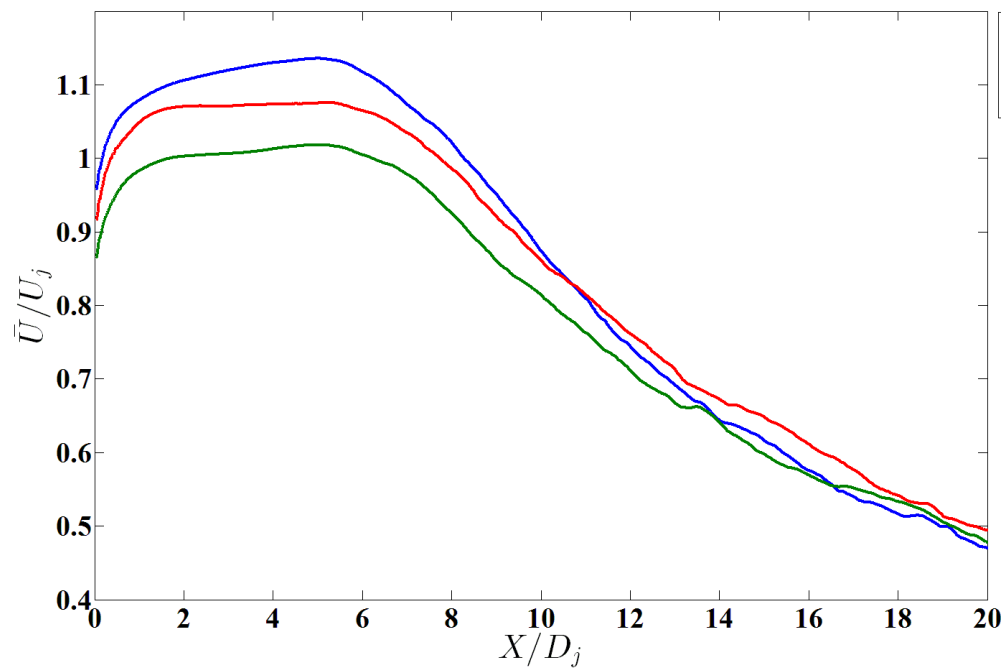Figure 3.7: Center-line mean streamwise velocity. Blue line: confluent mixer; green line: 12CL; red line: 20UH.

(a)

(b)

(c)
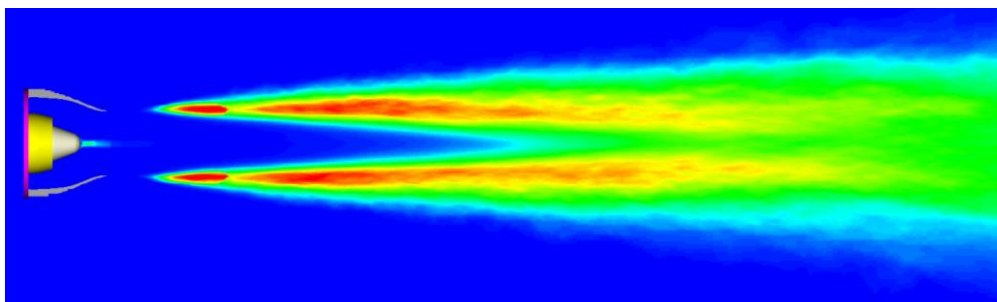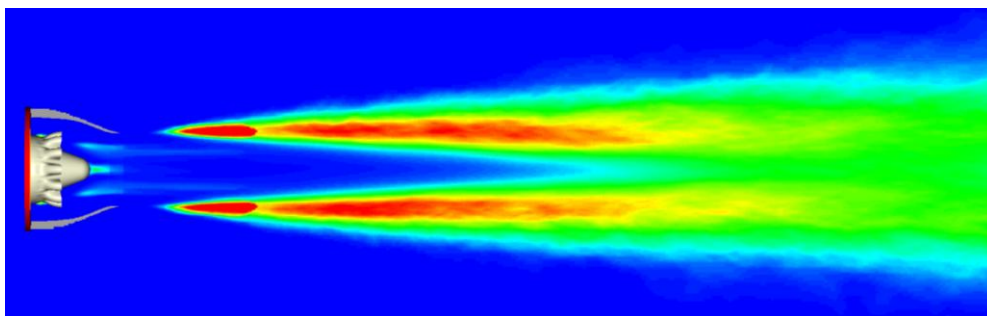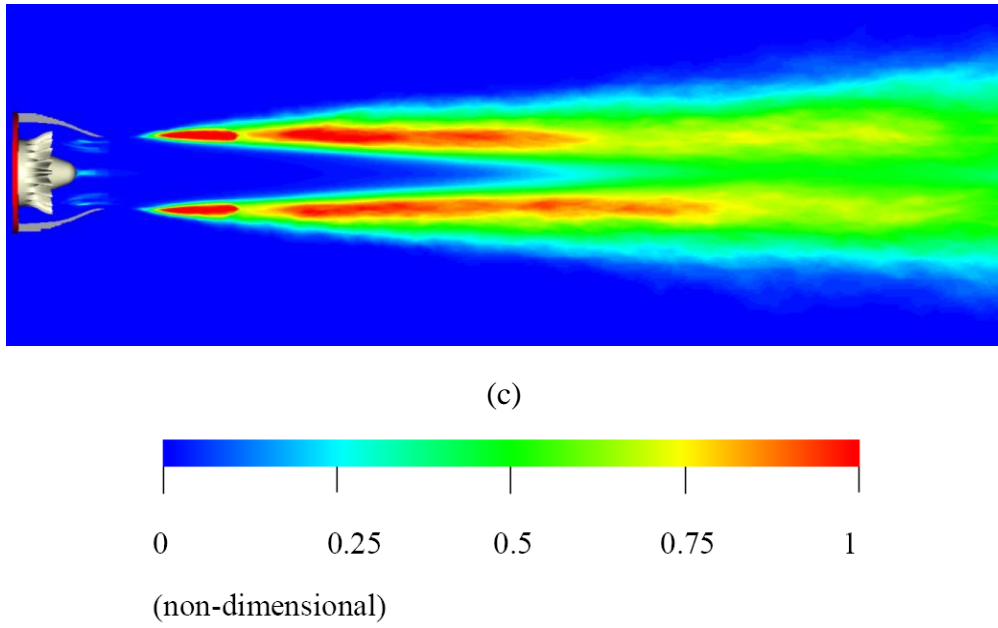
(non-dimensional)

Figure 3.8: Time-averaged mean turbulent kinetic energy contour. (a): confluent mixer; (b): 12CL; (c): 20UH.
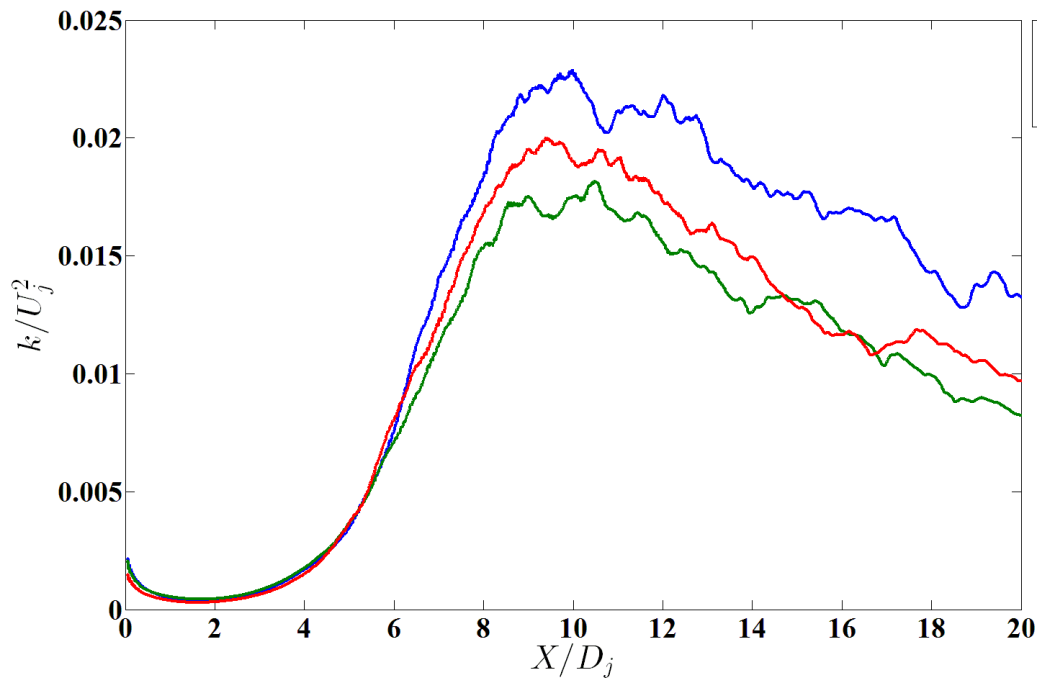
Figure 3.9: Non-dimensional center-line mean turbulent kinetic energy. Blue line: confluent mixer; green line: 12CL; red line: 20UH.
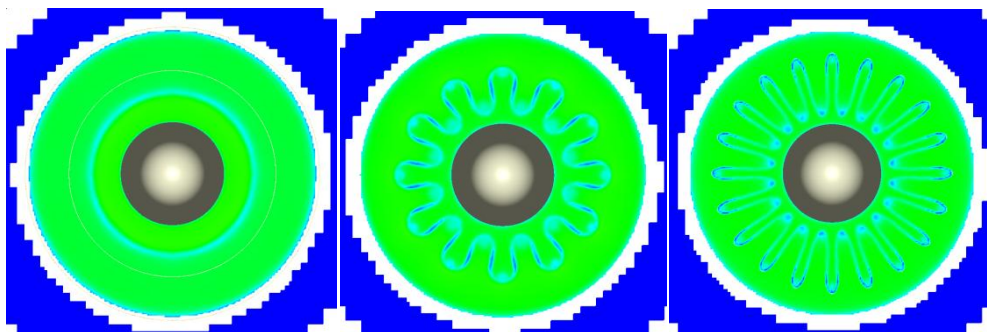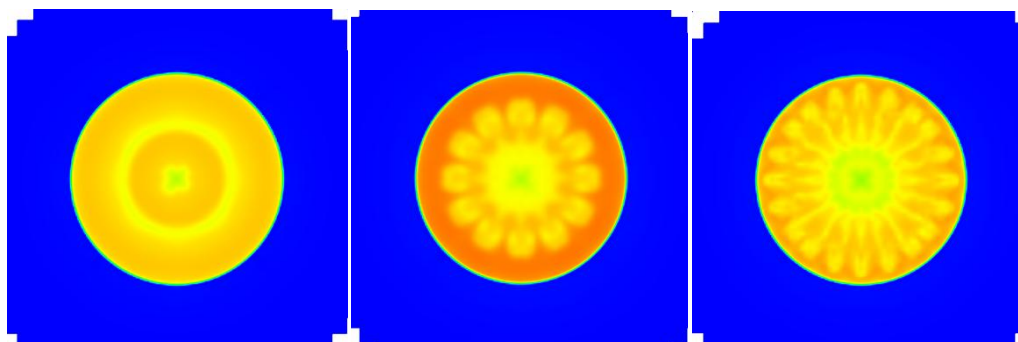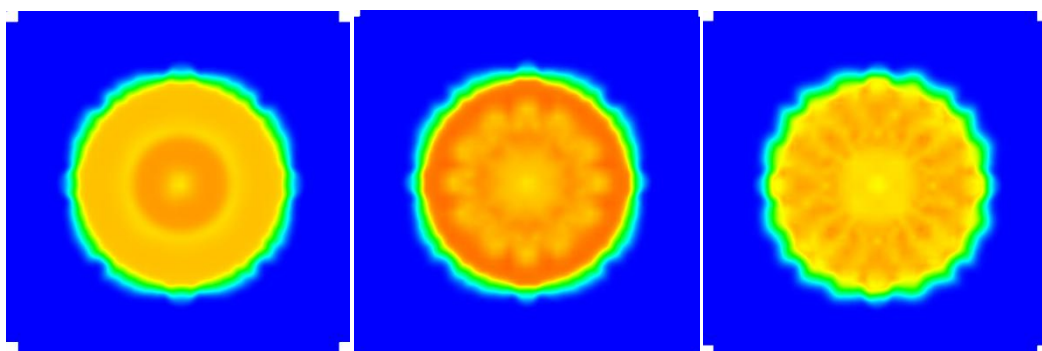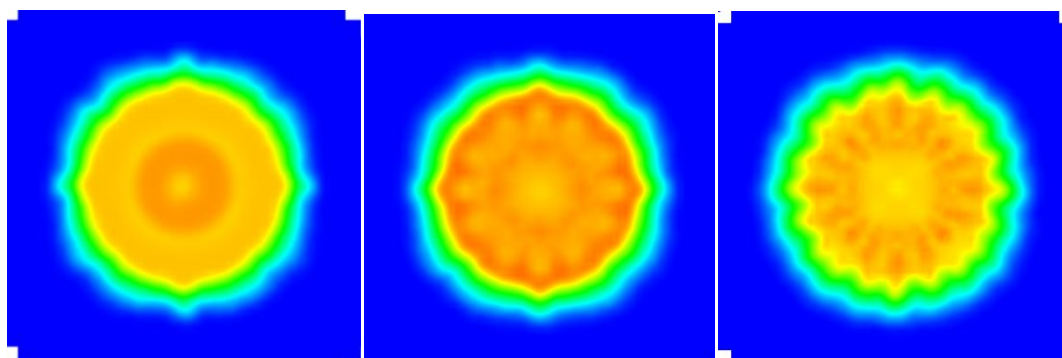
(a)

(b)

(c)

(d)
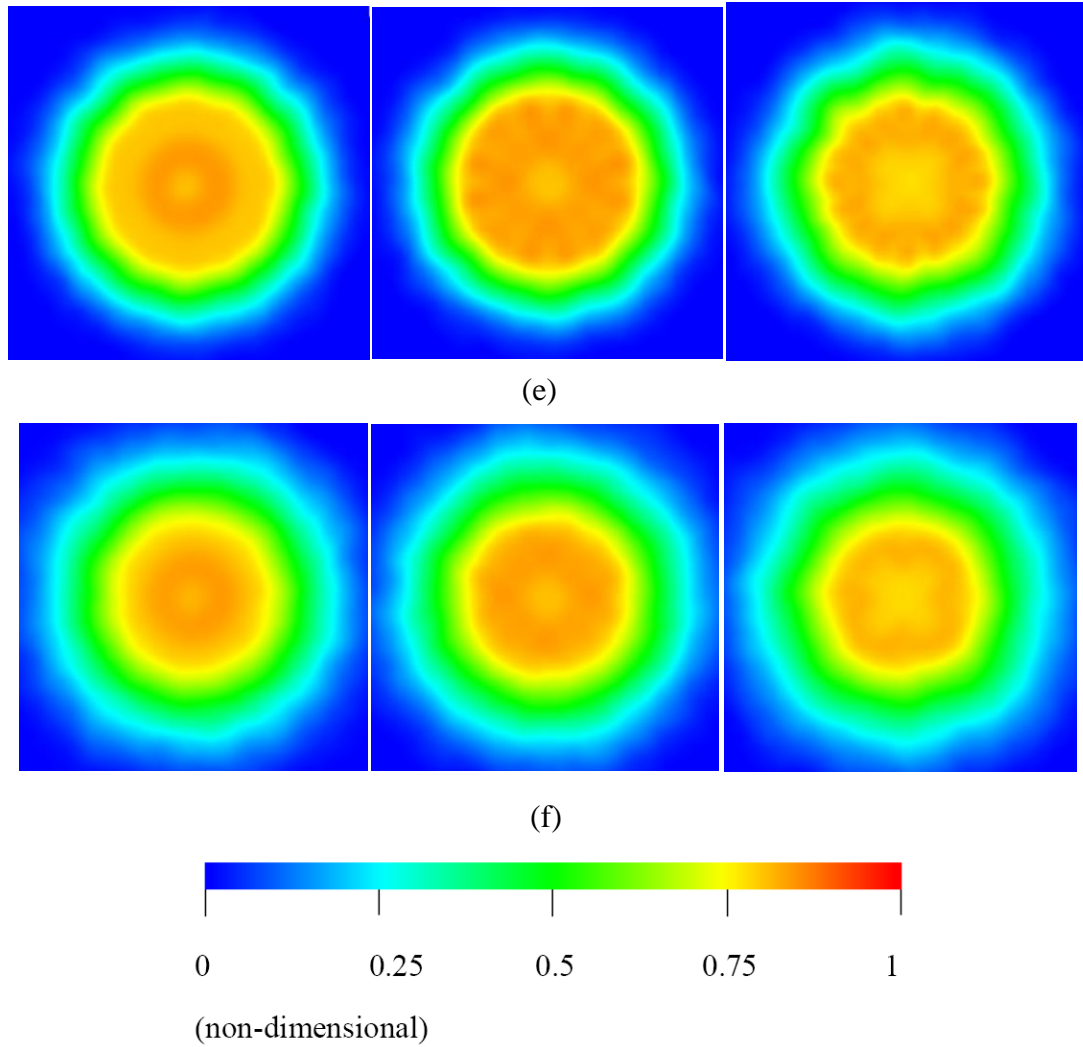
(e)

(f)

0   0.25   0.5   0.75   1

(non-dimensional)

Figure 3.10: Transwise views of mean streamwise velocity contour at different streamwise locations. From left to right: confluent mixer, 12CL, 20UH; (a): at mixer exit plane; (b): at nozzle exit plane; (c): $1D_j$ downstream of the nozzle exit; (d): $2D_j$ downstream of the nozzle exit; (e): $3D_j$ downstream of the nozzle exit; (f): $4D_j$ downstream of the nozzle exit.
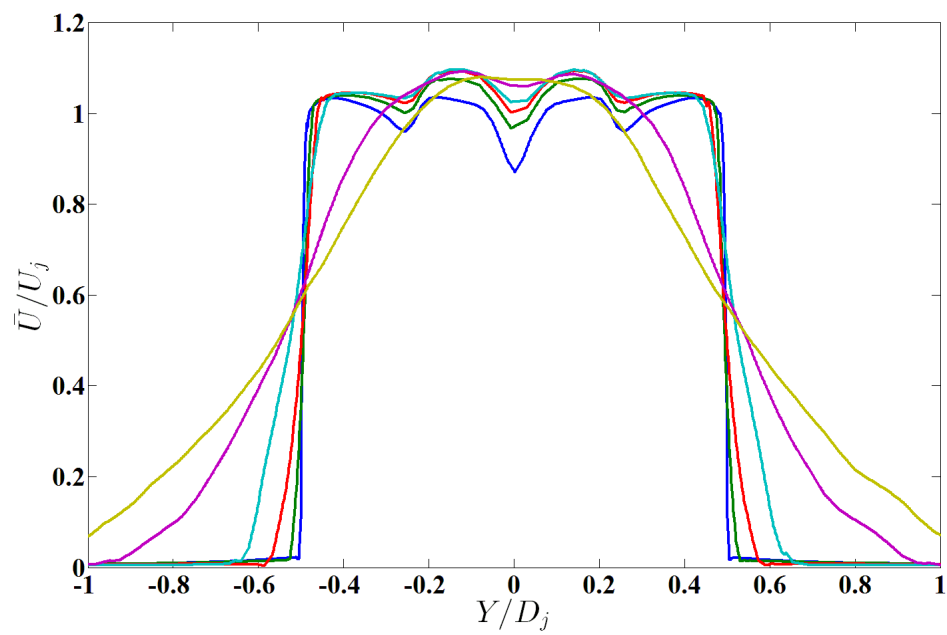
(a)
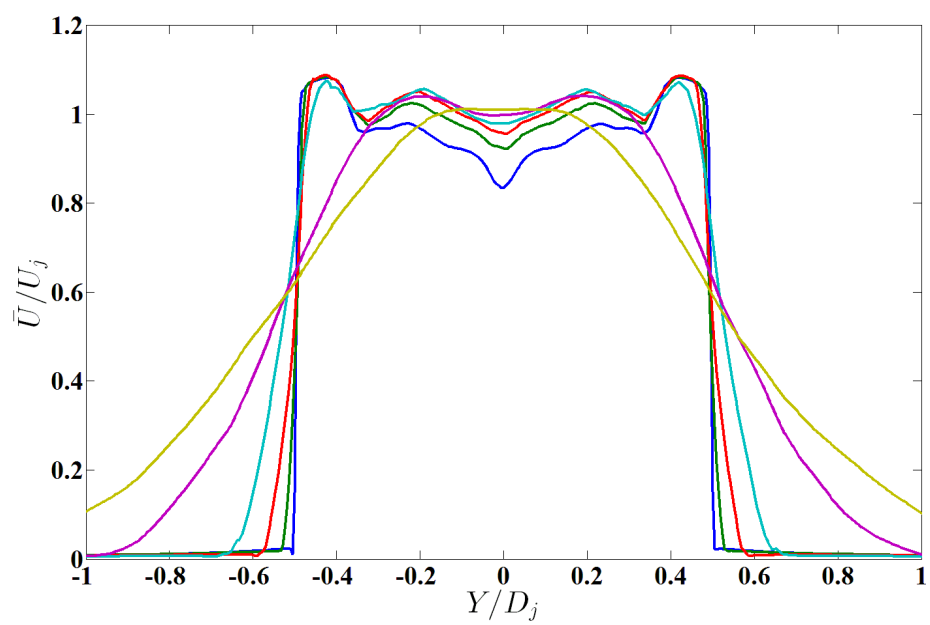
(b)
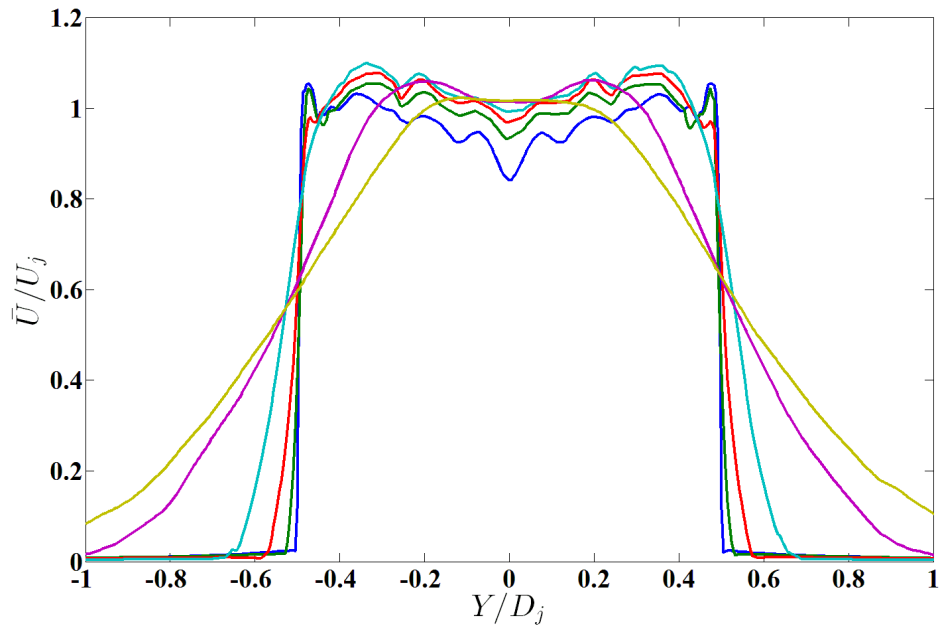
(c)

Figure 3.11: Downstream plume survey of mean streamwise velocity across transverse cross-section of the jet at different downstream locations. (a): confluent mixer; (b): 12CL; (c): 20UH. Dark blue line: at nozzle exit plane; green line: $0.2D_j$ downstream of the nozzle exit; red line: $0.5D_j$ downstream of the nozzle exit; light blue line: $1D_j$ downstream of the nozzle exit; purple line: $3D_j$ downstream of the nozzle exit; brown line: $5D_j$ downstream of the nozzle exit.
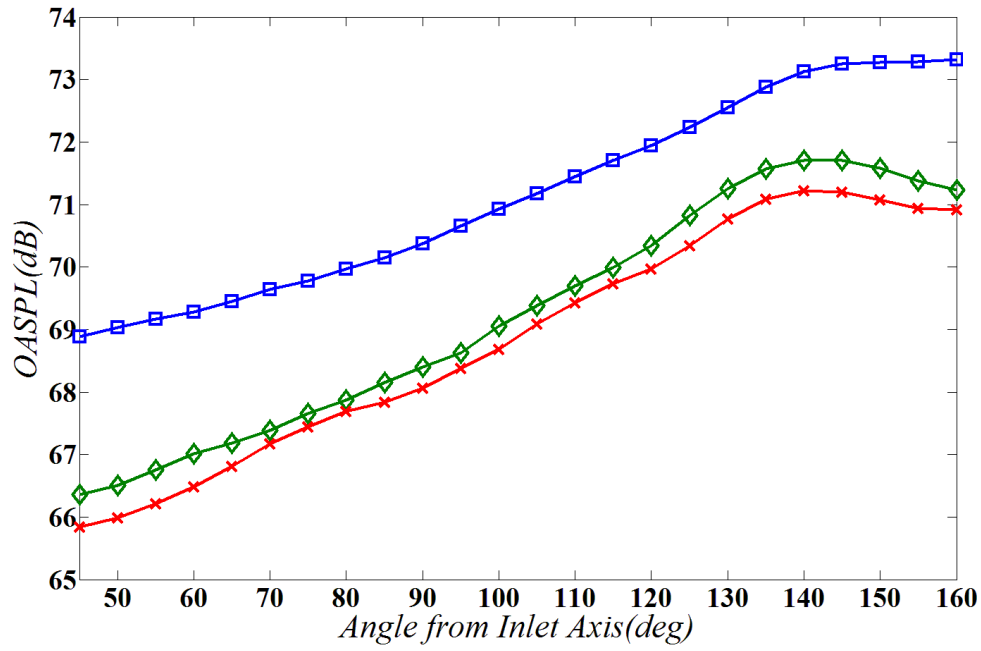
Figure 3.12: OASPL directivity. □: confluent mixer; ◇: 12CL; ✳: 20UH.
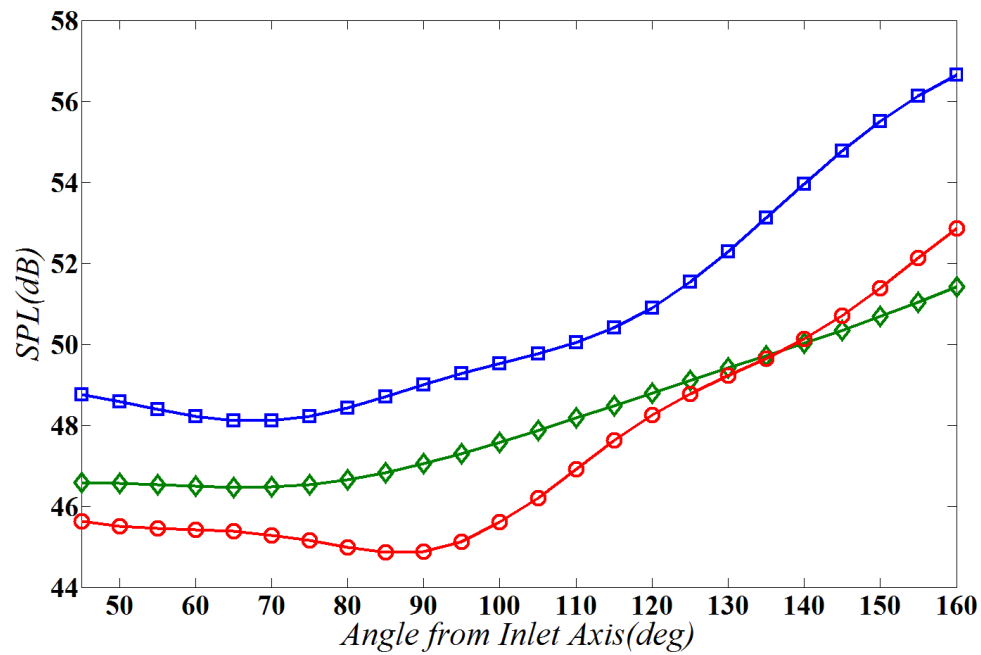
Figure 3.13: Band-passed 120hz SPL directivity. □: confluent mixer; ◇: 12CL; ✳: 20UH.
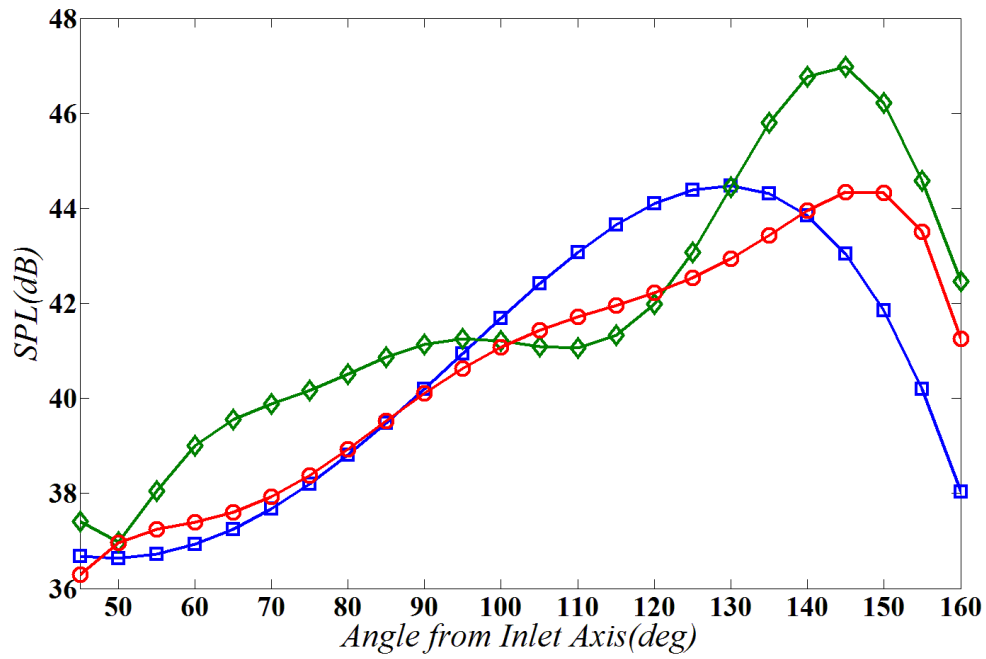
Figure 3.14: Band-passed 1200hz SPL directivity. ⊟: confluent mixer; ◇: 12CL; ✳: 20UH.
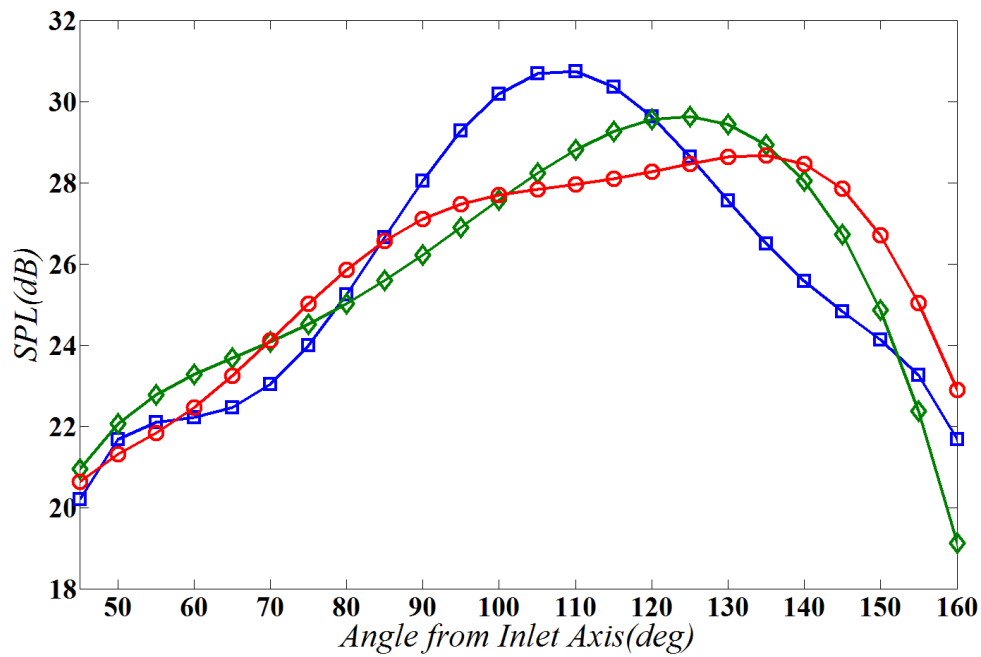
Figure 3.15: Band-passed 4500hz SPL directivity. ⊟: confluent mixer; ◇: 12CL; ✳: 20UH.

Chapter 4 Effects of Scalloping

In this chapter, effects of scalloping of the lobe mixers are discussed. A group of three 20-lobe high-penetration mixers with various scalloping depth was investigated. The confluent mixer was chosen as the baseline. Instantaneous and time-averaged flow results and statistics were obtained. Plume survey data is shown in terms of local velocity distribution across transverse cross-sections of the jet at different downstream locations. Overall sound pressure level (OASPL) and sound pressure level (SPL) directivity results are also reported for the four mixers to characterize the far-field radiated noise. The results are in qualitative agreement with experimental data.

4.1 Aerodynamic Results and Analysis

The same operating conditions (i.e., velocity and static pressure) were imposed in the simulation for the four mixer-nozzle configurations. All four models had the same fan inlet and core inlet area, therefore the bypass ratios were also the same. Figure 4.1 (a) to (c) shows instantaneous streamwise velocity contours for the four cases. These are slices along the jet centerline, through the lobe crests. The exit jet velocities for the three 20-lobe mixers were almost the same, at around 141m/s (Mach 0.406), while the confluent mixer had an exit jet velocity of 142.5 m/s (Mach 0.411). Transition from laminar to turbulent for the three lobed mixers occurred upstream of confluent mixer. The 20UH and 20DH mixers turned fully turbulent at around 0.8 D_j downstream of the nozzle exit, while 20MH underwent transition at around 0.4 D_j. This quantitative difference should result in differences between turbulent kinetic energy levels and far-field sound pressure levels. Whether or not the 20MH mixer is distinct from the other two lobed mixers is examined in the next sections. Because the potential jet core length is often used as an indicator of noise level, the values for the

four cases are compared. The length of the potential core is defined here as the distance over which the jet centerline velocity is reduced to 95% of its peak value, $U_{centerilne}(x_{centerline}) = 0.95U_{peak}$. The values of the potential core lengths are listed in Table 4.1. Note that as scalloping depth increased, the potential core length decreased. The jet core length of 20DH was 8.7% shorter than that of the 20UH mixer.

Figures 4.2 (a) to (d) show close-up views of the instantaneous vorticity inside the four nozzles. In comparison with lobed mixers, the confluent mixer does not exhibit significant mixing between core and fan streams. In contrast, the three lobed mixers do exhibit extensive mixing inside the nozzle. Flow separation along the lobe crest is observed, due to the high penetration depth. Vortices are initiated and shed from the lobe almost immediately downstream of the mixer exit. These vortices are then convected over the nozzle lip shear layer, increasing the turbulent intensity level. Because scalloping led to upstream mixing and interaction between the two streams, the lobe width may not constitute an appropriate characteristic length for the streamwise vortices. There are some differences, therefore, between the vortex shedding patterns of the three lobed mixers. Increased dissipation occurred downstream of the mixer exit as the scalloping depth was increased. In contrast to 20UH, the 20DH mixer produced more small-scale vortices. This is because the distance over which mixing occurs for 20DH is greater than for the 20UH. At the mixer exit plane, 20DH is already partially mixed while the 20UH mixer is only slightly beyond mixing initiation. It was mentioned in the last chapter that a high penetration depth, or lobe height, tends to lead the shed vortices towards the nozzle wall and away from the jet center line. It is interesting to see here that the path of the two scalloped mixers vortices is directed towards the jet flow central region interacting with the flow further downstream. This implies that the introduction of scalloping produced an effective lobe penetration that is no longer characterized by the lobe height only. Both the scalloping depth and the lobe height should be taken into account for a better characterization of the vortex-affected area.

Lambda 2 criterion iso-surface was shown in Figure 4.3 (a) to (d). Mixing was

initiated along the scalloping profile in the two scalloped mixers. The mixing for the 20MH and 20DH cases, indeed, started earlier than that for the 20UH unscalloped mixer.

Figure 4.4 (a) to (d) shows the 3D mean streamwise velocity contour at the nozzle exit plane. The three lobed mixers had more uniform velocity profiles than the confluent mixer. Furthermore, the two scalloped mixers had more uniformity than the 20UH mixer. The 20DH mixer seemed to have a better mixed flow profile than 20MH. The clear 'footprint' of the lobe in 20UH was not seen in 20MH or 20DH. Qualitatively, the high velocity gradient region was closer to the nozzle wall in the scalloped mixers. The energy loss caused by flow separation behind the center body led to the velocity deficit in the center region of the contour.

Figure 4.5 (a) to (d) shows the time-averaged mean streamwise velocity contours both inside and outside the nozzle. There were velocity 'hot spots' at the nozzle exit wall for all the cases. The 20DH mixer appeared to have a more uniform velocity profile from the nozzle exit to several jet diameters downstream. It has been said that the design philosophy behind scalloping is to introduce axial vorticity gradually into the flow so that fan and core stream mixing can proceed more gradually than in the unscalloped mixer. The most intense turbulence spots are then acoustically shielded by the nozzle duct. This does not necessarily lead to a more uniform velocity profile by the time the two streams reach the nozzle exit plane; however, it tends to reduce the mid-to-high frequency noise generated by internal mixing and by the interaction of the partially mixed flow with the ambient.

A centerline mean streamwise velocity comparison is shown in Figure 4.6. Within the first jet diameter downstream of the nozzle exit, all four cases experienced a rapid increase and reached a relatively stable stage, until the values started to decay at around six jet diameters. The 20UH and 20MH mixers reached a peak value upstream of the confluent mixer, and there was no significant difference between these two cases. The 20DH mixer is distinct from the other two lobe mixers. It featured a steady velocity increase from the nozzle exit to four diameters downstream. Its peak value

was nearly the same as that of the confluent mixer. The magnitude was 7% larger than that of the 20UH mixer. This might be attributed to the interaction between the vortices shed from the 20DH mixer and the downstream jet flow, as shown in Figure 4.2 (d). The 20MH mixer also featured a similar vortex shedding pattern. A more plausible explanation needs to be found to clarify this phenomenon. The impact on the far-field sound level is discussed in the next section. Further downstream, beyond ten jet diameters, all the cases exhibited a similar decay rate.

Figure 4.7 (a) to (d) shows the time-averaged mean turbulent kinetic energy contours for the four mixers. The low energy level close to the nozzle exit indicated a nearly laminar exit shear layer. A difference between the turbulent kinetic energy concentration location was observed among the four cases. The fully turbulent state was reached at around $0.6D_j$, $0.4D_j$, $0.2D_j$, and $0.5D_j$ downstream to the nozzle exit plane for confluent, 20UH, 20MH, and 20DH mixers respectively. The lobed mixers turbulent kinetic energy was concentrated closer to the nozzle than for the confluent mixer, as expected. The increase in scalloping depth did not lead to a monotonic variation of the downstream peak locations. As illustrated in Figure 4.1, the 20MH mixer flow transition is upstream to that of the other cases. For all three mixer-nozzles, vortices shed from the mixer tips were convected into the nozzle lip shear layer. The strengths of the vortices in the three mixers were different. It is reasonable to infer that the medium scalloping depth of 20MH allowed proper vortex growth producing the strongest vortices near the nozzle wall. In comparison, 20UH only started to form vortices after the mixer exit, and the distance over which the vortices developed might not be long enough. On the other hand, vortices inside the 20DH mixer were formed much earlier, but by the time those vortices entered the downstream shear layer they were already partially dissipated. The peak turbulent kinetic energy magnitude of 20MH along the nozzle lip line was 18% higher than those of 20UH and 20DH.

Figure 4.8 presents the normalized centerline mean turbulent kinetic energy variation along the downstream direction. The confluent mixer produced the highest turbulent kinetic energy level among the four cases. The turbulent kinetic energy level

of the three lobed mixers reached a peak value at approximately the same location, nine jet diameters downstream of the nozzle exit. The two scalloped lobed mixers had relatively higher levels than 20UH. This confirmed the previous presumption that the vortices shed from the scalloped mixer interacted with the jet flow near the centerline region, and modified the downstream flow development.

Figure 4.9 (a) to (f) shows the mean streamwise velocity contour at different streamwise locations downstream of the exit. As seen in Figure 4.9 (a), small-scale vortices were found at the crest and valley of the lobes. The 20MH mixer had larger and stronger vortices than the other two in the lobe valleys. This fact can be explained using the previous reasoning: the 20MH mixer offered the appropriate distance for vortex development and strengthening; 20UH started to form vortices at a later stage, and hence did not evolve over a long enough distance to acquire sufficient energy; although the vortices inside the 20DH mixer were formed and shed earlier, they were dissipated to some extent when they reached the downstream shear layer. From Figure 4.9 (b), it is evident that the 20MH and 20DH mixers did not preserve the lobe shape 'foot print' at the exit. Due to the same lobe penetration, the axial vortices had approximately similar radial locations for the three lobed mixers. The 20MH and 20DH mixers appeared to yield more uniform profiles at the nozzle exit. Beyond one jet diameter, the growth of the shear layer thickness began to diffuse the lobe pattern, as shown in Figure 4.9 (c) to (f). The transwise velocity contours tend to be axisymmetric further downstream.

Figure 4.10 (a) to (d) shows a plume survey of the mean streamwise velocity across transverse cross-sections of the jet at different downstream locations. For all cases, the initially complex velocity profile gave way to a simpler plume profile further downstream. Velocity deficits caused velocity gradients in the vicinity of the jet center line. High velocity gradients existed for all the mixers, from the nozzle exit to one diameter downstream. It appeared that the high velocity gradient of the 20MH mixer started to decrease earlier than the others.

In Table 4.2, the comparison of the mean thrust coefficients between the four

cases were made. The values were found to be close to each other.

4.2 Acoustic Results and Analysis

Figures 4.11 to 4.14 show the OASPL directivity and the associated SPL spectrum for the confluent, 20UH, 20MH, and 20DH mixers. Recall that the results were obtained for a stationary medium. The fixed virtual probes were located along a circle with a radius of 45m ($21D_j$), covering the angles from 45 to 160 degree relative to the nozzle inlet axis.

The OASPL level of the confluent mixer was again the highest. Among the three 20-lobe mixers, 20MH was the loudest and 20DH was the quietest. Previous experimental results indicate that the effect of the scalloping depth on the far-field sound pressure level does not obey a linear relation[72]. Aerodynamic results from Figures 4.1 and 4.7 confirmed this notion. The three mixers had a similar OASPL trend. The OASPL level of the 20DH mixer was on average 2 dB lower than 20MH, and 1 dB lower than 20UH. The largest reduction of 4 dB was obtained at 45 and 160 degrees, when comparing confluent and 20DH OASPL levels. The peak magnitude was reached at a 140-degree angle for the lobed mixers. There was a scalloping depth threshold to determine whether scalloping would bring noise reduction benefit or penalty. The medium scalloping of 20MH seemed to be below that value. The deep scalloping of the 20DH mixer, on the other hand, was over that threshold and brought the expected noise reduction benefit.

Some interesting points arise when looking at the SPL directivity at 120 hz in Figure 4.12. The magnitude of all mixers' SPL level peaked at the 160 degree angle. This is because the jet plume decayed far downstream of the nozzle exit, where large eddies governed the low frequency domain. The 20UH mixer had the lowest level of all, almost 4 dB lower than the confluent and 20MH mixer at shallow angles. Surprisingly, the 20MH mixer emissions were similar to those for the confluent mixer at locations downstream of 145 degrees. 20 DH did not yield significant suppression of low frequency noise, as indicated by experimental results[72,73]. The introduction of

scalloping did not yield the same low-frequency noise reduction advantage as the 20UH unscalloped mixer, although the scalloped mixers provided reduction benefits in the low-frequency domain. Because of scalloping and the fact that the vortex length was not characterized by the lobe width, the development and size of the shed vortex were changed. This impact can be brought to the further downstream jet flow to modify the low-frequency noise radiation mechanism, as indicated in Figure 4.2 (c) and (d). The relatively high low-frequency level partly explained the higher OASPL level of 20MH.

Figure 4.13 shows the 1200 hz SPL directivity comparison among the three mixers. As with the experimental results[72], the confluent mixer had lower a mid-frequency sound pressure level than lobed mixers. 20MH had the highest SPL level among the four cases at angles upstream of 115 degrees. 20MH was the quietest mixer downstream of 135 degrees. The 20DH mixer had a higher mid-frequency level than confluent and 20UH at angles between 45 and 90 degrees. Now recall that the 20MH mixer had the highest peak turbulent kinetic energy level in the nozzle shear layer. It also had the turbulent kinetic energy concentration region closest to the nozzle exit. Turbulent kinetic energy in the shear layer is a major contributor to the mid-to-high frequency noise, and mid-to-high frequency noise is generally located near the nozzle exit[81]. This can explain why at angles of 45 to 125 degrees 20MH had higher mid-frequency noise level. This should also be the case in the high-frequency domain. Noise from the three lobed mixers peaked at different locations: 150 degrees, 120 degrees, and 140 degrees for the 20UH, 20MH, and 20DH mixers respectively. There was clearly a correlation between the scalloping depth and the peak angle, but further investigation is beyond the scope of the current study.

The SPL directivity comparison at 4500 hz is shown in Figure 4.14. Upstream of 125 degrees, 20MH had the highest high-frequency SPL level among the lobed mixers, as mentioned earlier. Downstream of 125 degrees, the 20UH mixer produced higher levels than the others, while the 20MH and 20DH mixers shared a similar SPL trend and magnitude. From 85- to 125-degree angles there was an SPL variation associated

with the scalloping depth. In that range, 20DH had the lowest level. Combining Figures 4.12 and 4.14, it appears that scalloping tended to trade part of the advantage of suppressing low-frequency noise for decreasing the noise in the high-frequency domain. The 20UH, 20MH, and 20DH mixers peaked at 135 degrees, 115 degrees, and 120 degrees respectively. In addition to a peak shift due to the geometry difference, there was also an upstream peak shift related to an increase in frequency domain for the three cases. That is presumably because high frequency noise near the nozzle exit plane or inside the nozzle may have been emitted to upstream locations.

In summary, all three lobed mixers were quieter than the confluent mixer. There seemed to be a threshold that determined the benefit or penalty scalloping could bring to noise reduction. In terms of OASPL and SPL directivity, 20MH distinguished itself from the other two mixers because of its high turbulent kinetic energy concentration near the nozzle exit. It was the significant suppression of 20UH in the low-frequency domain that made it the second quietest mixer. The improved reduction in the high-frequency domain of the 20DH mixer led to the lowest OASPL level of the mixers tested. Finally, the peak angles of the three mixers' SPL level were found to be shifted upstream when the investigated frequency was increased.

4.3 Summary

As in the Fisher *et al.*[82] coaxial jet model, there appears to be at least two dominant regions of frequency in lobed mixers. One is the low-frequency peak governed by the fully mixed region far downstream and the other is the mid-to-high frequency peak governed by the shear layer between the ambient and the partially mixed fan-core flow close to nozzle exit. The geometry of the lobed mixer and changes to the mixing process can be used beneficially to control one or the other of these peaks. The unscalloped 20UH mixer produced a substantial reduction in low-frequency noise compared to the confluent design, but an increase in the mid-to-high frequency domain at angles downstream to 140 degrees was also observed. The presence of sidewall scalloping maintained the low frequency

suppression, although not as much as for the 20UH mixer, and reduced the mid-to-high frequency penalty.

The unique turbulent kinetic energy distribution of the 20MH mixer led to its differentiation from the other two lobed mixers in terms of OASPL and SPL levels. The higher turbulent kinetic energy in the shear layer apparently increased the 20MH mixer's noise level in the mid-to-high frequency domain, as reflected in Figures 4.13 and 4.14. The 20DH mixer, however, was able to suppress the mid-to-high frequency noise to some extent. On the other hand, it has been shown that in the 20MH and 20DH mixers, there were vortices going towards the flow downstream to the center body and interacting with jet flow. The effect of this was seen in the low frequency SPL directivity. Both the 20MH and 20DH mixers had higher levels than 20UH in the low frequency domain. Finally, the higher velocity peak for 20DH at five diameters downstream to the nozzle exit plane, as shown in Figure 4.6, did not seem to produce measurable consequence in the far-field sound pressure level.

Mixer ID	CONF	20UH	20MH	20DH
$x_{centerline}/D_j$	8.33	8.36	8.19	7.69

Table 4.1: Potential core length for the four tested cases.

Mixer ID	$T_{s,c}/T_{s,f}$	M_j	C_T
Confluent	1.0	0.41	1.95
20UH	1.0	0.43	1.94
20MH	1.0	0.42	1.94
20DH	1.0	0.41	1.93

Table 4.2: Mean thrust coefficient comparison between the four tested cases.
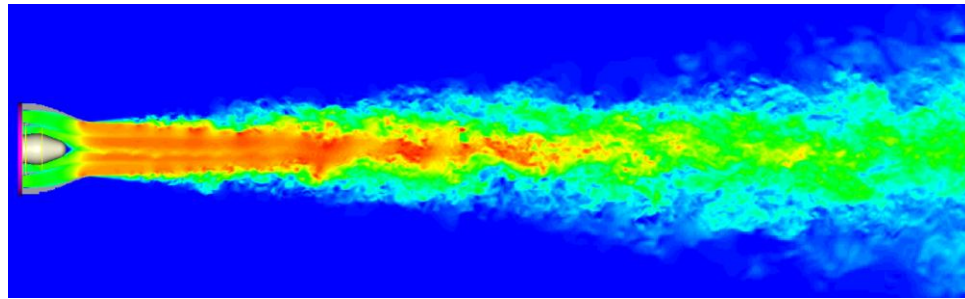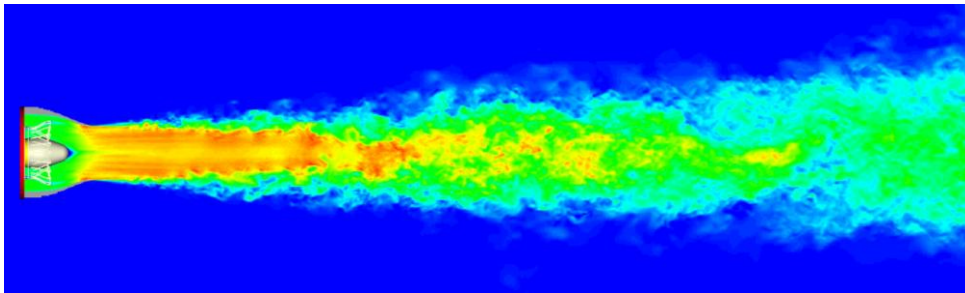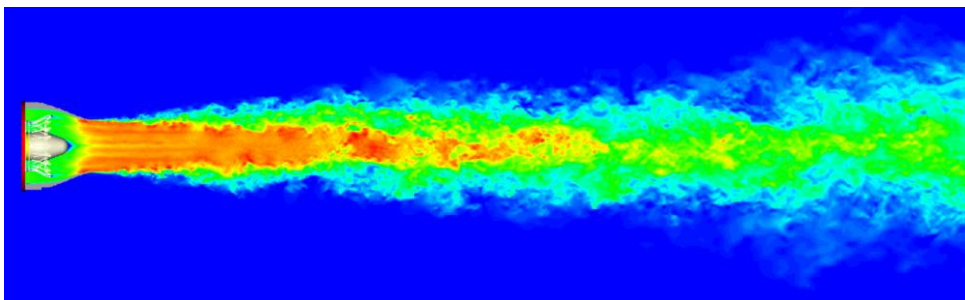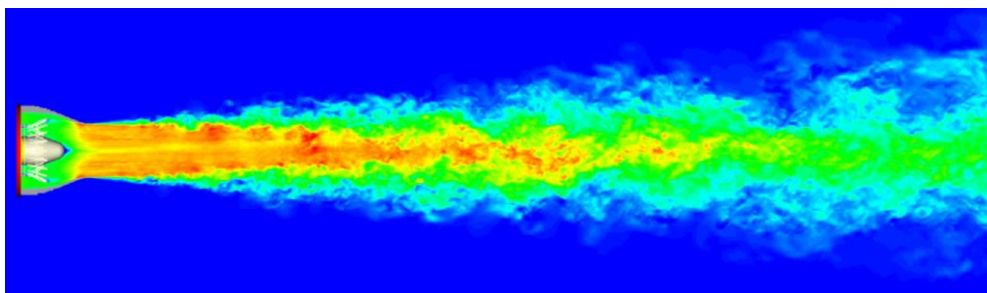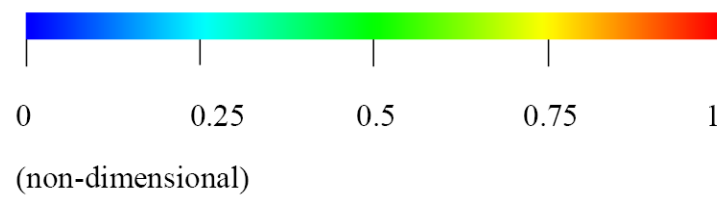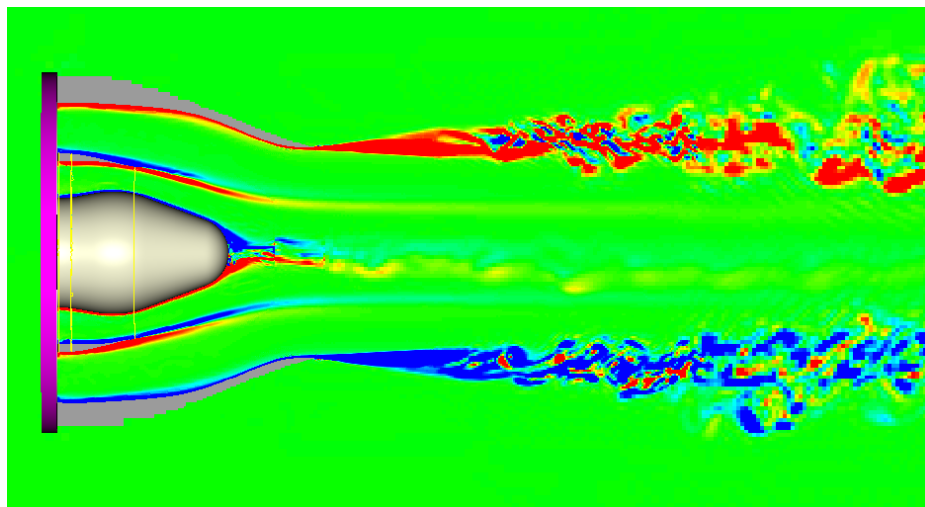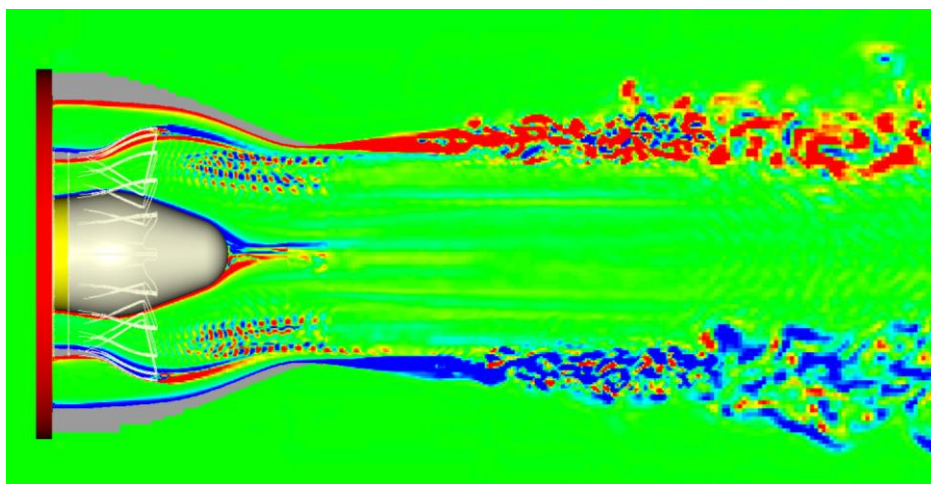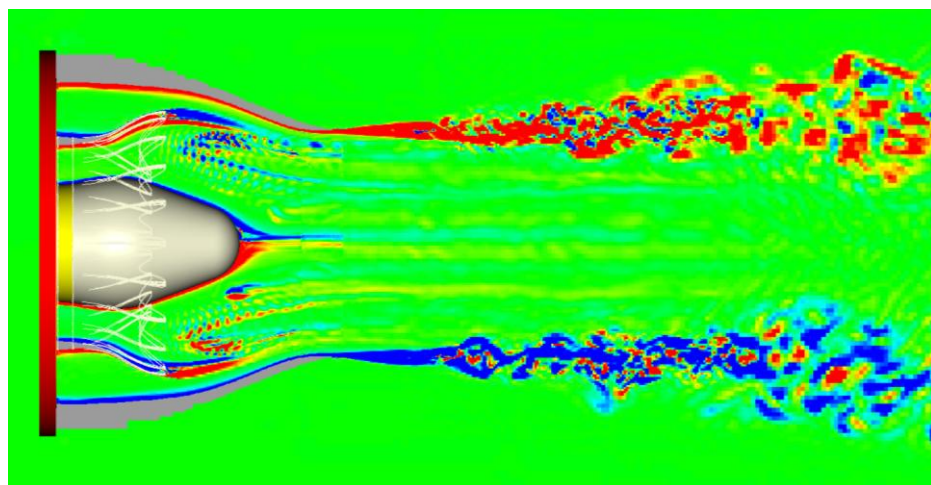
Figure 4.1: Instantaneous total velocity contours of the four mixers. (a): confluent mixer; (b): 20UH; (c): 20MH; (d): 20DH.
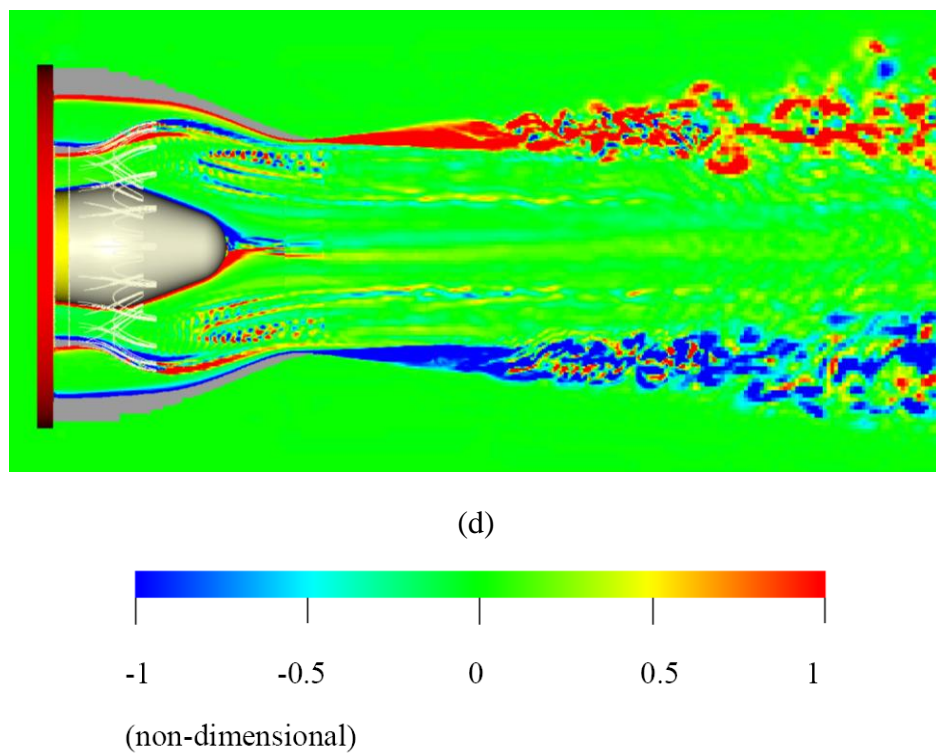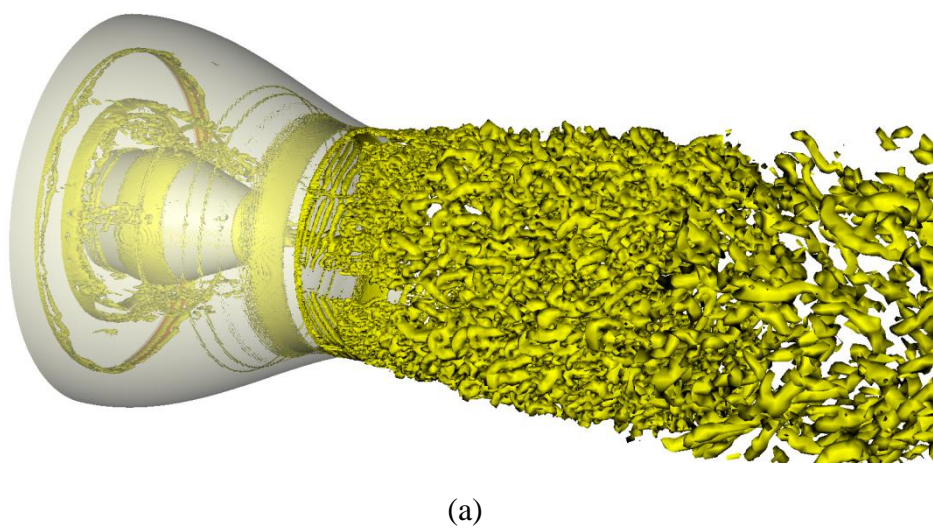
(a)

(b)

(c)

(d)

(non-dimensional)

Figure 4.2: Close-up view of instantaneous vorticity inside the four nozzles. (a): confluent mixer; (b): 20UH; (c): 20MH; (d): 20DH.

(a)
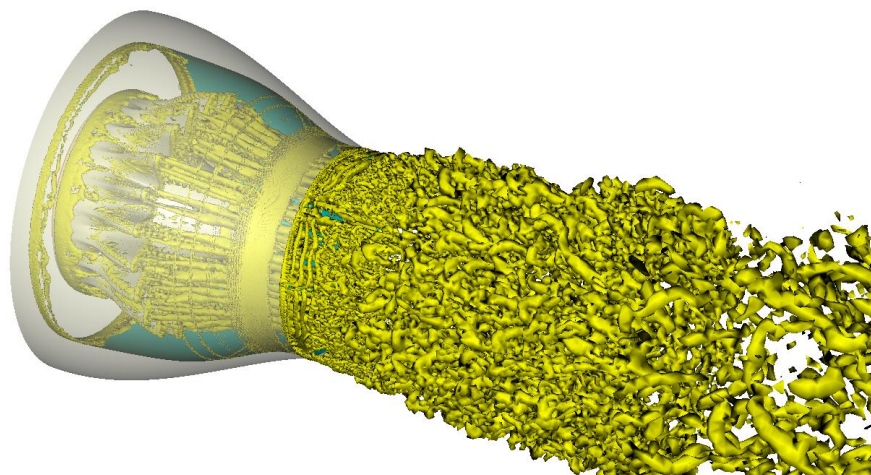
(b)
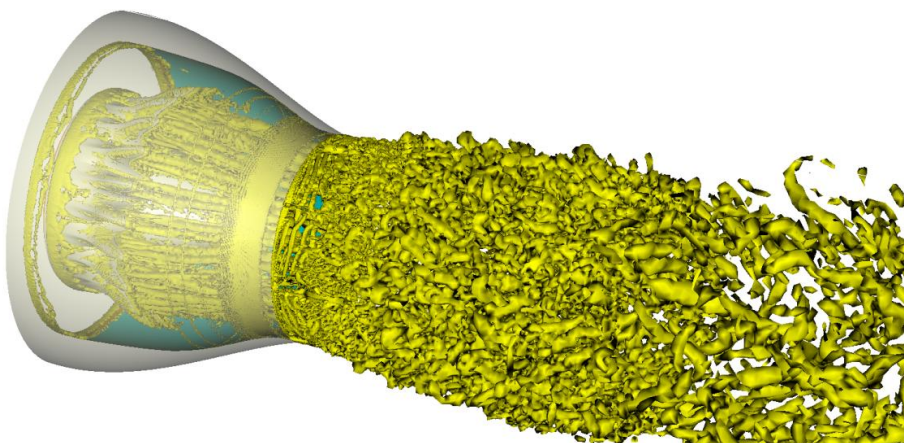
(c)
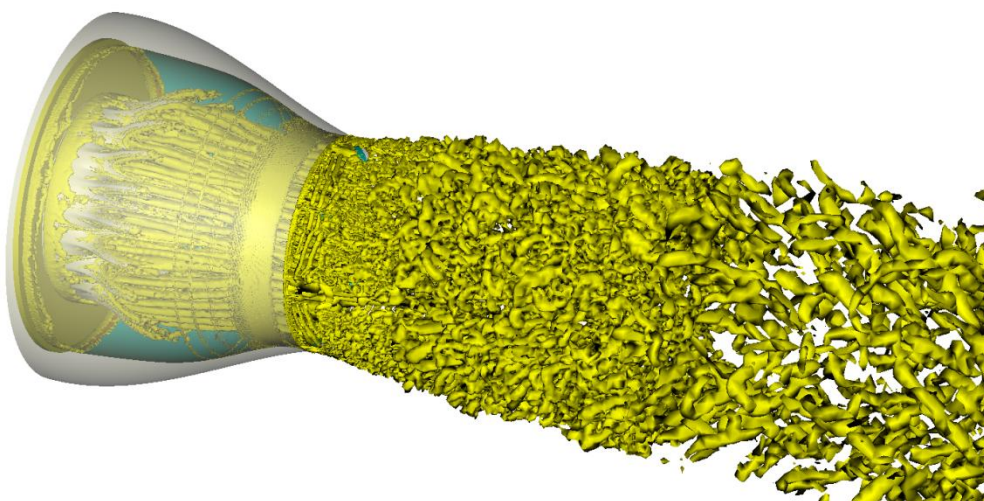
(d)

Figure 4.3: Lambda 2 criterion iso-surface for the four mixers. (a): confluent mixer; (b): 20UH; (c): 20MH; (d): 20DH. (iso-surface value = -100)
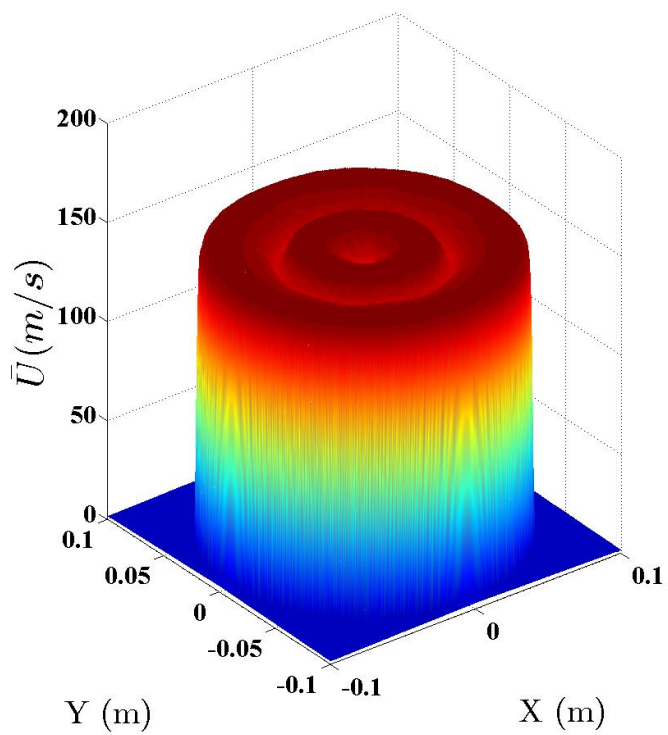
(a)
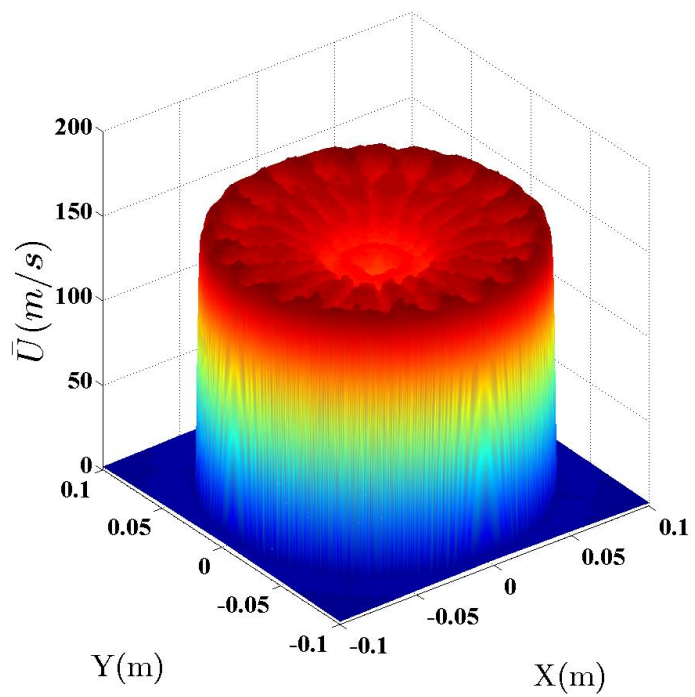
(b)
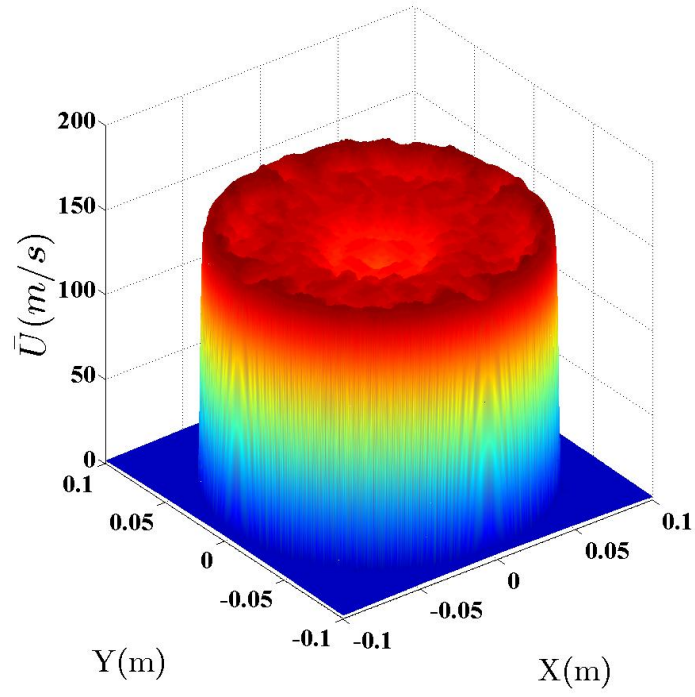
(c)
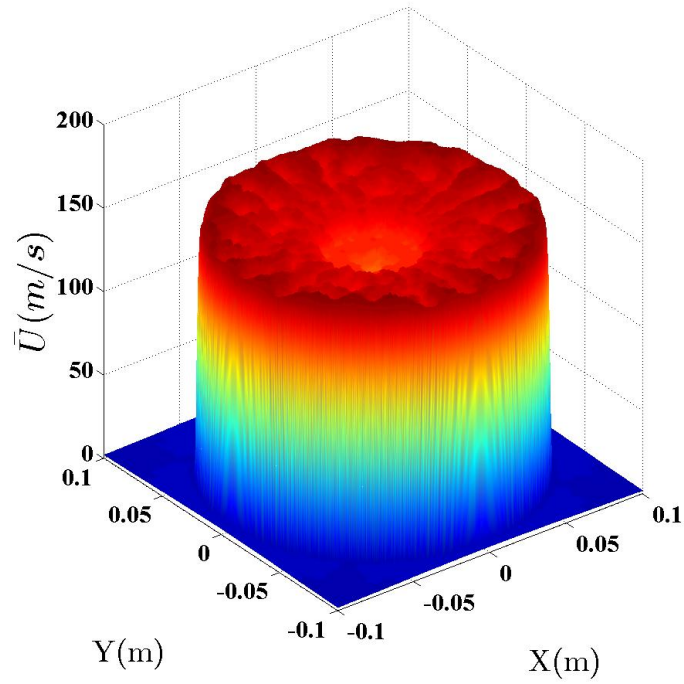
(d)

Figure 4.4: Mean streamwise velocity 3D contour at the nozzle exit plane. (a): confluent mixer; (b): 20UH; (c): 20MH; (d): 20DH.
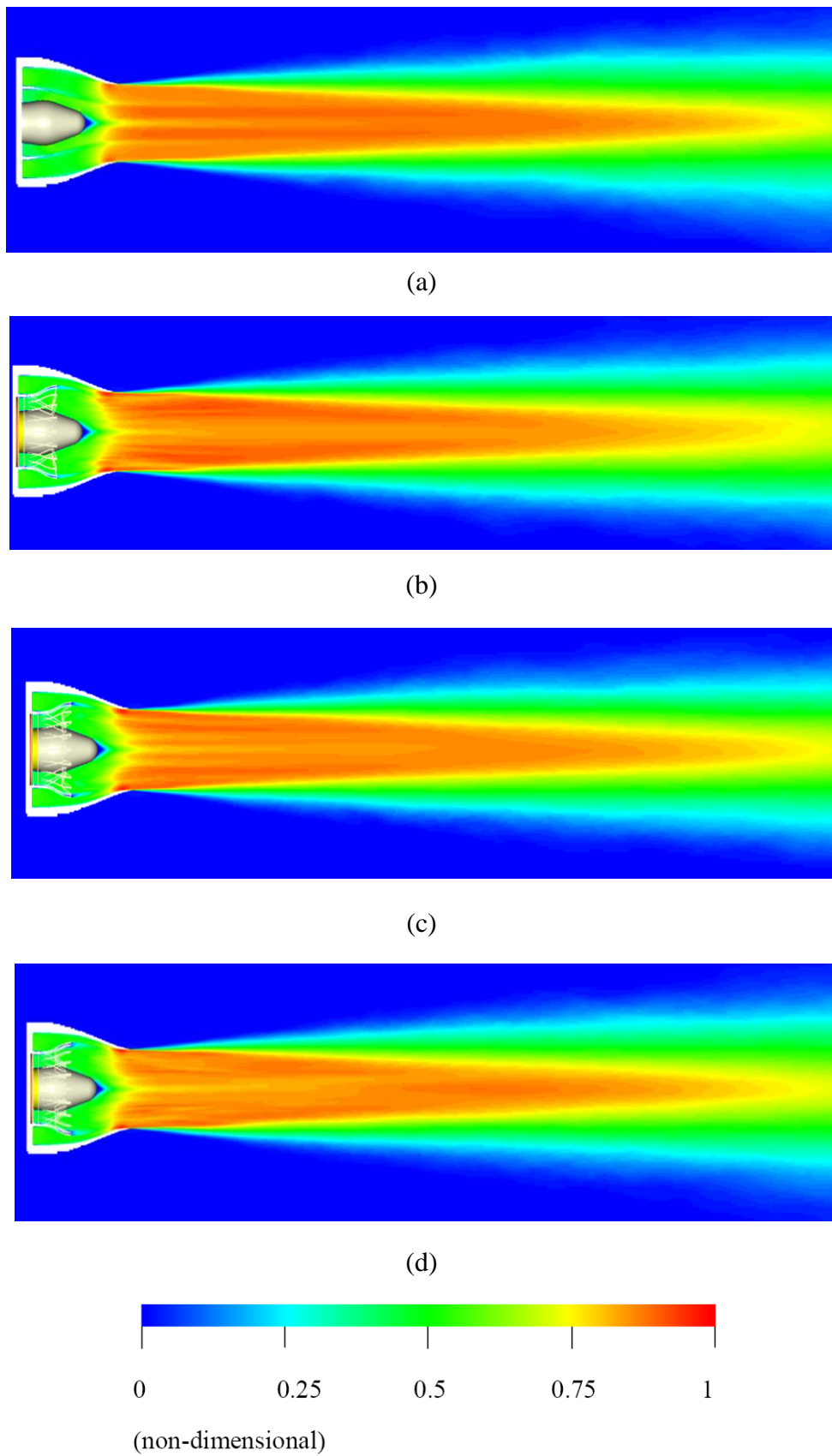
Figure 4.5: Time-averaged mean streamwise velocity contour for the four cases along jet center plane. (a): confluent mixer; (b): 20UH; (c): 20MH; (d): 20DH.
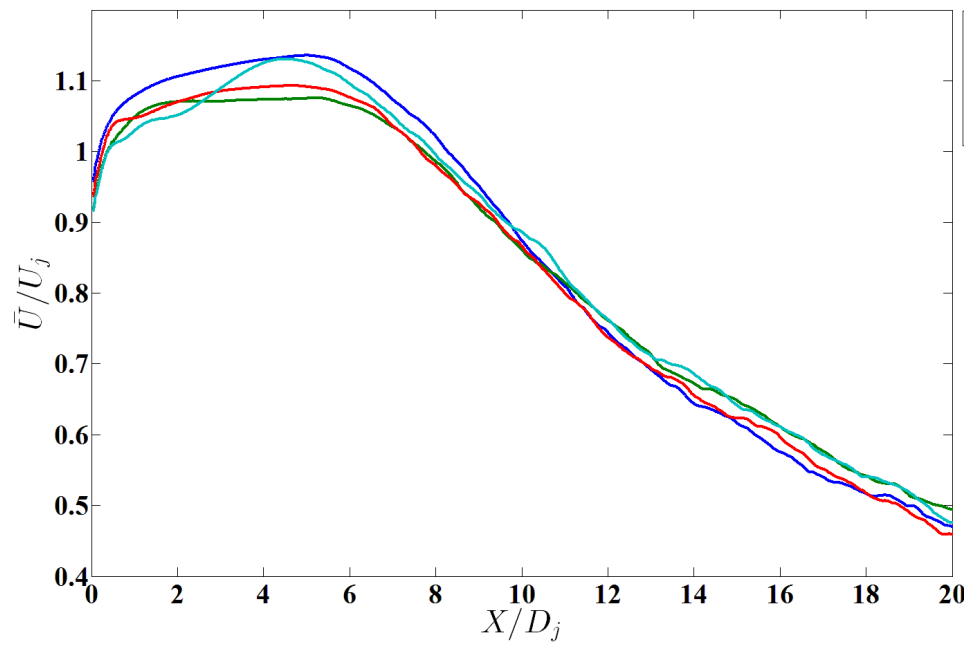
Figure 4.6: Center-line mean streamwise velocity. Dark blue line: confluent mixer; green line: 20UH; red line: 20MH; light blue line: 20DH.

(a)

(b)

(c)

(d)

0 0.25 0.5 0.75 1
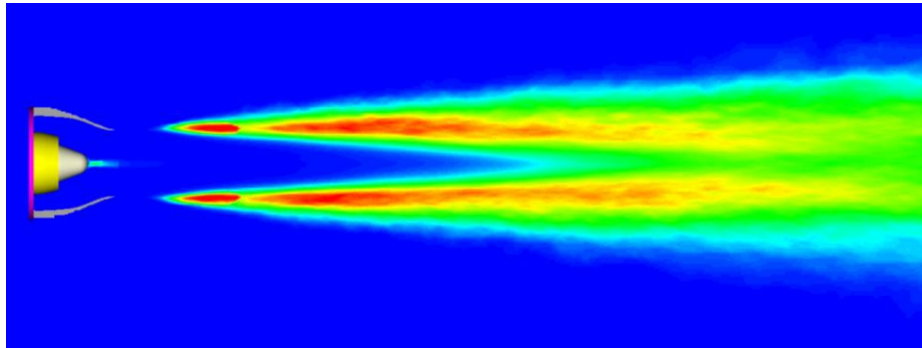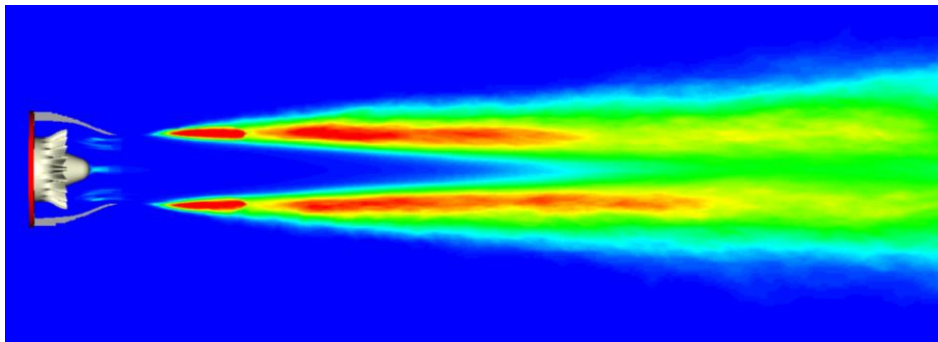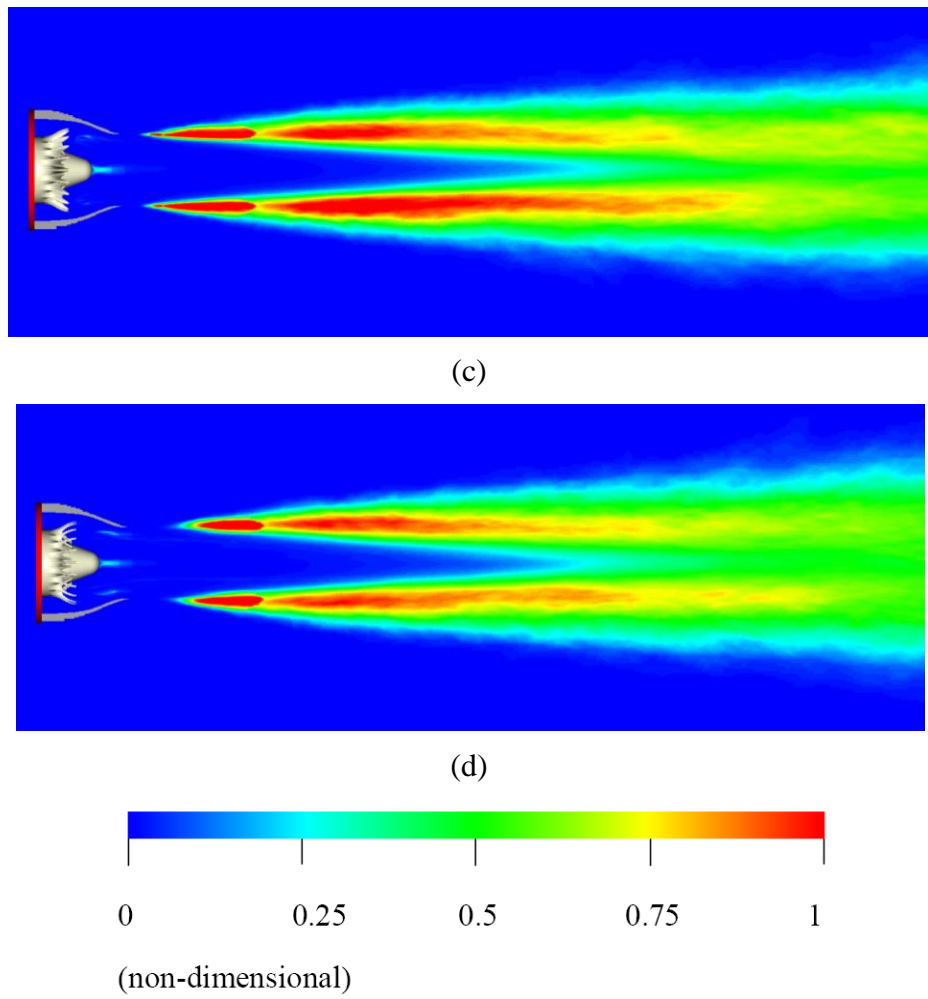
(non-dimensional)

Figure 4.7: Time-averaged mean turbulent kinetic energy contour. (a): confluent mixer; (b): 20UH; (c): 20MH; (d): 20DH.
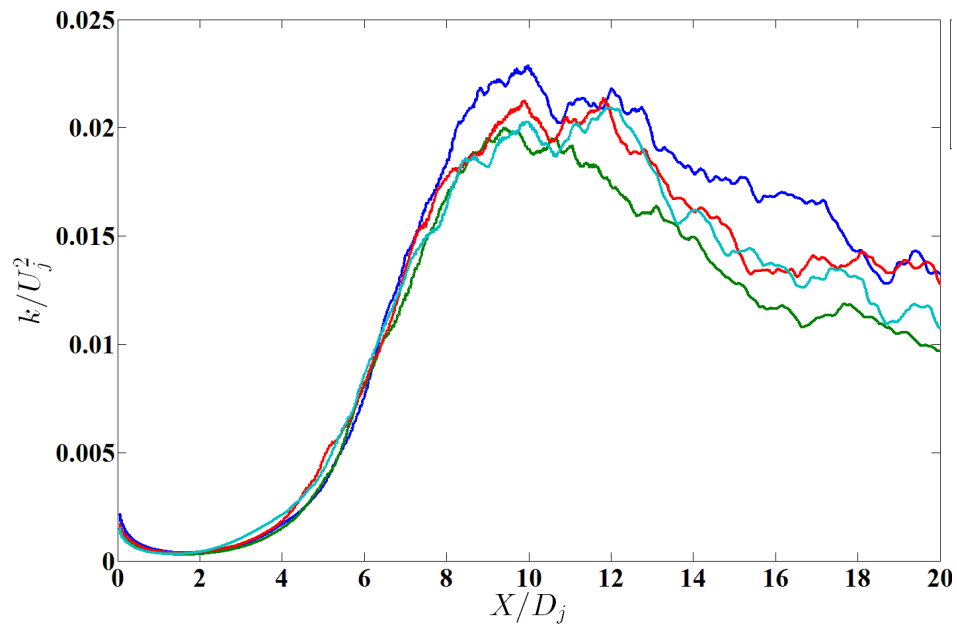
Figure 4.8: Non-dimensional center-line mean turbulent kinetic energy. Dark blue line: confluent mixer; green line: 20UH; red line: 20MH; light blue line: 20DH.
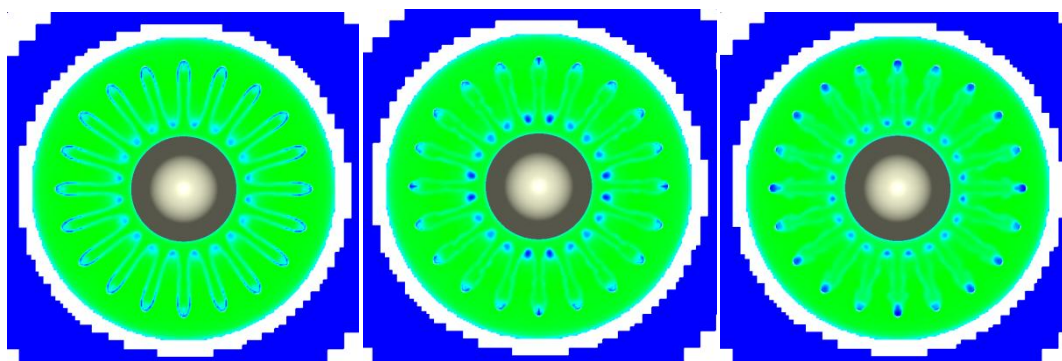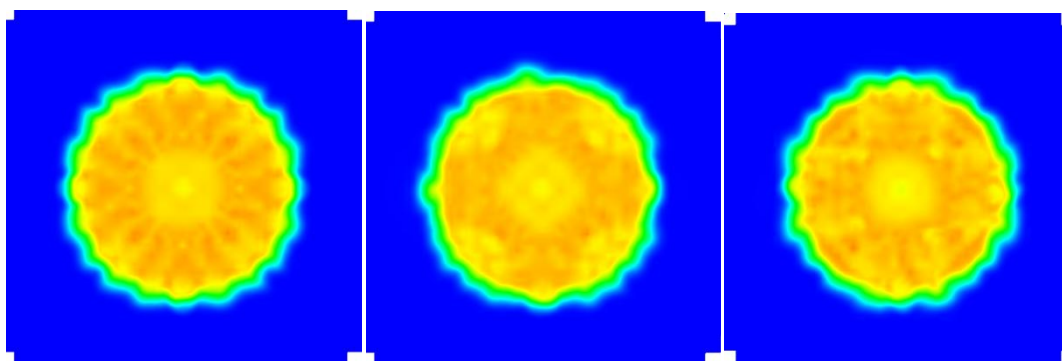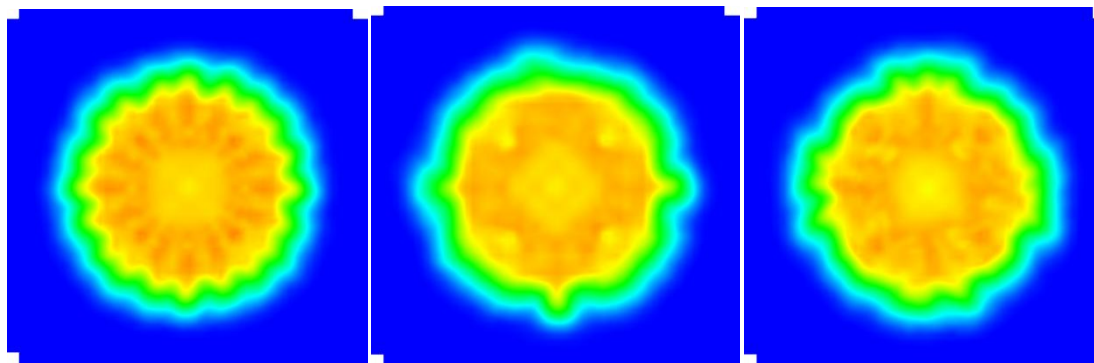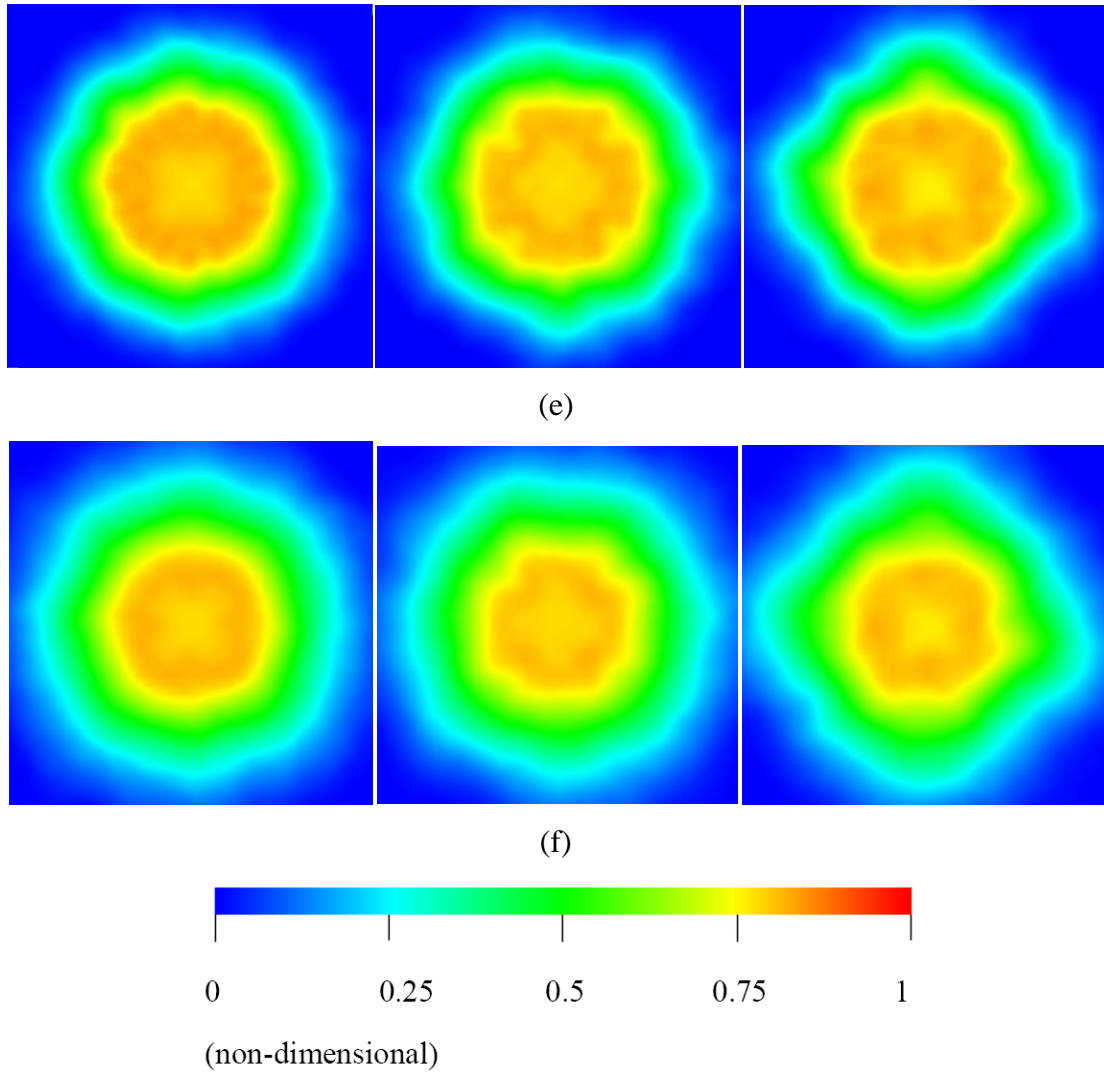
(a)

(b)

(c)

(d)

Figure 4.9: Transwise views of mean streamwise velocity contour at different streamwise locations. From left to right: 20UH, 20MH, 20DH; (a): at mixer exit plane; (b): at nozzle exit plane; (c): $1D_j$ downstream of the nozzle exit; (d): $2D_j$ downstream of the nozzle exit; (e): $3D_j$ downstream of the nozzle exit; (f): $4D_j$ downstream of the nozzle exit.
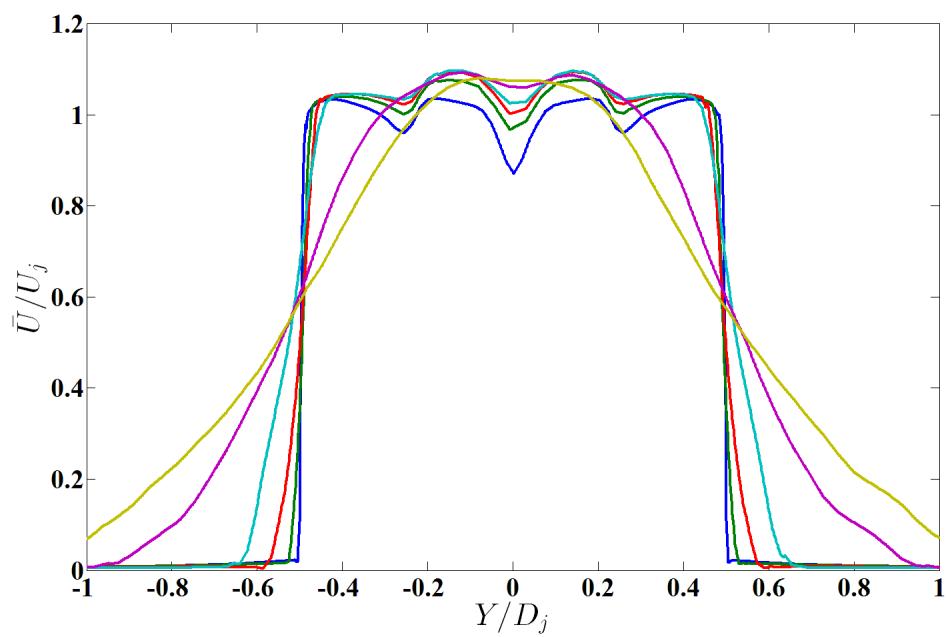
(a)
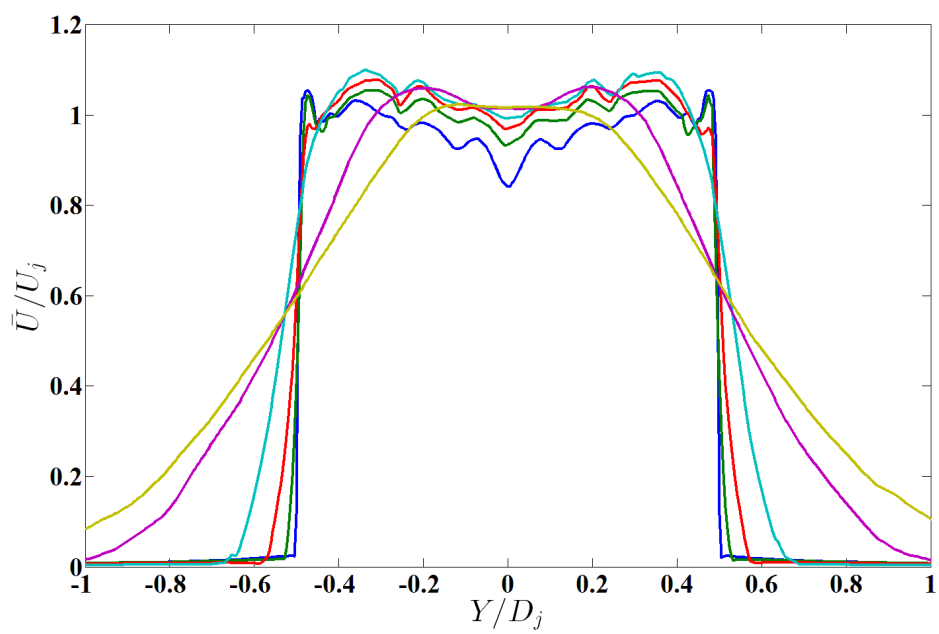
(b)
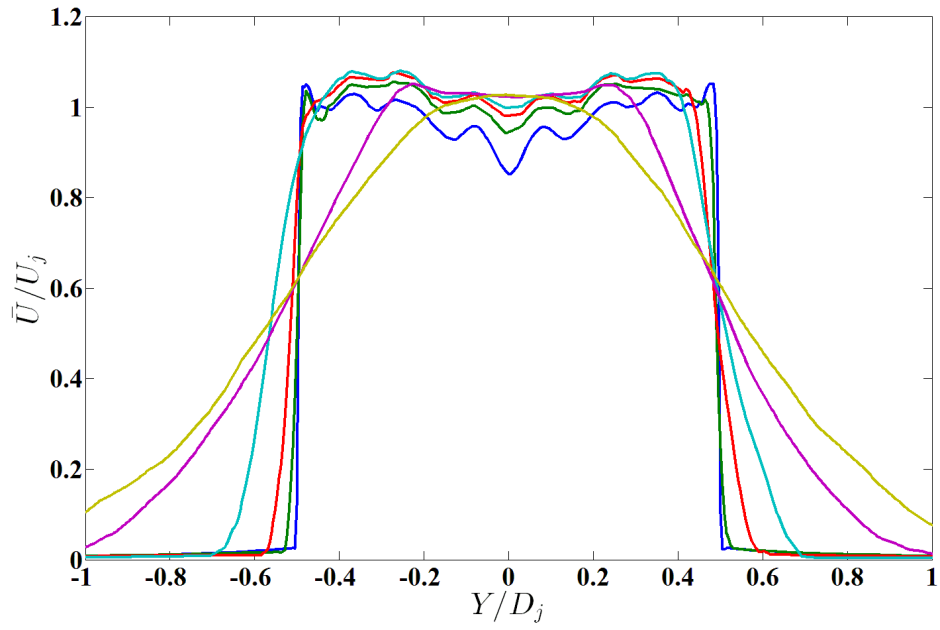
(c)
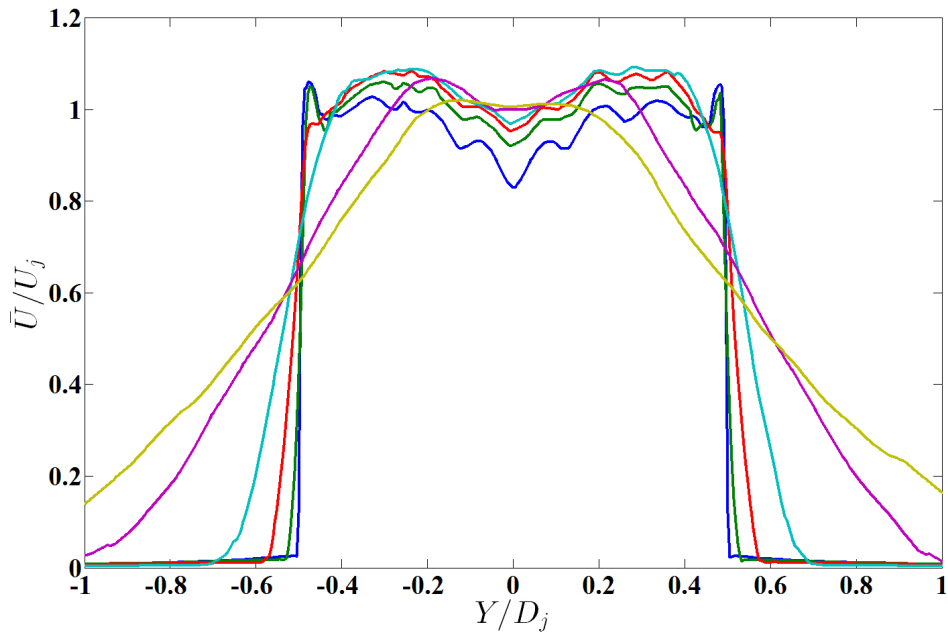
(d)

Figure 4.10: Downstream plume survey of mean streamwise velocity across transverse cross-section of the jet at different downstream locations. (a): confluent mixer; (b): 20UH; (c): 20MH; (d): 20DH. Dark blue line: at nozzle exit plane; green line: $0.2D_j$ downstream of the nozzle exit; red line: $0.5D_j$ downstream of the nozzle exit; light blue line: $1D_j$ downstream of the nozzle exit; purple line: $3D_j$ downstream of the nozzle exit; brown line: $5D_j$ downstream of the nozzle exit.
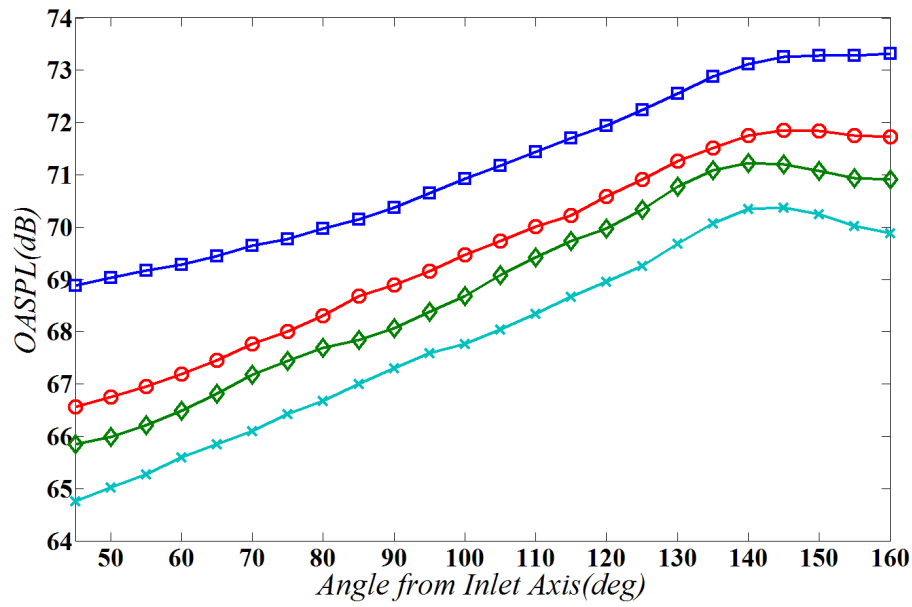
Figure 4.11: OASPL directivity. ⊟: confluent mixer; ◇: 20UH; ⊖: 20MH; ✳: 20DH.
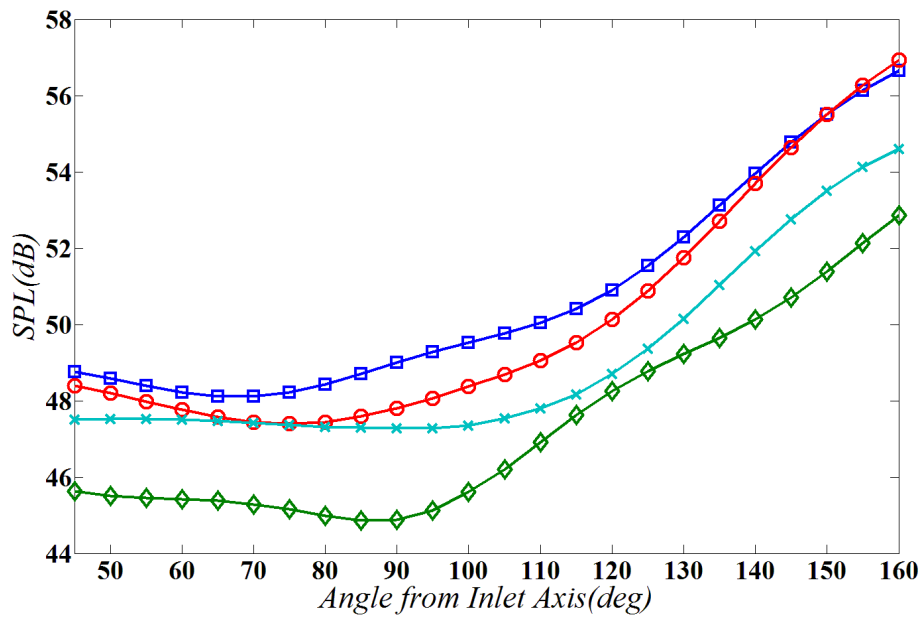
Figure 4.12: Band-passed 120hz SPL directivity. ⊟: confluent mixer; ◇: 20UH; ⊖: 20MH; ✳: 20DH.
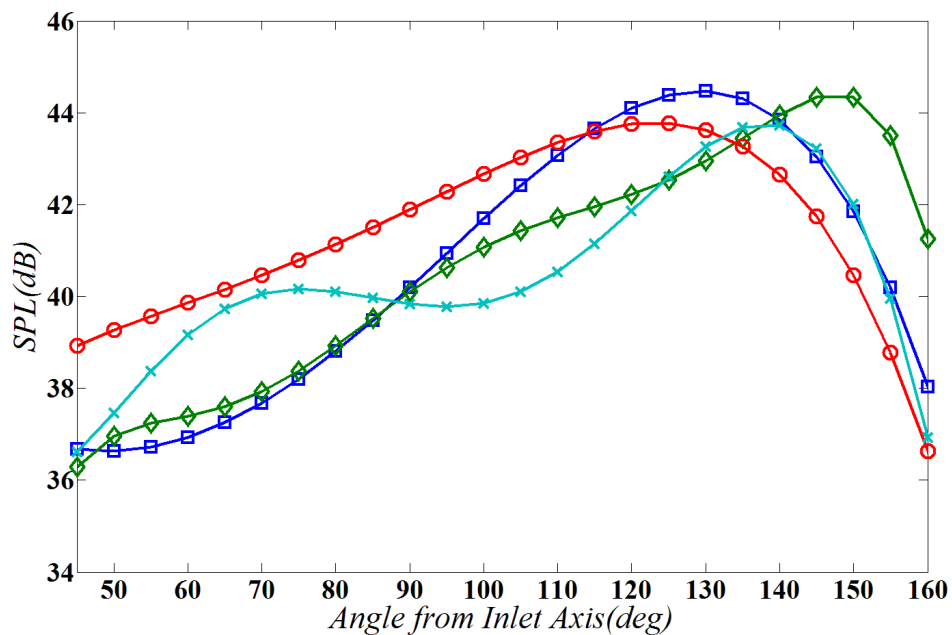
Figure 4.13: Band-passed 1200hz SPL directivity. ⊟: confluent mixer; ◇: 20UH;
⊖: 20MH; ✳: 20DH.
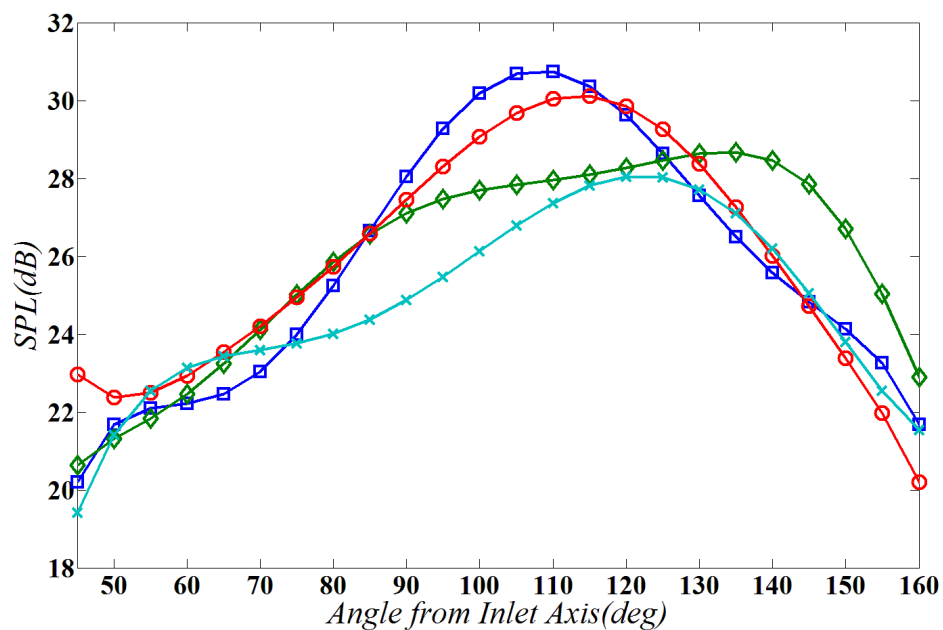
Figure 4.14: Band-passed 4500hz SPL directivity. ⊟: confluent mixer; ◇: 20UH;
⊖: 20MH; ✳: 20DH.

Chapter 5 Conclusions and Future Work

5.1 Conclusions

Four lobed mixers and one baseline confluent mixer were investigated in a computational study of the aerodynamic and aeroacoustic effects of actual turbo-fan jet engine mixer-nozzle geometries. The Lattice Boltzmann Method (LBM) was used because of its advantages to handle complex geometries in the computational domain. The grid distribution and measurement settings were refined to capture the sensitivity of the near-field flow patterns and far-field sound levels to the mixer geometric difference, as was shown by the aerodynamic and acoustic results. The data showed that the boundary conditions and artificial forcing functions imposed at the inlet produced realistic turbulent kinetic energy levels downstream of the nozzle exit.

5.1.1   Effects of Lobe Number and Penetration Depth

The first group of mixers was studied to understand the effects of different lobe number and penetration depth. As expected, lobed mixers enhanced mixing inside the nozzle relative to the baseline confluent mixer. Results showed that the three mixers (i.e., confluent, 12CL and 20UH) reached a fully turbulent state within one jet diameter downstream of the nozzle. Due to a smaller lobe number, the scale of the vortices shed from the 12CL mixer was found to be larger than from the 20UH mixer. This may have led to the greater levels of noise in the low-to-mid frequency domain for the 12CL mixer. The high penetration of 20UH guided part of the vortex into the shear layer, and, as a consequence, the turbulent kinetic energy level was raised in the downstream shear layer. The 20UH mixer features a turbulent kinetic energy concentration at the nozzle exit. However, this did not seem to result in a considerable

increase in mid-to-high frequency noise and Overall Sound Pressure Level (OASPL). The velocity exit profile of 20UH was found to be more uniform than that of 12CL. The high velocity gradient of 20UH was also smaller and decayed faster than that of 12CL. These two differences were attributed to the increased interface area of the 20UH mixer. There were some differences in mean streamwise centerline velocity decay pattern, but it did not seem to affect the far-field sound levels.

The two lobed mixers showed their noise reduction benefit over the confluent mixer. The 20UH mixer demonstrated its capacity for greater noise reduction compared with 12CL. The smaller scale vortex of 20UH did lead to an improvement over 12CL in the low-frequency domain. At high frequencies, the noise reduction advantage of 20UH was not as significant. The 12CL mixer had higher low-to-mid frequency noise and a lower high frequency SPL level in the far downstream than 20UH. The high penetration depth and higher lobe number of 20UH had the benefit of decreasing the mid-frequency noise while maintaining considerable reduction in low-frequency noise. In addition, the results implied an upstream shift in the SPL level peaks with the frequency increase for all the mixers.

5.1.2   Effects of Scalloping

The 20UH, 20MH and 20DH mixers along with confluent mixer were studied to uncover the impact of scalloping. The medium scalloping brought the 20MH mixer the earliest transition to a fully turbulent state and the fastest turbulent kinetic energy increasing rate among the three lobed mixers. This directly led to the differentiation of 20MH from the other two lobed mixers in far-field sound field. The results suggested that there might exist a threshold value that determines whether or not scalloping could yield noise reduction benefits. Because of the different sidewall scalloping, the characteristic length and strength of the shed vortex in the three mixers were different. Some vorticity dissipation existed downstream of the scalloped mixers exit. This impact was reflected in the differences in turbulent kinetic energy levels in the shear layer, and hence on the far-field SPL directivity level. Scalloping tended to guide the

shed vortices towards the central jet flow region thus interacting with the flow further downstream. All three scalloped mixers had a fairly uniform velocity profile at the exit, and the high velocity gradient was found close to the nozzle exit wall. The 20DH mixer had a high peak value of the centerline mean streamwise velocity variation; however, this did not produce an increase in the far-field sound pressure level.

Among the three mixers, 20DH had the lowest OASPL level, and 20MH had the highest. The introduction of scalloping did not yield the same low-frequency noise reduction advantage as for the 20UH unscalloped mixer, but it yielded reduction benefits in the low-frequency domain. The 20DH results showed that deep scalloping tended to trade some of the advantage of suppressing low-frequency noise for decreasing the noise in the high-frequency domain. The SPL directivity showed that there was a peak shift associated with the scalloping depth variation. The SPL levels also confirmed an upstream peak shift related to the frequency domain for the three cases.

5.2 Plans for Future Work

5.2.1 High Mach Number Simulations

Due to the current limit of simulated Mach of LBM, the exit flow velocity was relatively low compared to practical commercial jet engine operating conditions. A high Mach version of the LBM-based commercial code is expected to be released for validation and practice in the near future. By then, the same experimental conditions of lobed mixers will be utilized in the simulation to achieve the exit jet Mach number close to 0.9.

5.2.2 Heated Jet Simulation

The current LBM model only allows heated jet simulation with a limit of Mach 0.2. This is apparently not of much practical use for jet noise prediction. With the release of the high Mach LBM code, high Mach heated jet simulation will be carried

out with a fully coupled LBM-heat transfer scheme.

5.2.3   Two-Step Simulation

Jet flow simulation can be divided into internal and external flow simulation. Depending on whether the simulation domain is inside or outside of the nozzle, the flow is called internal or external flow. The idea of two-step simulation is to first run the internal simulation and record all the interested data (i.e., velocity, pressure and temperature). The recorded data is then fed to the second-step external simulation. The advantage of this approach is that considerable computational cost is saved because the expensive second-step external simulation does not need to be started until the internal flow reaches the fully convergent state. The difficulties are to impose the proper outlet boundary condition in the first step and reduce the size of the recorded data. Preliminary study on the confluent mixer has already been conducted, and it proved technically feasible at the current stage.

5.2.4   Parametric Studies of the Lobed Mixer Geometry

The key parameters of a lobed mixer include lobe number, penetration depth, scalloping shape, lobe width, lobe height and sidewall cut-off angle. In this study, the investigation of the scalloping effect can be considered a first step. Because a systematic experimental study on these parameters is practically almost impossible, the LBM-based simulation tailored particularly for the complex flow appears to be an excellent option.

References

[1] Hygge, S., Evans, G.W., and Bullinger, M., "A Prospective Study of Some Effects of Aircraft Noise on Cognitive Performance in Schoolchildren," *Psychological Science*, Vol. 13, No. 5, September 2002, pp. 469–474.

[2] "AeroAcoustics Research Consortium," (http://www.oai.org/aeroacoustic /challenge.html).

[3] McCormick, D. C., and Bennett, J. C., Jr., "Vortical and Turbulent Structure of a Lobed Mixer Free Shear Layer," *AIAA Journal*, Vol. 32, No. 9, 1994, pp. 1852-1859.

[4] Belovich, V. M., Samimy, M., and Reeder, M. F., "Dual Stream Axisymmetric Mixing in the Presence of Axial Vorticity," AIAA-94-3084, 30th AIAA/ASME/SAE/ASEE Joint Propulsion Conference, Indianapolis, Indiana, June 1994.

[5] Manning, T. A., "Experimental Studies of Mixing Flows with Streamwise Vorticity," M.S. Thesis, Massachusetts Inst. of Technology, Cambridge, MA, September 1991.

[6] Paterson, R.W., "Turbofan Forced Mixer-Nozzle Internal Flow Field," NASA Contractor Report 3492.

[7] Paterson, R.W., "Turbofan Mixer Nozzle Flow Field-A Benchmark Experimental Study," *ASME Journal of Engineering for Gas Turbines and Power*, Vol. 106, pp.692-698.

[8] Werle, M. J., Paterson, R. W., and Presz, W. M., Jr.,"Flow Structure in a Periodic Axial Vortex Array," AIAA-87-610, AIAA 25th Aerospace Sciences Meeting, Reno, Nevada, January 1987.

[9] Eckerle, W.A, Sheibani, H. and J. Awad, "Experimental Measurement of the Vortex Development Downstream of a Lobed Forced Mixer," *ASME* Paper 90-GT-27.

[10] Barber, T. Paterson, R. W., and Skebe, S. A., "Turbofan Forced Mixer Lobe Flow Modeling, I-Experimental and Analytical Assessment," NAS3-23039, NASA CR 4147, Part I, 1988.

[11] McCormick, D.C., "Vortical and TurbulentStructure of Planar and Lobed Mixer Free-Shear Layers," Ph.D. Dissertation, University of Connecticut.

[12] McCormick, D. C., and Bennett, J. C., Jr., "Vortical and Turbulent Structure of a Lobed Mixer Free Shear Layer," *AIAA Journal*, Vol. 32, No. 9, 1994, pp. 1852-1859.

[13] Frost, T. H., "Practical Bypass Mixing Systems for Fan Jet Aero Engines," *The Aeronautical Quarterly*, pp. 141-160, May 1966.

[14] Hartmann, A., "Studies of Mixing in Ducted Fan Jet Engines," NASA Report TT F-12, 562, November 1969.

[15] Packman, A. B., Kozlowskim, H., and Gutierrez, O., "Jet Noise Characteristics of Unsuppressed Duct Burnig Turbofan Exhaust System," AIAA-76-149, AIAA 14th Aerospace Sciences Meeting, Washington, D.C., January 1976.

[16] Shumpert, P. K., "An Experiment Model Investigation of Turbofan Engine Internal Exhaust Gas Mixer Configurations." AIAA-80-0228, AIAA 18th Aerospace Sciences Meeting, Pasadena, California, January 1980.

[17] Kuchar, A., "Scale Model Performance Test Investigation of Exhaust System Mixer for an Energy Efficient Propulsion (E3) System." AIAA-80-0229, AIAA 18th Aerospace Sciences Meeting, Pasadena, California, January 1980.

[18] Larkin, M. J. and Blatt, J. R., "Energy Efficient Engine Exhaust Mixer Model Technology Report Addendum, Phase III Test Program." NASA CR 174799, April 1984.

[19] Crouch, R. W., Coughlin, C. L., and Paynter, G.C., "Nozzle Exit Flow Profile shaping for Jet Noise Reduction," AIAA-76-511, 3rd AIAA Aeroacoustics Conference, Palo Alto, California, July 1976.

[20] Shumpert, P. K., "An Experiment Model Investigation of Turbofan Engine Internal Exhaust Gas Mixer Configurations." AIAA-80-0228, AIAA 18th Aerospace Sciences Meeting, Pasadena, California, January 1980.

[21] Kozlowski, H., and Kraft, G., "Experimental Evaluation of Exhaust Mixers for an Energy Efficient Engine Propulsion System," AIAA-80-1088, AIAA/SAE/ASME 16th Joint Propulsion Conference, Hartford, Connecticut, January 1980.

[22] Barber, T., "Turbofan Forced Mixer Lobe Flow Modeling, II-Three-Dimensional Inviscid Mixer Analysis (FLOMIX)," NAS3-23039, NASA CR 4147, Part II, 1988.

[23] Barber, T., Moore, G. C. and Blatt, J. R., "Turbofan Forced Mixer Lobe Flow Modeling, III- Application to Augment Engines," NAS3-23039, NASA CR 4147, Part III, 1988.

[24] Booher, M. E., Kwon, O., Barta, A. B., Vittal, B. R., and Krishnan, M. R., "Development of an Advanced Exhaust Mixer for a High Bypass Ratio Turbofan Engine," AIAA-93-2435, AIAA/SAE/ASME/ASEE 29th Joint Propulsion Conference and Exhibit, Monterey, California, June 1993.

[25] Meade, J. P., "Acoustic Evaluation of a Forced Mixer on a High Bypass Ratio Engine," AIAA-94-2954, AIAA/SAE/ASME 30th Joint Propulsion Conference, Indianapolis, Indiana, June 1994.

[26] Presz, W. M., Blinn, R. F., and Morin, B., "Short Efficient Ejector System," AIAA-87-1837, AIAA/SAE/ASME/ASEE 23rd Joint Propulsion Conference, San Diego, California, June 1987.

[27] Presz, W. M., Gousy, R., and Morin, B., "Forced Mixer Lobes in Ejector Design," *Journal of Propulsion and Power*, Vol. 4, No. 4, 1988, pp. 350-360.

[28] Presz, W. M., Reynolds, G., and McCormick, D., "Thrust Augmentation Using Mixer-Ejector-Diffuser System," AIAA-94-0020, 32nd Aerospace Sciences Meeting & Exhibit, Reno, Nevada, January 1994.

[29] Povinelli, L. A. and Anderson, B. H., "Investigation of Mixing in turbofan Exhaust Duct, Part II: Computer Code Application of Verification," *AIAA* Journal, Vol. 22, No. 4, 1984, pp. 518-525.

[30] Barber, T. J., Muller, G. L., Ramsey, S. M., and Murman, E. M., "Three Dimensional Inviscid Flow in Mixers, Part I: Mixer Analysis Using a Cartesian Grid," *AIAA Journal of Propulsion and Power*, Vol. 2, No. 3, 1986, pp. 275-281.

[31] Barber, T. J., Muller, G. L., Ramsey, S. M., and Murman, E. M., "Three Dimensional Inviscid Flow in Mixers, Part II: Analysis of Turbofan Forced Mixers," *AIAA Journal of Propulsion and Power*, Vol. 2, No. 4, 1986, pp. 339-344.

[32] Koutmos, P., and McGuirk, J. J., "Turbofan Forced Mixer/Nozzle Temperature and Flow Field Modeling," *International Journal of Heat and Mass Transfer*, Vol. 32, No. 6, 1989, pp. 1141-1152.

[33] Malecki, R. and Lord, W., "Navier-Stokes Analysis of a Lobed Mixer and Nozzle," AIAA-90-0453, 28th Aerospace Sciences Meeting, Reno, Nevada, January 1990.

[34] Abolfad, M., and Sehra, A., "Applications of Three Dimensional Viscous Analysis to Turbofan Mixers," 29th Aerospace Science Meeting, Reno, NV, January 1991.

[35] Barber, T. J., Chiappetta, L. M., and Zysman, S. H., "An Assessment of Jet Noise Analysis Codes for Multistream Axiaymmetric and Forced Mixer Nozzles," AIAA-96-0750, 34th Aerospace Sciences Meeting, Reno, Nevada, January 1996.

[36] Salman, H., "Numerical Simulation of Streamwise Vorticity Enhanced Mixing." PhD. Dissertation, Loughborough University, January 2001.

[37] Salman, H., McGuirk, J. J., and Page, G. J., "A Numerical Study of Vortex Interactions in Lobed Mixer Flow Fields," AIAA-99-3409, 30th AIAA Fluid Dynamics Conference, Norfolk,VA, 1999.

[38] Garrison, L. A., "Computational Fluid Bynamics Analysis and Noise Modeling of Jets with Internal Forced Mixers," PhD. Dissertation, Purdue University, West Lafayette, IN, May 2006.

[39] Freund, J. B., Lele, S. K., and Moin, P., "Direct Numerical Simulation of a Mach 1.92 Turbulent Jet and Its Sound Field," *AIAA* Journal, Vol. 38, No. 11, November 2000, pp. 2023–2031.

[40] Freund, J. B., "Noise Sources in a Low-Reynolds-number Turbulent Jet at Mach 0.9," *Journal of Fluid Mechanics*, Vol. 438, 2001, pp. 277–305.

[41] Mankbadi, R. R., Hayder, M. E., and Povinelli, L. A., "Structure of Supersonic Jet Flow and Its Radiated Sound," *AIAA* Journal, Vol. 32, No. 5, May 1994, pp. 897–906.

[42] Lighthill, M. J., "On the Sound Generated Aerodynamically: I, General Theory," *Proc. Royal Soc. London A*, Vol. 211, 1952, pp. 564–587.

[43] Lyrintzis, A. S. and Mankbadi, R. R., "Prediction of the Far-field Jet Noise Using Kirchhoff's Formulation," *AIAA* Journal, Vol. 36, No. 12, 1996, pp. 1–4.

[44] Constantinescu, G. S. and Lele, S. K., "Large Eddy Simulation of a Near Sonic Turbulent Jet and Its Radiated Noise," AIAA-2001-0376, 39th AIAA Aerospace Sciences Meeting & Exhibit, Reno, Nevada, January 2001.

[45] Uzun, A., Blaisdell, G. A., and Lyrintzis, A. S., "Coupling of Integral Acoustic Methods with LES for Jet Noise Prediction," *International Journal of Aeroacoustics*, Vol. 3, No. 4, 2005, pp. 297–346.

[46] Bogey, C. and Bailly, C., "LES of High Reynolds, High Subsonic Jet: Effects of the Inflow Conditions on Flow and Noise," AIAA-2003-3170, 9th AIAA/CEAS Aeroacoustics Conference and Exhibit, Hilton Head, South California, May 2003.

[47] A. Uzun., "3-D Large Eddy Simulation for Jet Aeroacoustics," PhD thesis, School of Aeronautics and Astronautics, Purdue University, West Lafayette, IN, December 2003.

[48] Andersson, N., Eriksson, L.-E., and Davidson, L., "Large-Eddy Simulation of Subsonic Turbulent Jets and Their Radiated Sound," *AIAA Journal*, Vol. 43, No. 9, 2005, pp. 1899–1912.

[49] Paliath, U. and Morris, P. J., "Prediction of Noise from Jets with Different Nozzle Geometries," AIAA-2004-3026, 10th AIAA/CEAS Aeroacoustics Conference, May 2004.

[50] Shur, M. L., Spalart, P. R., and Strelets, M. K., "Noise Prediction for Increasingly Complex Jets, Part I: Methods and Tests," *International Journal of Aeroacoustics*, Vol. 4, No. 3 and 4, 2005, pp. 213–246.

[51] Uzun, A. and Hussaini, M. Y., "High Frequency Noise Generation in the Near-Nozzle Region of a Jet," AIAA-2006-2499, 12th AIAA/CEAS Aeroacoustics Conference, Cambridge, Massachusetts, May 2006.

[52] Chen, S. and Doolen, G., "Lattice Boltzmann Method for Fluid Flows," *Ann. Rev. Fluid Mech.*, Vol. 30, 1998, pp. 329–364.

[53] Chapman, P. and Cowling, T., The Mathematical Theory of Non-uniform Gases, Cambridge University Press, 1990.

[54] Chen, H., Teixeira, C., and Molvig, K., "Digital Physics Approach to Computational Fluid Dynamics: Some Basic Theoretical Features," *Int. J. Mod. Phys. C*, Vol. 8, 1997, pp. 675–684.

[55] Chen, H., Chen, S., and Matthaeus, W. H., "Recovery of the Navier-Stokes Equations using a lattice-gas Boltzmann Method," *Phys. Rev. A*, Vol. 45, No. 8, 1992, pp. R5339–R5342.

[56] Lew, P., Najafiyazdi, A. and Mongeau, L., "Unsteady Numerical Simulation of a Round Jet with Impinging Microjets for Noise Suppression," AIAA-2010-0018, 48th Aerospace Sciences Meeting, Orlando, Florida, January 2010.

[57] Habibi, K., Najafiyazdi, A., Lew, P. and Mongeau, L., "Simulation of Sound Radiated from Turbulent Heated Jets using the Lattice Boltzmann Method,"

AIAA-2011-2885, 17th AIAA/CEAS Aeroascoustics Conference, Portland, Oregon, June 2011.

[58] G. M. Lilley. The generation and radiation of supersonic jet noise. Part IV: Theory of turbulence generated jet noise, noise radiation from upstream sources and combustion noise. AFAPL-TR-72-53 Volume IV, 1972.

[59] Najafi-Yazdi, A., Brès, G. A., & Mongeau, L. (2011). "An acoustic analogy formulation for moving sources in uniformly moving media". *Proceedings of the Royal Society A: Mathematical, Physical and Engineering Science*, 467(2125), 144-165.

[60] Lyrintzis, A. S. and Uzun, A., "Integral Techniques for Jet Aeroacoustics Calculations," AIAA-2001-2253, 7th AIAA/CEAS Aeroacoustics Conference, Maastricht, Netherlands, May 2001.

[61] Lyrintzis, A. S., "Surface Integral Methods in Computational Aeroacoustics - From the (CFD) Near-field to the (Acoustic) Far-Field," *International Journal of Aeroacoustics*, Vol. 2, No. 2, 2003.

[62] Bhatnagar, P., Gross, E., and Krook, M., "A Model for Collision Processes in Gases I. Small Amplitude Processes in Charged and Neutral One-Component System," *Physics Review*, Vol. 94, 1954, pp. 511–525.

[63] Chen, H., "Volumetric Formulation of the Lattice Boltzmann Method for Fluid Dynamics: Basic Concept," *Physics Review E*, Vol. 58, 1998, pp. 3955–3963.

[64] Crouse, B., Senthooran, S., Balasubramanian, G., Freed, D., Lew, P., and Mongeau, L., "Fundamental Aeroacoustics Capabilities of the Lattice-Boltzmann Method," *AIAA* Paper No. 2006-2571, 2006.

[65] Chen, H., Chen, S., and Matthaeus, W. H., "Realization of Fluid Boundary Conditions via Discrete Boltzmann Dynamics," *Intl. J. Mod. Phys. C*, Vol. 9, No. 8, 1998, pp. 1281–1292.

[66] Bogey, C. and Bailly, C., "Decrease of the Effective Reynolds Number with Eddy-Viscosity Subgrid-Scale Modeling," *AIAA* Journal, Vol. 43, 2005, pp. 437–439.

[67] Sun, C. and Hsu, A., "Multi-level lattice Boltzmann model on square lattice for compressible flows," *Computers and Fluids*, Vol. 33, 2004, pp. 1363–1385.

[68] Shan, X., Yuan, X., and Chen, H., "Kinetic Theory Representation of Hydrodynamics: A way beyond the Navier-Stokes Equation," *Journal of Fluid Mechanics*, Vol. 550, 2006, pp. 413–441.

[69] Chen, H., Orszag, S. A., and Staroselsky, I., "Macroscopic Desciption of Arbitrary Knudsen Number Flow using Boltzmann-BGK Kinetic Theory," *Journal of Fluid Mechanics*, Vol. 574, 2007, pp. 495–505.

[70] Li, X. M., Leung, R. C. L., and So, R. M. C., "One-Step Aeroacoustics Simulation Using Lattice Boltzmann Method," *AIAA Journal*, Vol. 44, No. 1, January 2006, pp. 78–89.

[71] Li, Y., Shock, R., Zhang, R., and Chen, H., "Numerical Study of flow past an impulsively started cylinder by the lattice-Boltzmann method," *Journal of Fluid Mechanics*, Vol. 519, 2004, pp. 273–300.

[72] Mengle, V. G., and Dalton, W. N., "Lobed Mixer Design for Noise Suppression: Vol. 1," NASA CR-2002-210823/Vol1, July 2002.

[73] Mengle, V. G., Barker, V. D., and Dalton, W. N., "Lobed Mixer Design for Noise Suppression: Vol. 2," NASA CR-2002-210823/Vol2, July 2002.

[74] Packman, A.B and Eiler, D.C., "Internal mixer Investigation for JT8D Engine Jet noise Reduction, Vol.I-Results."U.S. Dept. of Transportation, Federal Aviation Administration Report No. FAA RD-77-132.1.

[75] Lew, P., Lyrintzis, A., Crouse, B., Balasubramanian, G., Freed, D., Mongeau, L., "Noise Prediction of a Subsonic Turbulent Round Jet using the Lattice-Boltzmann Method," AIAA-2007-3636, 13th AIAA/CEAS Aeroacoustics Conference, Roma, Italy, May 2007.

[76] Bogey, C., Marsden, O., & Bailly, C., "Large-eddy simulation of the flow and acoustic fields of a Reynolds number 10^5 subsonic jet with tripped exit boundary layers," *Physics of Fluids*, Vol. 23, 2011

[77] Greitzer, E., Paterson, R. W. and Tan, S. C., 1985, "An Approximation Substitution Principle for Viscous Heat Conducting Flows," *Proceedings of the Royal Society of London*, Vol. 401, No. 5, pp. 162-192.

[78] Freund, J. B., "Direct Numerical Simulation of the Noise from a Mach 0.9 Jet," *FEDSM* Paper No. 99-7251, July 1999.

[79] Jeong, J., Hussain, F., "On the Identification of a Vortex," *Journal of Fluid Mechanics*, Vol. 285., pp.69-94

[80] Abramovich,G.N., The Theory of Turbulent Jets, the MIT Press, Cambridge, Massachusetts, 1936.

[81] Tam, C.K.W., Viswanathan, K., Ahuja, K.K., Panda, J., "The Sources of Jet Noise: Experimental Evidence, " *Journal of Fluid Mechanics*, Vol. 615, pp.253-292.

[82] Fisher, M.J., Preston, G.A. and Bryce, W.D, "A Modeling of the Noise from Simple Co-Axial Jets," AIAA-93-4413, 2nd AIAA/CEAS Aeroacoustics Conference, State College, Pennsylvania, October 1993.